AD NUMBER

AD810471

NEW LIMITATION CHANGE

TO

Approved for public release, distribution unlimited

FROM

Distribution authorized to U.S. Gov't. agencies and their contractors; Administrative/Operational Use; MAR 1967. Other requests shall be referred to Air Force Weapons Lab., Kirtland AFB, NM.

AUTHORITY

AFWL ltr, 30 Nov 1971

AFWL-TR
66-130

CRITICAL LOAD CURVES FOR REBOUND CRACKING

G. S. Samuelsen
W. Stuiver
G. R. Abrahamson

Stanford Research Institute
Menlo Park, California
Contract AF 29(601)-6828

TECHNICAL REPORT NO. AFWL-TR-66-130
March 1967

AIR FORCE WEAPONS LABORATORY
Research and Technology Division
Air Force Systems Command
Kirtland Air Force Base
New Mexico

Research and Technology Division
AIR FORCE WEAPONS LABORATORY
Air Force Systems Command
Kirtland Air Force Base
New Mexico

AFWL-TR-66-130

CRITICAL LOAD CURVES FOR REBOUND CRACKING

G. S. Samuelsen

W. Stuiver

G. R. Abrahamson

Stanford Research Institute
Menlo Park, California
Contract AF29(601)-6828

TECHNICAL REPORT NO. AFWL-TR-66-130

FOREWORD

This report was prepared by the Poulter Laboratories, Stanford Research Institute, Menlo Park, California under Contract AF29(601)-6828. The research was performed under Program Element 6.16.46.01D, Project 5710, Subtask 15.014, and was funded by the Defense Atomic Support Agency (DASA).

Inclusive dates of research were June 1965 through September 1966. The report was submitted 13 February 1967 by the AFWL Project Officer, Lt Walter D. Dittmer (WLRP). Contractor's report number is FGU-5569.

Technical direction was provided by Lt R. C. Brightman and Lt W. Dittmer in coordination with Lt L. T. Montulli, all of the Physics Branch of the Air Force Weapons Laboratory (WLRP).

The authors are indebted to Betty Bain, who provided invaluable assistance with the numerical calculations presented in Section 2, and to Leonard Dary, who was responsible for the experimental work.

This report has been reviewed and is approved.

Walter D Dittmer

WALTER D. DITTMER
Lt, USAF
Project Officer

Harvey A Riggs Maj for

EDGAR M. MONYON
Colonel, USAF
Chief, Physics Branch

CLAUDE K. STAMBAUGH
Colonel, USAF
Chief, Research Division

ABSTRACT

It is shown that, under an external load, a cylindrical plastic shell mounted on a steel mandrel can rebound at a velocity sufficient to cause cracking of the shield due to hoop tension. Using numerical calculations, critical load curves are found for the combinations of peak pressure and impulse which divide the loads that produce cracking from those that do not. These curves are found to be consistent with semigraphical solutions based on the method of characteristics. The latter method is also used to obtain critical load curves for spall.

Experiments that verify the theory of rebound cracking are reported.

This page intentionally left blank.

CONTENTS

ILLUSTRATIONS

ILLUSTRATIONS (Continued)

ILLUSTRATIONS (Concluded)

TABLES

This page intentionally left biank.

SECTION 1

INTRODUCTION

As illustrated in Fig. 1.1, a cylindrical plastic shield supported by a metal base structure may fail by rebound cracking under a suddenly applied surface load. In this report the shield is taken to be thin compared to its radius and compared to the thickness of the supporting base structure; the load is taken as uniform over the surface. Under these conditions, the rebound velocity of the shield can be found using one-dimensional wave theory. To calculate the hoop stress developed, the subsequent motion of the shield is taken to be a linear oscillation. Cracking occurs if the hoop stress developed during the outward motion exceeds the strength of the shield.

For loads with a step rise and gradual decay, the combinations of peak pressure and total impulse which result in cracking would be expected to appear as shown in Fig. 1.2. For loads of duration less than twice the transit time through the shield, the outward displacement depends only on the impulse. As load duration increases, the peak pressure must be increased to maintain the rebound velocity. Moreover, for the loads acting after separation, a higher rebound velocity is necessary to reach the critical displacement. Hence, as load duration increases, peak pressure (and thus impulse) required to cause cracking increase as indicated in Fig. 1.2.

In the present investigation methods for determining cracking boundaries are developed and the theory of rebound cracking is checked experimentally. Cracking boundaries are determined for a typical plastic supported by a base of thick aluminum, a base of thin aluminum, and a base of thin aluminum over a rigid foam for pulses with a step rise and exponential decay. More limited calculations are made for pulses with a step rise and linear decay. Rebound velocities are obtained from numerical calculations based on the Q-method and the maximum displacement is found, regarding the plastic cylinder as a linear oscillator. The

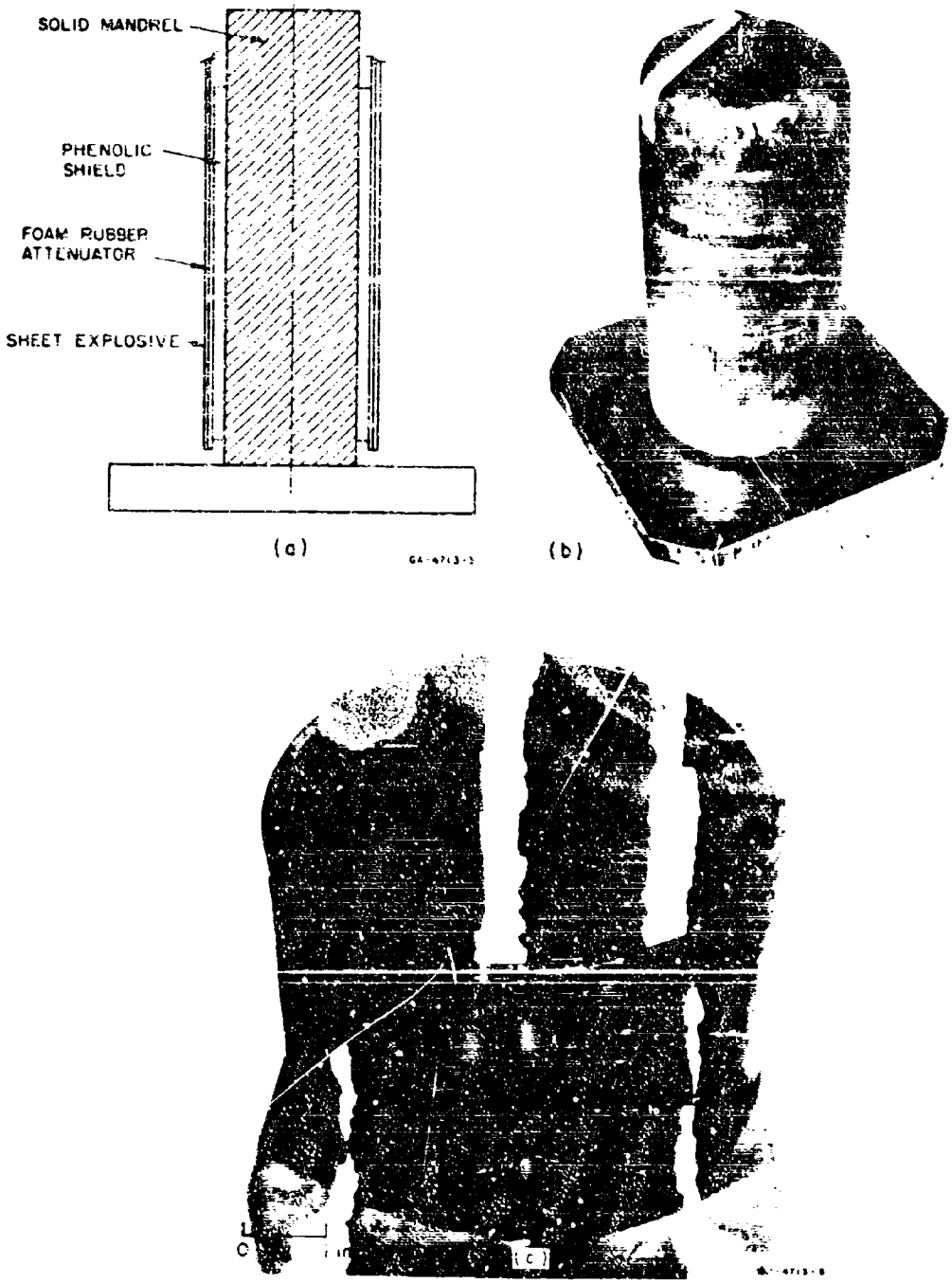

FIG. 1.1 EXPERIMENT DEMONSTRATING REBOUND CRACKING. The explosive drives the Phenolic shield against the steel. Since the steel has a higher shock impedance, the shield rebounds. If the rebound velocity is sufficient, cracking occurs as shown.

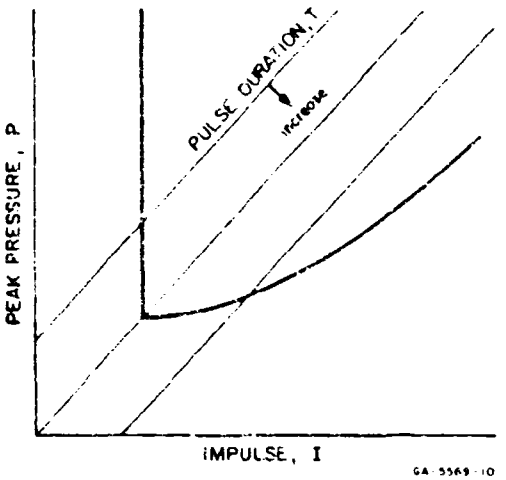

FIG. 1.2 SHAPE OF CRACKING BOUNDARY

cracking boundary in the pressure-impulse plane is the line separating the region of cracking from the region of no cracking. The cracking boundary is also determined using a graphical method based on linear wave theory. The boundaries obtained by the two methods are found to be consistent.

The graphical technique is also used to obtain the spall boundary in the pressure-impulse plane. The boundary obtained is consistent with the results of the numerical calculations.

A limited series of experiments were undertaken to check the validity of the theory of rebound cracking. The experimental results agree with the predictions within experimental error.

In Section 2 the numerical calculations are described and the cracking boundaries obtained are plotted. In Section 3 an introduction to the graphical analysis is given and the results are compared with those of the numerical calculations. A detailed description of the graphical method is given in Section 4. The experiments undertaken to verify the theory are described in Section 5.

This page intentionally left blank.

SECTION 2

NUMERICAL SOLUTIONS

2.1 Introduction

The response of a shield on a thick base has been extensively analyzed for uniform [1] and exponential pulses (Section 4) for linear-elastic materials, using the method of characteristics. However, under high pressures some materials exhibit strong nonlinear properties and respond plastically. Such conditions introduce complex interactions between variables and necessitate a different theoretical approach.

In the present study a computer code was modified to study the effects of pulses with a step rise and exponential or linear decay, applied uniformly to the exterior of a cylindrical model for which the modes of failure are cracking and spalling of the shield. Three models were investigated: (1) two-layered composite with a thick base, (2) two-layered composite with a thin base, and (3) three-layered composite with a thin base backed by foam.

The primary purpose of this work was to determine critical load boundaries for rebound cracking of the shield, taking account of nonlinear and plastic effects on stress-wave propagation. The calculations are divided into two parts: (1) early-time stress-wave propagation in the composite prior to separation, and (2) late-time structural displacement of the shield after separation. The stress-wave calculations yield the rebound velocity of the shield, which is the initial condition for the structural displacement calculations.

The shield is taken to be thin relative to the radius, permitting a one-dimensional model to be used for the stress-wave calculations. The stress-wave calculations are made using the Q-method of von Neumann and Richtmyer [2], which has proven very useful for nonuniform wave

flow, particularly where nonlinear material properties are involved. The method is based upon finite difference equations and an artificial viscosity function which removes discontinuities in the flow field; wave interactions are handled automatically and it is unnecessary to locate the wave fronts as with the method of characteristics. The code used here is based on a code developed by White and Griffis [3], Wood [4], and Morland [5], and generalized by Erkman [6].

The late-time structural model used is a ring in uniform radial motion, regarded as a linear oscillator. The maximum displacement is found for the rebound (initial) velocity and the incident load acting after separation. Cracking is taken to occur if the displacement exceeds a critical value.

The three models investigated are described in Table 2.1. For all models, the shield and base were epoxy and aluminum and the shield thickness was 2.54 cm. Model 1, the two layered (thick base) composite, was the one most extensively analyzed. For this model, the influence of linearity and plasticity were studied for exponential and triangular pulse profiles.

Models 2 and 3 were used to study the effect of rigid foam as a third layer. The thickness of the thin base was 0.635 cm. For Model 3, a thick layer of 7 lb/ft^3 foam was added to Model 2.

Table 2.1

MATERIAL PROPERTIES

Material	Density (g/cm^3)	Sound Speed (cm/μsec)	Acoustic Impedance (barsec/cm)	Yield Stress (kbar)	Poisson's Ratio	Model	Thickness (cm)	Mean Radius-r_m (cm)
Epoxy C-7	1.18	0.265	0.313	3.0	0.4	1,2,3	2.54	38.1
Aluminum (6061-T6)	2.79	0.640	1.781	5.0	0.3	1 2,3	"infinite" 0.635	...
Rigid foam	0.11 (7 lb/ft^3)	0.253	0.028	0.011	...	3	"infinite"	...

In Section 2.2 the theoretical bases for the stress-wave and structural displacement calculations are given and the failure criteria are described. In Section 2.3 the critical cracking boundaries determined from the numerical calculations are presented.

2.2 Approach

2.2.1 Basic Equations for Stress-Wave Calculations

The shield and base materials are represented by the elastoplastic model of Fig. 2.1. With this model, the material behaves elastically along ba, in which a is the yield point in compression. Segment ae is the locus of plastic loading states, ef the locus of elastic unloading states, and fb the locus of plastic unloading states. The mean pressure and maximum resolved shear stress are defined by

$$d\bar{p} = \frac{1}{3} d(p_x + p_y + p_z) \tag{2.1}$$

$$d\tau = \frac{dp_x - dp_y}{2} \tag{2.2}$$

and the compressive stress in the direction of propagation is given by

$$dp_x = d\bar{p} + \frac{4}{3} d\tau \tag{2.3}$$

The relationship between the mean pressure and density (Hugoniot) was assumed to be of the form

$$\bar{p} = A\mu + B\mu^2 + C\mu^3 \tag{2.4}$$

where $\mu = \rho/\rho_o - 1$ and A, B, and C are constants depending on the material (see Fig. 2.1).

Equation (2.3) is the basic relation used in the numerical calculations and was specialized for the various segments of Fig. 2.1.

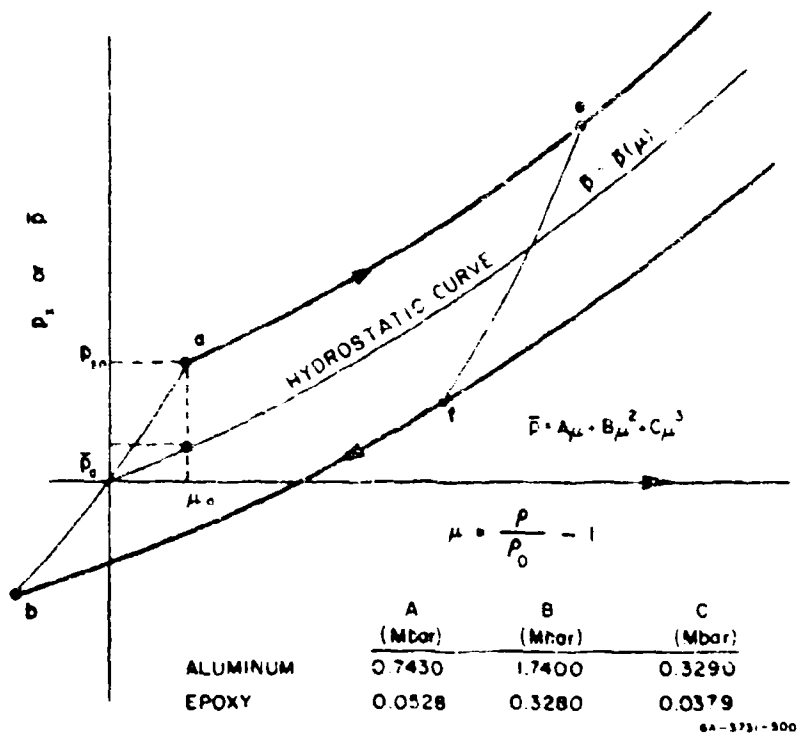

	A (Mbar)	B (Mbar)	C (Mbar)
ALUMINUM	0.7430	1.7400	0.3290
EPOXY	0.0528	0.3280	0.0379

6A-373(-500

FIG. 2.1 ELASTOPLASTIC CYCLE

For the elastic region, segment ab , (2.3) becomes

$$dp_x = (K_b + \frac{4}{3} G)\, d\varepsilon_x \tag{2.5}$$

where K_b is the bulk modulus and G the rigidity modulus. Using

$$K_b = \frac{E}{3}\left(\frac{1}{1 - 2\nu}\right) = \frac{d\bar{p}}{dV} \tag{2.5a}$$

$$G = \frac{E}{2(1 - \nu)} \tag{2.5b}$$

$$d\varepsilon = \frac{d\rho}{\rho} \tag{2.5c}$$

(2.5) can be written as

$$dp_x = 3\,\frac{1 - \nu}{1 + \nu}\, d\bar{p} \tag{2.6}$$

Taking ν as constant, (2.6) integrates to

$$p_{xe} = 3\frac{1-\nu}{1+\nu}\bar{p} \tag{2.7}$$

where the subscript e denotes the elastic segment ab. For uniaxial strain, the compressive stress normal to the direction of wave propagation is given by

$$dp_x = (K - 2\mu/3)d\varepsilon_x \tag{2.8}$$

and using (2.2) and (2.6), the resolved shear stress becomes

$$\tau = \frac{3}{2}\bar{p}\left(\frac{1-2\nu}{1+\nu}\right) \tag{2.9}$$

For the Tresca and the von Mises yield conditions in this geometry, the maximum resolved shear stress is determined by the yield stress $Y = 2\tau$. Consequently,

$$Y = 3\bar{p}\left(\frac{1-2\nu}{1+\nu}\right) \tag{2.10}$$

Along ae, (2.3) integrates to

$$p_{x\ell} - p_{xa} = \bar{p} - \bar{p}_a + \frac{2}{3}(Y - Y_a) \tag{2.11}$$

where the subscript ℓ denotes loading. Along fb,

$$p_{xu\ell} - p_{xf} = \bar{p} - \bar{p}_f - \frac{2}{3}(Y - Y_f) \tag{2.12}$$

where $u\ell$ denotes unloading. The other segments are determined in a similar manner.

For the foam (Model 3), the dependence of pressure upon specific volume is shown in Fig. 2.2. For the elastic states, the compressive stress in the direction of propagation is given by

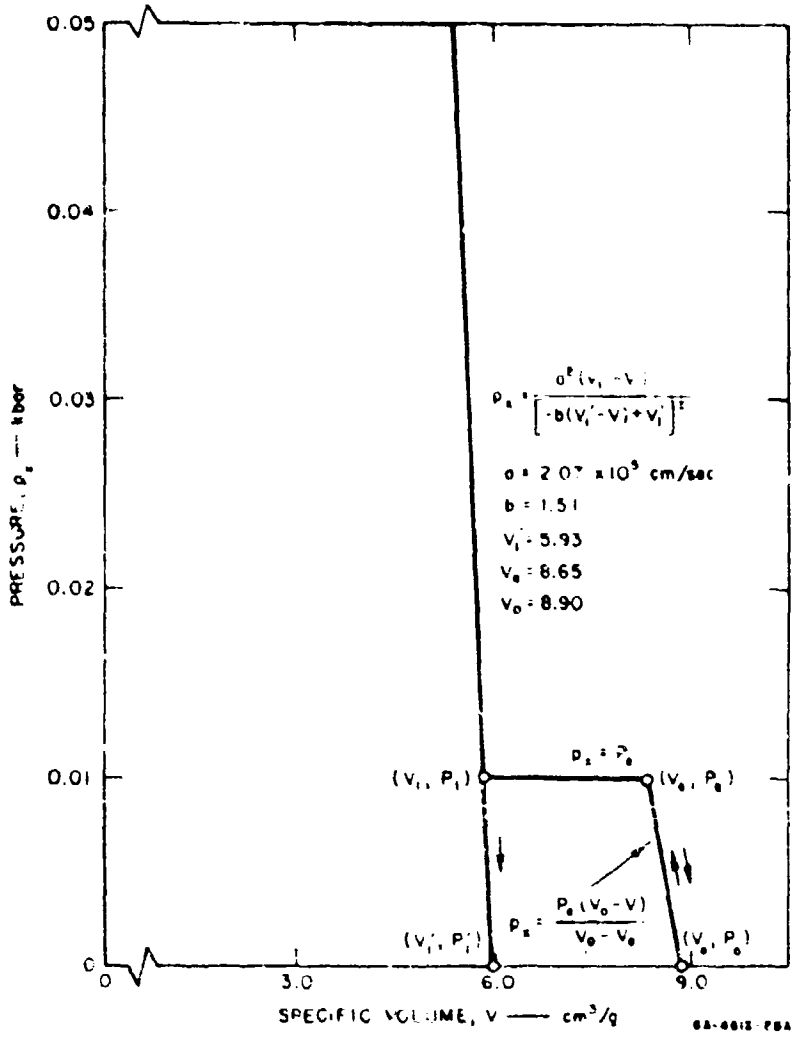

FIG. 2.2 LOCKING SOLID EQUATION OF STATE FOR FOAM

$$p_x = \frac{P_e(V_o - V)}{V_o - V_e} \qquad (2.13)$$

where P_e is the yield stress and $V = 1/\rho$. Between V_e and V_1

$$p_x = P_e \qquad (2.14)$$

As the material is compressed below V_1, the pressure is given by

$$p_x = \frac{a^2(V_1' - V)}{[-b(V_1' - V) + V_1']^2} \tag{2.15}$$

The equations of continuity and motion for one-dimensional flow in Lagrangian coordinates are

$$\rho_o \frac{\partial V}{\partial t} = \frac{\partial u}{\partial x} \tag{2.16}$$

$$\rho_o \frac{\partial u}{\partial t} = -\frac{\partial (p_x + Q)}{\partial x} \tag{2.17}$$

where u is particle velocity, and Q is the artificial viscosity parameter. In the code used here, Q was taken to be

$$Q = -\frac{1}{V}\frac{\partial u}{\partial x}\left(\left|\frac{\partial u}{\partial x}\right| i^2 + nc\right) \tag{2.18}$$

where $i = 1.7$, $n = 0.2$, and c is the local sound speed.

For the calculations, (2.16) and (2.17) were written in difference form, programmed in ALGOL, and integrated for the given initial conditions using the relations of Figs. 2.1 and 2.2 for the elastoplastic and foam layers. The program is characterized by the following progression of steps:

A. For each time step, the particle velocity is found in every cell;

B. the displacement of each cell is determined and the corresponding value of μ and V;

C. for the shield and base, p_x is determined as follows:

1. If μ is greater than that of the previous time step, loading occurs and

a. if the pressure $p_{x\ell}$ from (2.7) is above $p_{x\ell}$ from (2.11) the value of $p_{x\ell}$ is taken; otherwise

b. the pressure is in the elastic region and the value of p_{xe} is taken.

2. If μ is less than that of the previous time step, unloading occurs and

a. if p_{xe} is below p_{xui} from (2.12) the pressure is equated to p_{xui}, otherwise

b. the pressure is in the elastic unloading region and the value of p_{xe} is taken.

D. For the foam, if included, p_x is determined from (2.13) through (2.15), depending upon the value of the specific volume V.

The output of the calculations includes (1) the occurrence and time of spall, and (2) the time of separation and rebound velocity of the shield. The latter becomes the initial velocity for the structural displacement calculations.

2.2.2 Structural Displacement of the Shield

As outlined above, the structural model is taken as a ring behaving as a linear oscillator. The equation of motion for a linear oscillator (neglecting damping) is

$$\ddot{x} + \frac{k}{m} x = \frac{F(t)}{m} \tag{2.19}$$

where m is the mass, $F(t)$ the forcing function, and k the spring constant. In the present problem, k/m is related to the hoop modulus E_θ by

$$\frac{k}{m} = \frac{E_\theta}{\rho r_m^2} = \omega_m^2 \tag{2.20}$$

in which r_m is the mean radius of the shield. Since

$$E_\theta = \rho c_\theta^2 \tag{2.21}$$

and

$$\frac{c_r}{c_\theta} = \beta = \sqrt{\frac{1-\nu}{1+2\nu}} \tag{2.22}$$

(2.20) may be written

$$q_m = \frac{c_r}{\beta\, r_m} \tag{2.23}$$

Using (2.20) and (2.23), the solution to (2.19) may be written

$$x = x_s \cos q_m t + \frac{v_s}{c_m} \sin q_m t + \frac{1}{q_m} \int_o^t F(t) \sin q_m(t - t')dt' \tag{2.24}$$

or

$$x = x_s \cos q_m t + \frac{v_s}{q_m} \sin q_m t + G \cos q_m t + H \sin q_m t \tag{2.24a}$$

where

$$G = -\frac{1}{mq_m} \int_o^t F(t) \sin q_m t'dt' \tag{2.24b}$$

$$H = \frac{1}{mq_m} \int_o^t F(t) \cos q_m t'dt' \tag{2.24c}$$

and

x_s = initial displacement

t_g = time of separation

m = mass of shield = $\rho\pi(r_o^2 - r_i^2)$ (per unit length)

r_o = outer radius

r_i = inner radius

$F(t)$ = $P(t)$ x area = $P(t)\, 2\pi(r_m + \frac{h}{2} + x)$ (per unit length)

For exponential and triangular pulses respectively, we have

$$P(t) = P_o e^{-\lambda t} \qquad \text{(Fig. 2.3)}$$

$$P(t) = P_o\left(1 - \frac{t}{T}\right) \qquad \text{(Fig. 2.4)}$$

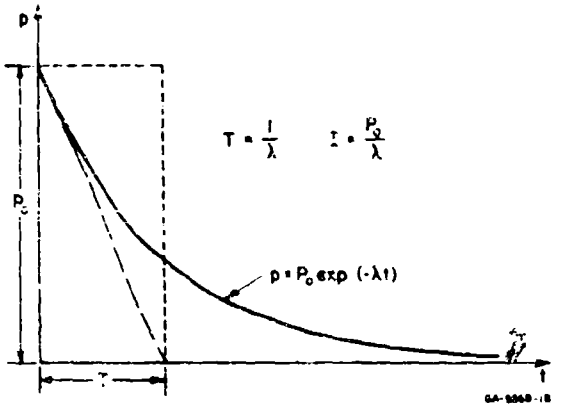

FIG. 2.3 EXPONENTIAL PULSE

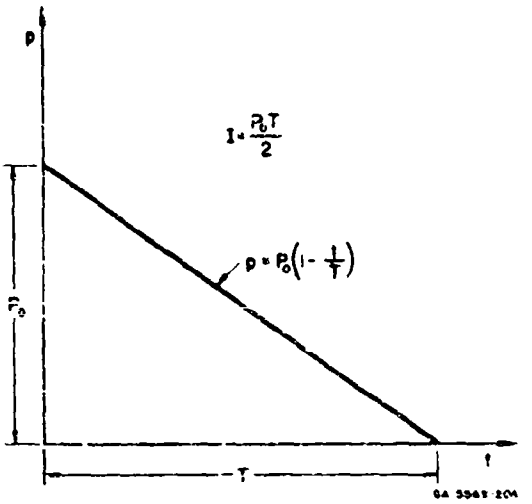

FIG. 2.4 TRIANGULAR PULSE

Substituting these into the above equations and integrating yields

$$x = \frac{x_s \cos q_m t + \frac{v_s}{q_m} \sin q_m t + SF}{1 - SF} \qquad (2.25)$$

where

$$S = \frac{P_o \beta \left(r_m + \frac{h}{2}\right)}{\rho c h} \qquad (2.25a)$$

and

$$F = \frac{1}{\lambda^2 + q_m^2} \left\{ q_m e^{-\lambda t} - e^{-\lambda t_s} \left[-\lambda \sin q_m(t - t_s) + q_m \cos q_m(t - t_s) \right] \right\}$$

(exponential) (2.25b)

or

$$F = \frac{1}{q_m} \left\{ 1 - \frac{t}{T} + \left(\frac{t_s}{T} - 1\right) \left[\cos q_m(t - t_s) + \frac{1}{q_m T} \sin q_m(t - t_s) \right] \right\}$$

(triangular) (2.25c)

2.2.3 Failure Criteria

Spall Stress. Spall failure was assumed to occur in the epoxy shield if the tensile stress exceeded the yield stress of the epoxy, 3.0 kbar.

Critical Velocity for Cracking--Short Pulses. If the incident pulse does not act beyond separation, a critical separation velocity sufficient to develop hoop stresses to the point of cracking may be defined. The residual velocity at separation is the average particle velocity across the layer at time of separation. If v_s is the residual velocity at separation, the kinetic energy (per unit area) is

$$KE = \frac{1}{2} \rho h (v_s)^2 \qquad (2.26)$$

For uniform radial displacement, the strain energy is

$$SE = \frac{1}{2} \frac{h}{E_\theta} \sigma_\theta^2 \qquad (2.27)$$

where E_θ is the modulus in the circumferential direction. Equating the strain energy (2.27) to the kinetic energy at separation yields

$$\sigma_\theta^2 = 2 \frac{E_\theta}{h} (KE) \qquad (2.28)$$

For the critical condition, σ_θ becomes the maximum hoop stress $\sigma_{\theta cr}$. Using (2.26) and solving or v_s yields the critical separation velocity

$$v_{cr} = \frac{\sigma_{\theta cr}}{\sqrt{E_\theta \rho}} \tag{2.29}$$

Using (2.21) and (2.22), (2.29) may be written

$$v_{cr} = \frac{\beta \sigma_{\theta cr}}{\rho c} \tag{2.30}$$

Taking $\sigma_{\theta cr}$ = 3 kbar,

$$v_{cr} = 12.88 \text{ cm/ms}$$

Critical Displacement for Cracking--Long Pulses. Pulses which act after separation must be accounted for in calculating the structural displacement of the shield. From Hooke's law

$$\frac{r - r_{Bi}}{r_m} = \sigma_\theta E_\theta \tag{2.31}$$

where r is the radial displacement of the mean radius r_m. Using (2.21) and (2.22), and putting $\Delta x_{cr} = (r_{cr} - r_m)$, $\sigma_\theta = \sigma_{\theta cr}$, (2.31) yields

$$\Delta x_{cr} = \sigma_{\theta cr} \frac{\beta^2}{\rho c_r} r_m \tag{2.32}$$

For the properties of Table 2.1 the critical displacement for the epoxy shield is

$$\Delta x_{cr} = 2.48 \text{ cm}$$

2.3 Results

2.3.1 Introduction

The results are presented in two parts. First the results for the two-layered composite with a thick base are given; these show the effects of differences in the constitutive relations for an exponential pulse and comparing the effects of exponential and triangular pulses. Next, the results are given for the two-layered composite with a thin base and the three-layered composite with a thin base and a thick foam layer, all for an exponential pulse.

2.3.2 Model 1--Two-Layered Composite with a Thick Base

Exponential Pulse. Critical load boundaries for rebound cracking of the shield were generated for an exponential pulse (Fig. 2.3) applied to an epoxy shield and aluminum base described by the model of Fig. 2.1. Effects of differences in material properties were examined for the following cases:

1. Nonlinear-Nonelastic [A, B, C $\neq$ 0 in (2.4)]
2. Nonlinear-Elastic ($p_{xa} = \infty$ in Fig. 2.1)
3. Linear-Elastic (B, C = 0; $p_{xa} = \infty$)
4. Linear-Nonelastic (B, C = 0)

The differences between the nonlinear and linear constitutive relations can be seen in Fig. 2.5.

Figures 2.6a and 2.6b show the results of the computer runs and the cracking boundaries determined from them.* As expected, the boundaries all exhibit a minimum, are impulse-dependent for low impulses, and rise monotonically beyond the minimum. Spall occurred as shown.

*See Tables 2.2 through 2.5 for numerical values.

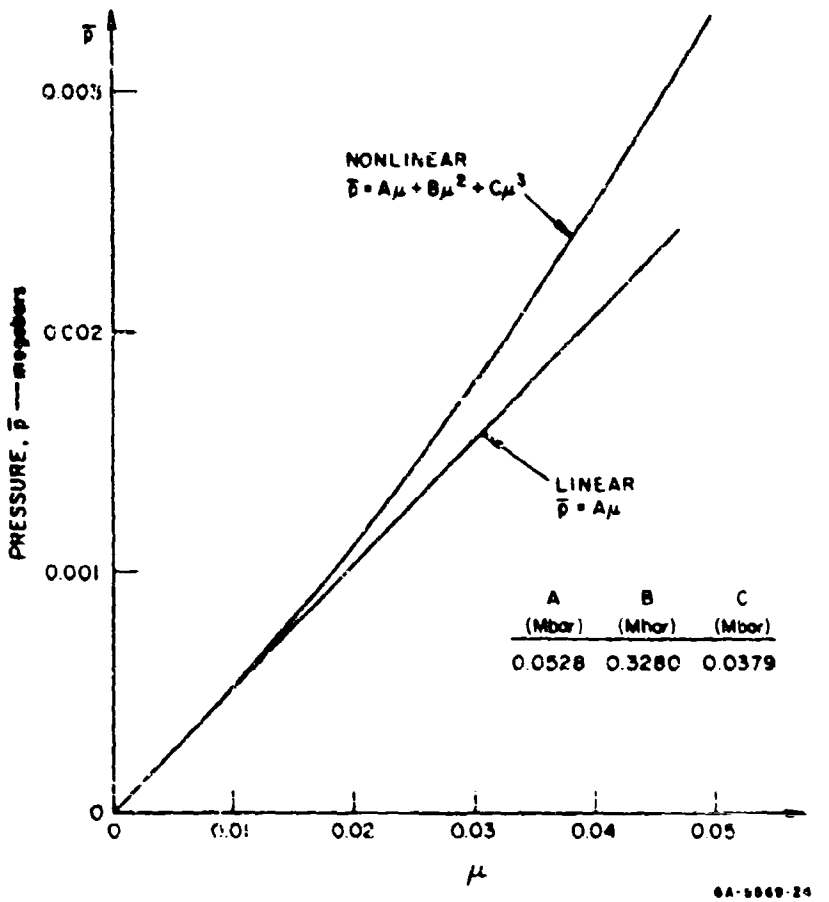

FIG. 2.5 COMPARISON OF NONLINEAR AND LINEAR EQUATIONS OF STATE FOR EPOXY

Effects of Differences in Constitutive Relations of Shield and Base. Effects of differences in the constitutive relations of the shield and base are shown in Fig. 2.6c (obtained from 2.6a and b). For the range of differences considered here, nonlinear effects (i.e., B, C $\neq$ 0) are much more significant than plasticity effects.

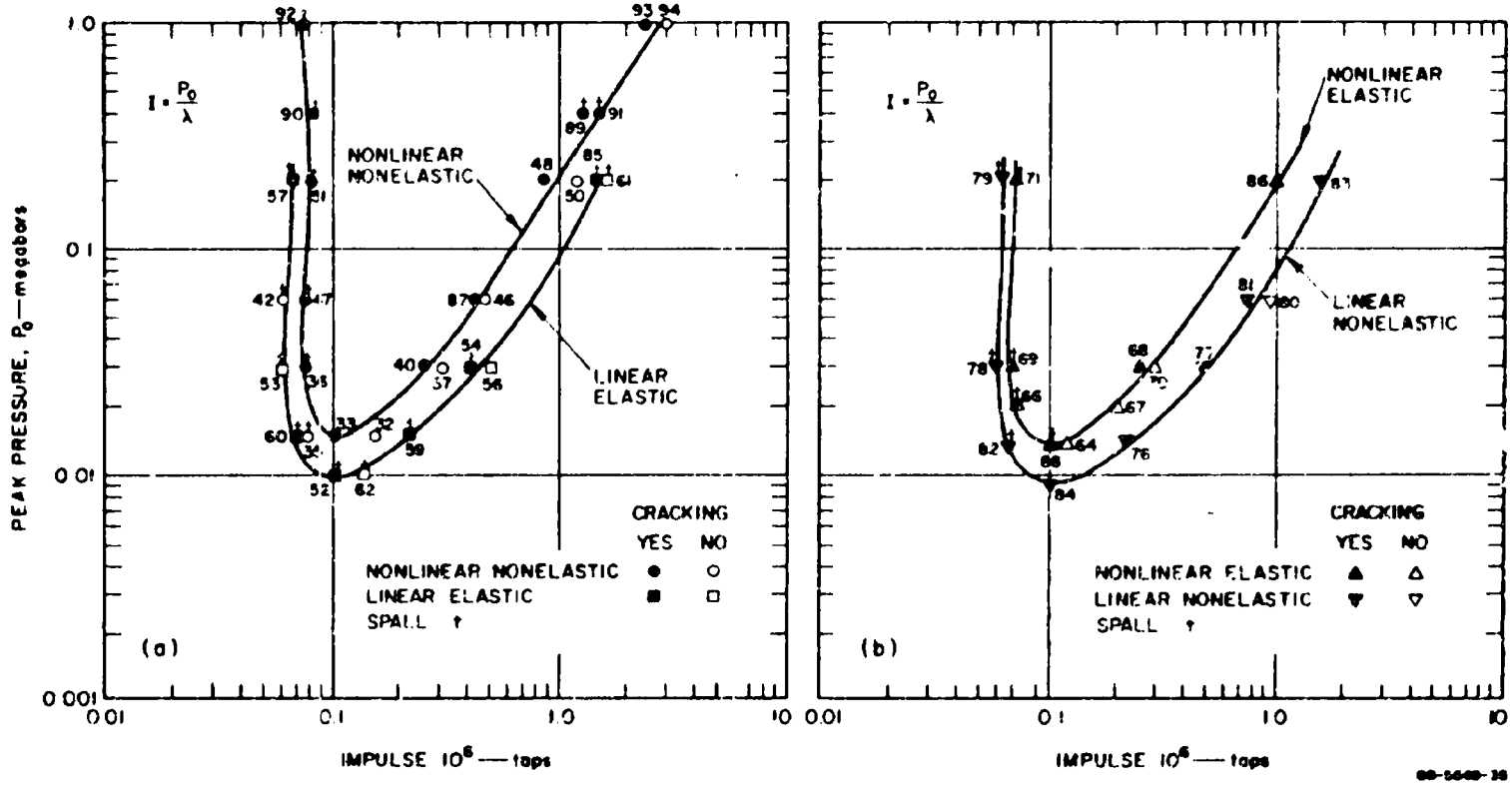

FIG. 2.6 CRACKING BOUNDARIES FOR EXPONENTIAL PULSES
(a) Nonlinear-nonelastic, linear-elastic
(b) Nonlinear-elastic linear-nonelastic

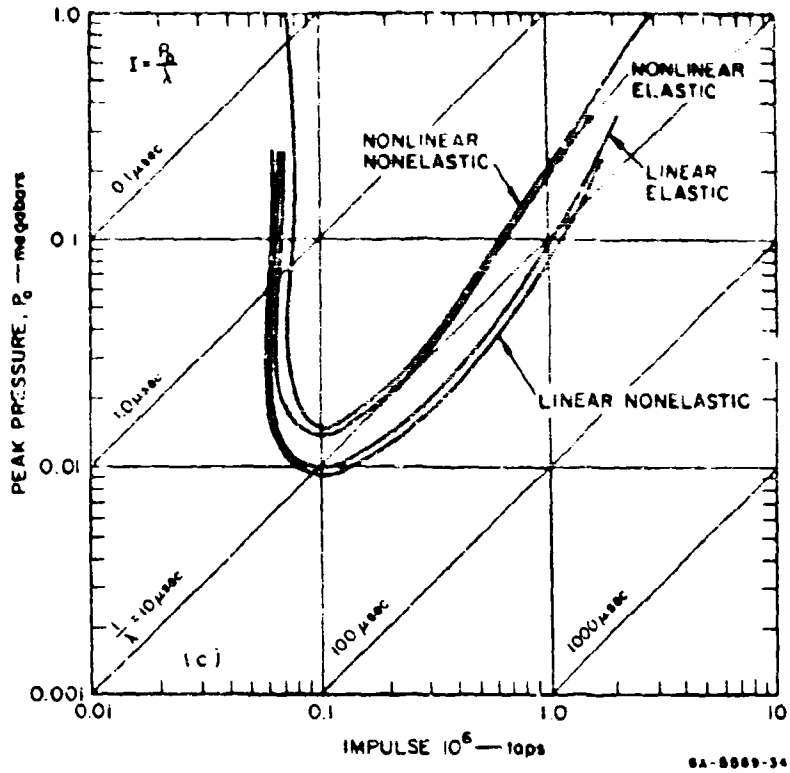

FIG. 2.6 (Concluded) CRACKING BOUNDARIES FOR EXPONENTIAL PULSES
(c) (a) and (b) combined

Nonlinear effects result in a difference of about 40% in critical pressure at the minimum. To the right of the minimum, nonlinear effects produce differences of about 40% or less in both pressure and impulse. To the left of the minimum (in the region where the curves rise rapidly) only the impulse is significant and differences in impulse due to nonlinear effects are about 15%. In contrast to the nonlinear effects, plasticity effects result in differences of less than 10% everywhere.

Nonlinearities affect the critical load curves primarily through increases in shock velocity with pressure, which result in earlier separation for the nonlinear material. This decreases the rebound velocity and, due to the higher load remaining at the earlier separation, causes the shield to experience more rapid deceleration after separation. Thus, the load amplitude required to develop a given displacement will be higher for the nonlinear material.

Table 2.2

EXPONENTIAL PULSE (NONLINEAR-NONELASTIC)

P (MBar)	λ (μsec^{-1})	I (10^6 taps)	Run	Time of Separation (μsec)	Separation Velocity (cm/msec)	Maximum Displacement (cm)	Crack	Spall Time (μsec)
1.00	13.2	0.076	92	20.25	- 14.9	- 2.87	yes	13.26
1.00	0.4	2.50	93	14.11	- 19.9	- 3.20	yes	none
1.00	0.33	3.00	94	20.00	- 11.4	- 1.90	no	none
0.40	4.8	0.083	90	20.38	- 15.1	- 2.92	yes	12.39
0.40	0.308	1.30	89	13.82	- 38.8	- 6.10	yes	13.74
0.40	0.667	1.50	91	15.67	- 21.2	- 2.55	yes	none
0.20	2.60	0.08	51	21.81	- 13.0	- 2.51	yes	14.18
0.20	2.30	0.087	49	21.55	- 14.0	- 2.70	yes	13.96
0.20	0.25	0.87	46	14.67	- 37.0	- 4.94	yes	none
0.20	0.17	1.176	50	20.19	- 3.0	- 1.31	no	none
0.08	1.0	0.08	42	23.24	- 11.0	- 2.12	no	16.16
0.08	0.80	0.075	47	22.68	- 13.0	- 2.54	yes	18.90
0.08	0.70	0.086	43	22.28	- 14.8	- 2.85	yes	15.65
0.08	0.15	0.40	45	17.55	- 29.7	- 3.67	yes	none
0.08	0.137	0.438	87	17.47	- 28.0	- 2.50	yes	none
0.06	0.13	0.461	46	17.90	- 25.6	- 1.83	no	none
0.06	0.12	0.50	44	18.71	- 21.0	- 0.60	no	none
0.03	0.40	0.075	36	23.30	- 13.6	- 2.64	yes	17.81
0.03	0.15	0.20	38	20.85	- 22.0	- 3.67	yes	none
0.03	0.12	0.25	40	20.47	- 21.3	- 2.61	yes	none
0.03	0.10	0.30	37	20.24	- 19.0	- 1.10	no	none
0.015	0.325	0.046	34	25.31	- 8.7	- 1.67	no	20.98
0.015	0.20	0.075	35	24.20	- 12.6	- 2.35	close	22.55
0.015	0.15	0.10	33	23.63	- 14.0	- 2.52	yes	none
0.015	0.10	0.15	32	23.15	- 14.0	- 1.71	no	none

Table 2.3

EXPONENTIAL PULSE (LINEAR-ELASTIC)

P (MBar)	λ (μsec^{-1})	I (10^6 taps)	Run	Time of Separation (μsec)	Separation Velocity (cm/msec)	Maximum Displacement (cm)	Crack	Spall Time (μsec)
0.20	3.5	0.057	55	19.00	- 11.0	- 2.12	no	17.93
0.20	3.0	0.067	57	26.45	- 13.6	- 2.40	close	17.67
0.20	0.137	1.46	85	19.00	- 68.0	- 5.16	yes	18.93
0.20	0.13	1.54	61	19.78	- 52.3	- 2.07	no	19.66
0.20	0.11	1.82	58	23.21	- 13.1	- 0.66	no	none
0.03	0.50	0.06	53	27.94	- 12.2	- 2.30	no	19.60
0.03	0.075	0.40	54	26.02	- 39.0	- 5.62	yes	25.96
0.03	0.06	0.50	86	25.78	- 38.0	- 1.17	no	none
0.015	0.22	0.068	60	28.85	- 13.7	- 2.64	yes	20.93
0.015	0.07	0.214	59	28.42	- 23.0	- 2.48	yes	28.53
0.01	0.10	0.10	52	29.44	- 15.2	- 2.57	yes	26.57
0.01	0.075	0.13	62	29.38	- 16.3	- 2.15	no	28.04

Table 2.4

EXPONENTIAL PULSE (LINEAR-NONPLASTIC)

P (Mbar)	λ (μsec^{-1})	I (10^6 taps)	Run	Time of Separation (μsec)	Separation Velocity (cm/msec)	Maximum Displacement (cm)	Crack	Spall Time (μsec)
0.20	0.1	0.064	79	28.75	- 13.2	- 2.64	yes	19.65
0.20	0.13	1.34	83	23.15	- 40.8	- 2.59	yes	none
0.06	0.081	0.741	81	24.10	- 57.7	- 3.81	yes	none
0.060	0.065	0.923	80	25.03	- 44.9	- 0.73	no	none
0.030	0.50	0.06	78	29.90	- 12.9	- 2.50	yes	22.08
0.030	0.065	0.462	77	27.80	- 40.3	- 2.72	yes	none
0.015	0.23	0.065	82	30.39	- 14.0	- 2.70	yes	23.30
0.015	0.07	0.214	76	30.40	- 24.0	- 2.88	yes	none
0.012	0.10	0.12	74	30.74	- 18.6	- 3.19	yes	28.94
0.0105	0.10	0.105	75	30.93	- 16.2	- 2.79	yes	29.40
0.0093	0.093	0.10	64	30.95	- 14.6	- 2.43	close	none

Table 2.5

EXPONENTIAL PULSE (NONLINEAR-ELASTIC)

P (Mbar)	λ (μsec^{-1})	I (10^6 taps)	Run	Time of Separation (μsec)	Separation Velocity (cm/msec)	Maximum Displacement (cm)	Crack	Spall Time (μsec)
0.20	2.80	0.071	71	21.19	- 13.2	- 2.55	yes	13.19
0.20	0.23	0.87	73	13.10	- 45.2	- 5.52	yes	none
0.20	0.202	0.986	86	14.98	- 30.0	- 2.42	close	none
0.20	0.19	1.053	72	16.04	- 22.0	- 0.81	no	none
0.03	0.44	0.068	69	22.76	- 13.8	- 2.68	yes	15.51
0.03	0.12	0.25	68	19.18	- 24.3	- 2.93	yes	none
0.03	0.107	0.28	70	18.69	- 83.4	- 2.00	no	none
0.02	0.28	0.071	66	23.21	- 14.2	- 2.74	yes	16.79
0.02	0.10	0.20	67	20.76	- 49.1	- 1.97	no	none
0.015	0.15	0.10	65	22.88	- 15.8	- 2.81	yes	20.68
0.014	0.14	0.10	88	23.03	- 15.2	- 2.66	yes	21.64
0.014	0.12	0.117	64	22.90	- 13.5	- 2.08	no	none
0.012	0.10	0.12	63	23.88	- 12.2	- 1.58	no	none

Triangular Pulse. The cracking boundary for a triangular pulse for the nonlinear, nonelastic case* is given in Fig. 2.7 together with that for an exponential pulse. The curves coincide in the impulse-sensitive region, as expected. The minimum for the triangular pulse is about 50% below that for the exponential pulse. To the right of the minimum the curves differ by about 30%.

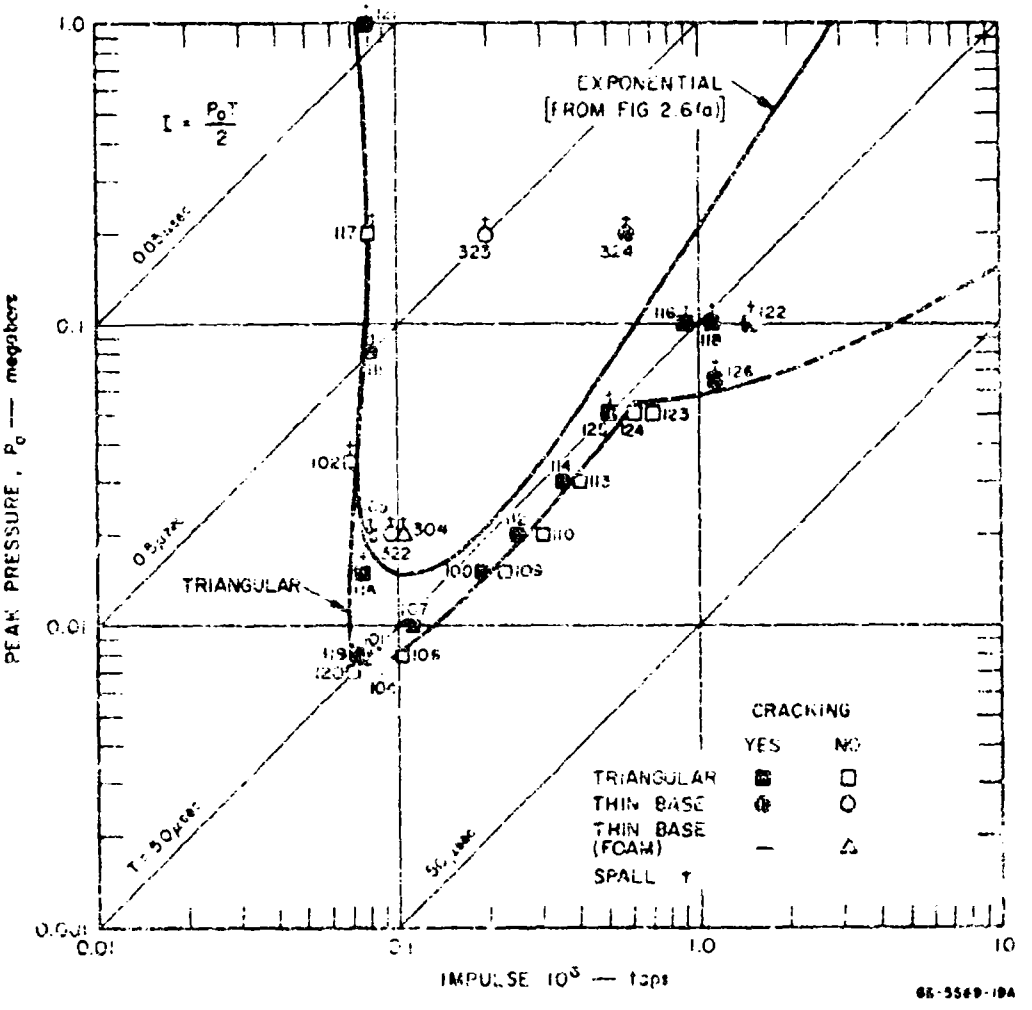

FIG. 2.7 CRACKING BOUNDARIES FOR EXPONENTIAL AND TRIANGULAR PULSES FOR NONLINEAR, NONELASTIC CASE

*See Table 2.6 for numerical values.

The triangular pulse differs from the exponential in that, for the same peak pressure and total impulse, the exponential pulse has a higher initial decay rate and a longer duration. Thus, for triangular and exponential pulses of the same peak pressure in the region where curves rise to the right, less reflected momentum (from the base) is realized for the exponential pulse and more of the pulse acts after separation. Thus, to develop the same maximum displacement for a given peak pressure, the exponential pulse requires a shorter duration and hence less momentum.

Above 0.05 Mbar in the region where the curve rises to the right, the numerical results suggest that a distinct break exists in the critical boundary. This is different from the exponential results which show a continuously rising curve. The dashed line is the boundary as it would be expected to develop for increasing values of impulse.

2.3.3 Model 2--Two-Layered Composite with a Thin Base

To provide a basis for evaluating the effect of a third layer of foam, a few cases were run without the foam. The model is described in Table 2.1. The calculations, employing the nonlinear-nonelastic constitutive relation and exponential pulse, indicated that the rarefaction from the free surface of the base caused greater inward particle velocities to be realized in the base than in the shield. As a result, the base separated from the shield when the rarefaction arrived at the interface. Because the average velocity of the base was over three times larger than that of the shield, it was assumed that the shield would not re-impact the base during the inward motion. After separation, the shield motion was regarded as a linear oscillator. As before, cracking was taken to occur if the outward displacement exceeded 2.48 cm. Although the inward displacement was usually equal to or greater than the outward displacement, failure in tension was assumed. This is reasonable for a material with a yield strength in compression which exceeds that in tension.

The results are indicated in Fig. 2.7 by the points labeled 322, 323, and 324.* Although all three points are within the cracking region for a thick base, only 324 exhibited cracking.

2.3.4 Model 3--Three-Layered Composite (Thin Base with Foam)

For this model the thin base used for the calculations described immediately above was backed with a thick layer of rigid polyurethane foam of density 7 lb/ft^3 (see Table 2.1 and Fig. 2.2). The foam would be expected to affect the results by attenuating the rarefaction wave from the back surface of the base.

The results of the calculations are indicated in Fig. 2.7 by the point labeled 304. The maximum outward displacement was 2.25 cm. For the same load (point 322), the thin base without foam gave a maximum outward displacement of 2.29 cm. Thus, the foam did not significantly affect the response.

A foam of greater density might have prevented the base from separating as a result of the free surface rarefaction. This would have increased the time during which the foam could influence the momentum exchange with the shield and the affect on the velocity of the rebounding shield would have been more pronounced.

*See Table 2.7 for numerical values.

Table 2.6

TRIANGULAR PULSE (NONLINEAR-NONELASTIC)

P (Mbar)	λ (μsec^{-1})	I (10^6 taps)	Run	Time of Separation (μsec)	Separation Velocity (cm/msec)	Maximum Displacement (cm)	Crack	Spall Time (μsec)
1.00	0.16	0.08	121	21.19	- 13.5	- 2.61	yes	13.97
0.20	0.80	0.05	117	21.56	- 12.8	- 2.47	close	13.68
0.10	30.0	1.50	122	35.2	- 24.4	- 4.80	yes	33.05
0.10	22.0	1.10	118	28.7	- 22.0	- 4.34	yes	24.7
0.10	18.0	0.90	116	22.09	- 25.0	- 4.81	yes	19.31
0.08	2.0	0.08	111	22.15	- 12.9	- 2.48	yes	14.3?
0.07	30.0	1.05	126	35.99	- 21.1	- 4.12	yes	33.93
0.07	28.0	0.7	123	35.12	- 11.3	- 2.22	no	none
0.06	24.0	0.6	124	28.07	- 11.1	- 2.17	no	none
0.05	20.0	0.5	125	21.95	- 24.0	- 4.56	yes	20.9
0.035	4.0	0.07	102	23.23	- 12.2	- 2.34	close	16.36
0.03	27.0	0.405	113	26.98	- 9.0	- 1.85	no	none
0.03	23.0	0.345	114	23.2	- 19.0	- 3.61	yes	none
0.02	30.0	0.30	110	27.9	- 8.0	- 1.51	no	none
0.02	25.0	0.25	112	24.1	- 15.6	- 3.01	yes	none
0.02	4.0	0.08	105	23.52	- 20.0	- 2.84	yes	18.5
0.01	30.0	0.23	109	27.19	- 9.0	- 1.81	no	none
0.015	25.0	0.19	108	23.47	- 15.0	- 2.97	yes	none
0.015	10.0	0.075	115	24.05	- 14.0	- 2.72	yes	20.06
0.01	22.0	0.11	107	24.26	- 15.0	- 2.91	yes	none
0.008	25.0	0.1	106	23.12	- 12.0	- 2.27	no	none
0.008	20.0	0.08	101	25.03	- 13.3	- 2.56	yes	none
0.008	18.0	0.072	119	25.07	- 13.0	- 2.54	yes	none
0.0072	25.0	0.09	104	25.4	- 11.0	- 2.14	no	none
0.007	20.0	0.07	120	25.48	- 12.0	- 2.32	close	none
0.006	30.0	0.09	103	28.07	- 8.0	- 1.58	no	none

Table 2.7

THIN-BASE MODEL (EXPONENTIAL PULSE, NONLINEAR, NONELASTIC)

P (Mbar)	λ (μsec^{-1})	I (10^6 taps)	Run	Time of Separation (μsec)	Separation Velocity (cm/msec)	Maximum Displacement	Crack	Spall Time (μsec)	Remarks
0.2	0.333	0.6	324	8.65	79.13	- 15.46	yes	8.54	...
0.2	1.0	0.2	323	9.15	11.10	- 2.22	no	7.78	...
0.02	0.2	0.1	322	14.34	10.83	- 2.29	no	16.33	...
0.02	0.2	0.1	304	14.49	10.65	- 2.25	no	16.39	third layer foam

SECTION 3

LINEAR ELASTIC ANALYSIS--INTRODUCTION AND RESULTS

3.1 Introduction

As mentioned earlier, the purpose of the analysis presented in this and the following section is to provide insight into the stress-wave action which results in rebound cracking and spalling and to provide checks on the numerical calculations presented in Section 2. As in the numerical calculations, the basic model taken is a thin shield over a thick base with zero bond strength across the interface. One-dimensional linear wave theory is used to calculate the response of the laminate to a uniform loading with a step rise and exponential decay. Cracking occurs if the circumferential tensile stress exceeds a critical value σ_{cr}, and spalling occurs if the radial tensile stress exceeds a critical value σ_{sp}, in general different from σ_r. Since the problem is linear, the stresses generated are proportional to the peak pressure P. Thus, for the circumferential and radial stresses σ_θ and σ_r, we may write

$$\sigma_\theta = PC(a_i) \qquad \sigma_r = PS(a_i)$$

where C and S depend through the a_i on the pulse shape factor ϕ defined by $p = P\phi(t)$, and on material properties. Then for cracking we have

$$P \geq P_{cr} = \frac{\sigma_{cr}}{C(a_i)} \tag{3.1a}$$

and for spalling

$$P \geq P_{sp} = \frac{\sigma_{sp}}{S(a_i)} \tag{3.1b}$$

The relations (3.1) define failure boundaries once the functions $C(a_i)$ and $S(a_i)$ are known. The method for calculating these functions and the corresponding failure boundaries is given in Section 4 for pulses with a step rise and exponential decay. The remainder of this section gives a comparison of the failure boundaries so found with those from the numerical analysis of Section 2.

3.2 Results

Figure 3.1 shows the cracking boundaries for pulses with a step rise and an exponential decay. The two upper curves are from the numerical analysis and are the same as those of Fig. 2.6. The lower curve is from the graphical analysis and is obtained from Fig. 4.14, using the material properties and dimensions for Model 1 from Table 2.1.

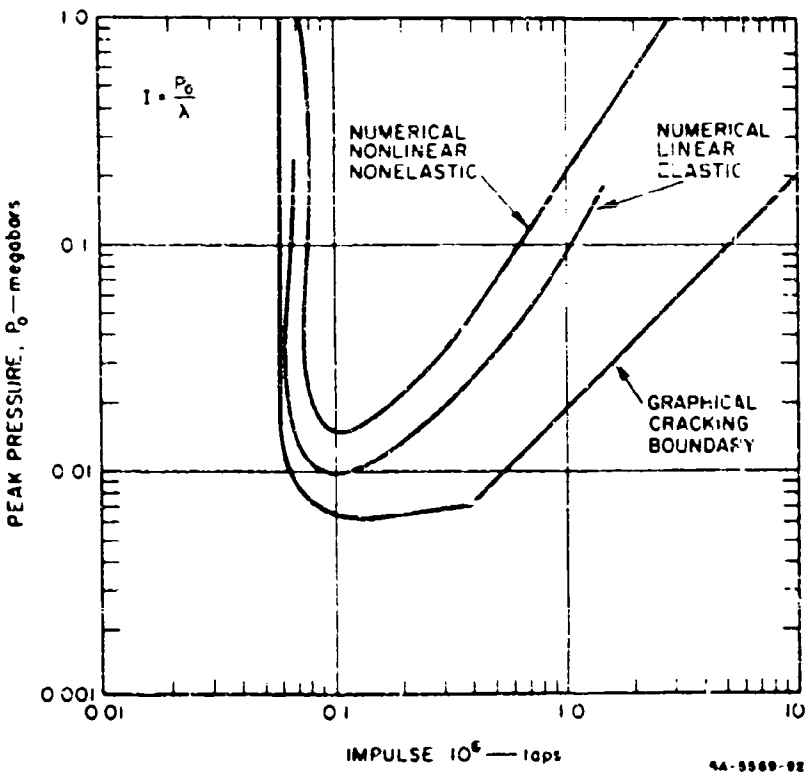

FIG. 3.1 CRACKING BOUNDARY FOR EXPONENTIAL PULSES

The failure boundary from the graphical analysis lies below the boundary from the numerical analysis, with the difference becoming greater at high impulses. The difference is attributed to the effects of the load acting after separation and to the contribution of particle velocity to the wave propagation velocity, which are accounted for in the numerical analysis but not in the graphical analysis. Both of these effects would be expected to raise the failure boundary and would be greater at larger impulses (longer pulse duration), in agreement with Fig. 3.1.

Figure 3.2 shows the graphical spall boundary for exponential pulses. The spall region to the right of the dashed line of unit slope is due to the effect of recombination at the shield-base interface. The results of the numerical calculations are given by the points, the crosses indicating spalling. The distribution of the points, which was chosen to determine the cracking boundary, is not ideal for comparison with the graphical spall boundary. However, the points that are available agree well. The most significant agreement is near the center of the middle square, where spall and no-spall points come close to bracketing the graphical boundary. The difference is attributed to the effect of particle velocity on wave velocity.

The foregoing comparisons show agreement between the numerical and graphical solutions. The major difference in the cracking boundaries from the two methods is attributed to the effects of the load acting after separation and of particle velocity on wave velocity. The points available from the numerical analysis are consistent with the graphical spall boundary, but more points are needed to establish the significance of the protrusion attributed to the effect of separation.

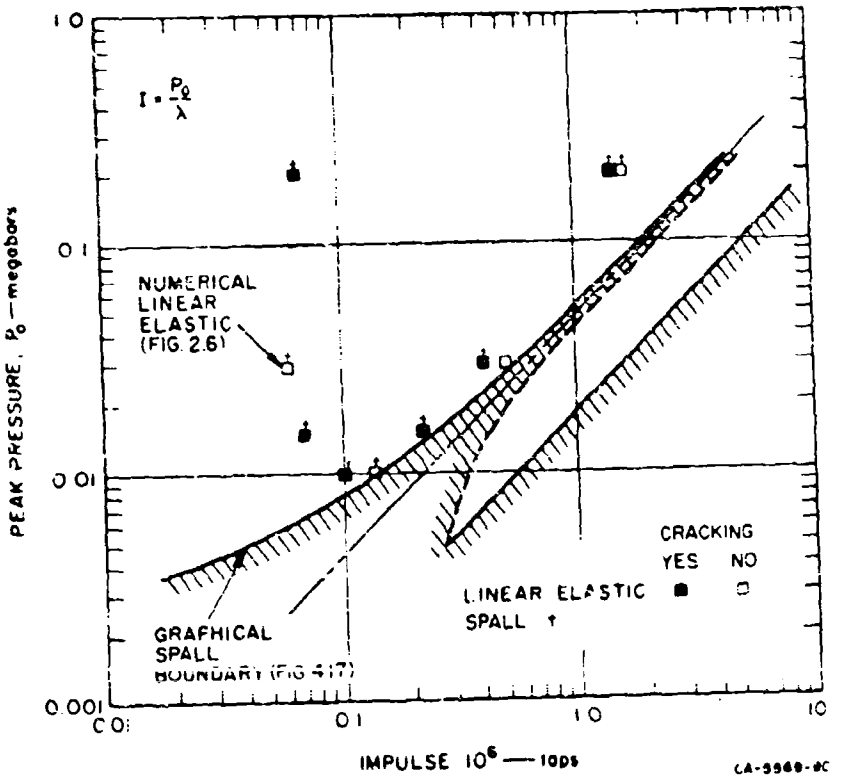

FIG. 3.2 SPALL BOUNDARY FOR EXPONENTIAL PULSES

SECTION 4

CRACKING AND SPALLING BOUNDARIES FOR EXPONENTIAL PULSES FROM GRAPHICAL ANALYSIS

4.1 Introduction

In this section cracking and spalling boundaries are determined for exponential pulses using a semigraphical procedure based on the method of characteristics.

4.2 One-Dimensional Linear Wave Theory

The wave equation for linear one-dimensional stress waves is

$$\frac{\partial^2 y}{\partial t^2} = c^2 \frac{\partial^2 y}{\partial x^2} \tag{4.1}$$

where y is displacement, t is time, x is the space coordinate, and c is the wave propagation velocity. On the straight lines (characteristics) in the x,t plane

$$x = \pm ct + \text{constant} \tag{4.2}$$

Substituting (4.2) into (4.1) yields

$$c \frac{\partial y}{\partial x} = \pm \frac{\partial y}{\partial t} + \text{constant} \tag{4.3}$$

Taking p for pressure and ρ for density, Hooke's law may be written

$$p = -\rho c^2 \frac{\partial y}{\partial x} \tag{4.4}$$

Substituting (4.4) and

$$u = \frac{\partial y}{\partial t}$$

into (4.3) yields

$$p = \mp \rho c u + \text{constant} \tag{4.5}$$

Thus, along the lines $x = \pm ct + \text{constant}$, the relations $p = \mp \rho c u + \text{constant}$ hold.

We now derive a basic relation between loading surface states at t_o and $t_o + \tau$, where τ is twice the transit time of the shield ($2h/c$). Figure 4.1a shows an x,t diagram for a two-layered (thick base) laminate. The characteristics C_o^+ and C_o^- are lines of $x = \pm ct + \text{constant}$ in the shield, and the characteristic C_{bo}^+ is a line of $x = c_b t + \text{constant}$ in the base. From the preceding discussion, C_b^+ characteristics in the x,t plane map into Γ_b^- characteristics in the u,p plane (Fig. 4.1b). However in the absence of C_b^- characteristics, the u,p state behind C_{bo}^+ must be constant. Therefore, the mapping of C_{bo}^+ in the u,p plane degenerates to a point. Moreover, in the absence of C_b^- characteristics, all the states in the base must lie on the same Γ_b^+. For an initial state $u = p = 0$ in the base, this must be Γ_{bo}^+ as indicated. Since the states in the base are also interface states, Γ_{bo}^+ is the line of interface states.

As can be seen from Fig. 4.1a, along the loading surface $x = 0$ the points $t = t_o$ and $t = t_o + \tau$ are connected by the characteristics C_o^+ and C_o^-, which meet at the interface. Therefore, as shown in Fig. 4.1b, the state u_o, p_o at $t = t_o$ and the state u,p at $t = t_o + \tau$ must be connected to the interface state $\bar{u},\bar{p}$ by Γ_o^- and Γ_o^+. Hence, we may write

$$\begin{aligned} \bar{p} &= \rho_b c_b \bar{u} \\ \bar{p} - p_o &= -\rho c(\bar{u} - u_o) \\ \bar{p} - p &= \rho c(\bar{u} - u) \end{aligned} \tag{4.6}$$

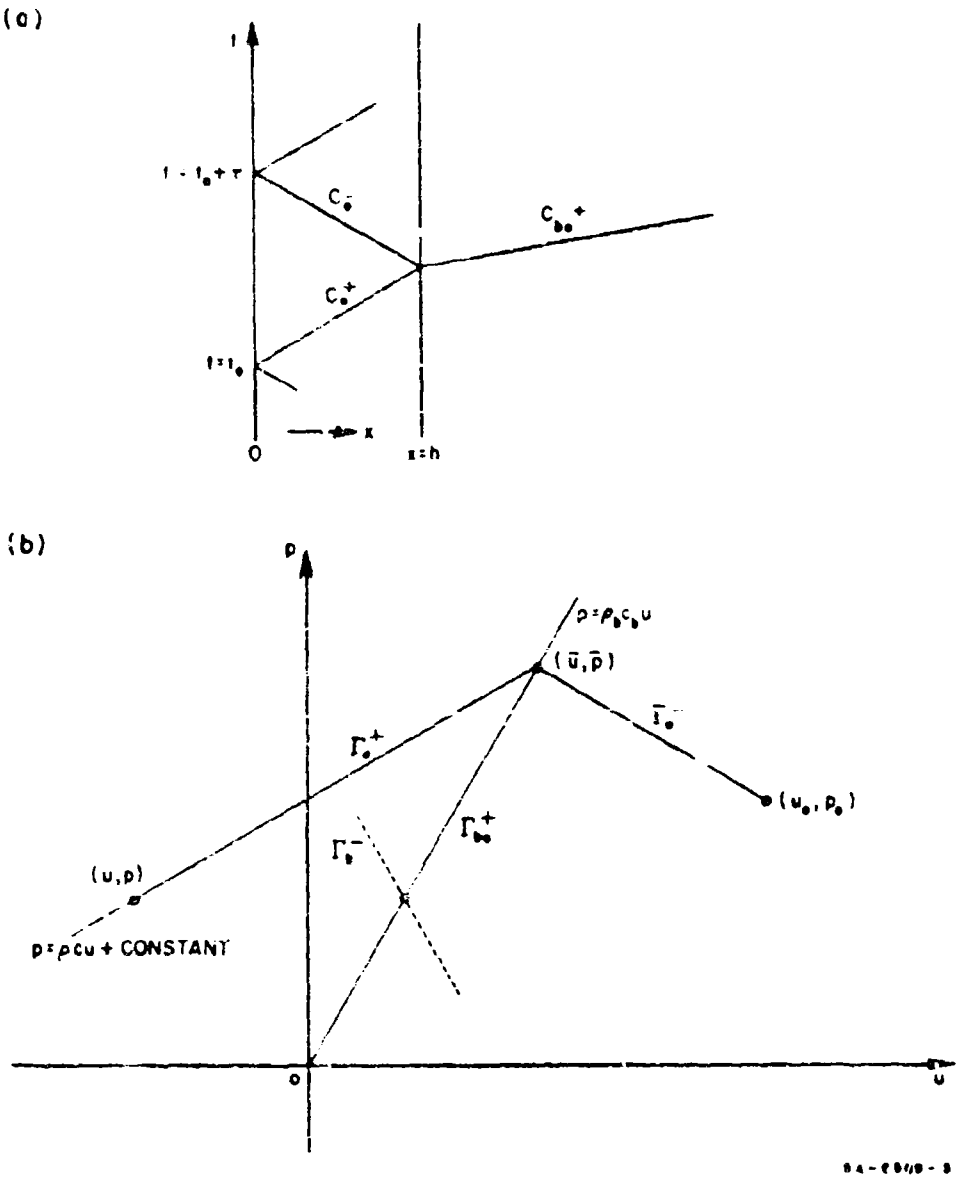

FIG. 4.1 SCHEMATIC x, t AND u, p DIAGRAMS WITH NOTATION

Eliminating $\bar{p}$ and $\bar{u}$ yields for the relation between loading surface states at t_o and $t_o + \tau$,

$$p - \rho c u = K(p_o + \rho c u_o) \tag{4.7}$$

where K is the reflection coefficient defined as*

$$K = \frac{1 - \frac{\rho c}{\rho_b c_b}}{1 + \frac{\rho c}{\rho_b c_b}} \tag{4.8}$$

4.3 Exponential Pulses

For an exponential pulse,

$$p_o = Pe^{-\lambda t_o} \qquad p = Pe^{-\lambda(t_o + \tau)}$$

Hence,

$$\frac{p}{p_o} = e^{-\lambda\tau} \tag{4.9}$$

To simplify the equations in the following, we will use

$$e = e^{-\lambda\tau} \tag{4.10}$$

Also, we adopt a slope factor n given by

$$p_o = n\rho c\, u_o \tag{4.11}$$

to denote the slope of the line connecting u_o, p_o (the state at t_o) with the origin.

Using (4.9) and (4.11) to eliminate u_o and p_o from (4.7) yields

$$p = \rho c u \frac{ne}{ne - (n + 1)K} \tag{4.12}$$

*For simplicity this expression is denoted by K instead of K_r as used elsewhere.

For given laminate materials, (4.12) gives the relation between u and p at $t = t_o + \tau$, in terms of the slope factor n.

Should separation occur at $t_o + 0.5\tau$, the interface condition becomes $p = 0$. This corresponds to $\rho_b = 0$ and, from (4.8), to $K = -1$. Thus, if separation occurs, instead of (4.12) we have

$$p = \rho cu \frac{ne}{ne + (n + 1)} \tag{4.13}$$

The second equation of (4.6) is a relationship between a loading surface state u_o, p_o and the corresponding interface state $\bar{u}, \bar{p}$. Using the first equation of (4.6) and (4.11) in the second equation of (4.6) to eliminate u_o and $\bar{u}$ yields

$$\bar{p} = p_o \frac{K + 1}{2} \frac{n + 1}{n} \tag{4.14}$$

For a given laminate, (4.14) gives the relation between the pressure p_o at the loading surface at t_o and the pressure $\bar{p}$ at the interface at $t_o + 0.5\tau$ in terms of the slope factor n.

Figure 4.2a shows the x,t diagram for a two-layered (thick base) laminate for which separation does not occur. In the region 01a, only C^+ characteristics occur. Therefore, each characteristic in this region maps into a point on the same Γ^+ in the u,p plane. If $u = p = 0$ for $t < 0$ $(n = 1)$, this must be Γ_o^+ $(p = \rho cu)$ as indicated in Fig. 4.2b. The segment of Γ_o^+ involved is determined by the load applied during the interval $0 \le t < \tau$. For an exponential pulse, as shown in Fig. 4.2b, the segment extends from $p = P$ to $p = eP$. This gives the loading surface states for $0 \le t < \tau$.

To determine the interface states for $0.5\tau \le t \le 1.5\tau$, we use (4.14) with $n = 1$ and obtain

$$\bar{p}(t) = (K + 1)Pe(t - 0.5\tau) \tag{4.15}$$

These states lie on the line $p = \rho_b c_b u$ along the segment $\bar{12}$, as shown in Fig. 4.2b.

(a)

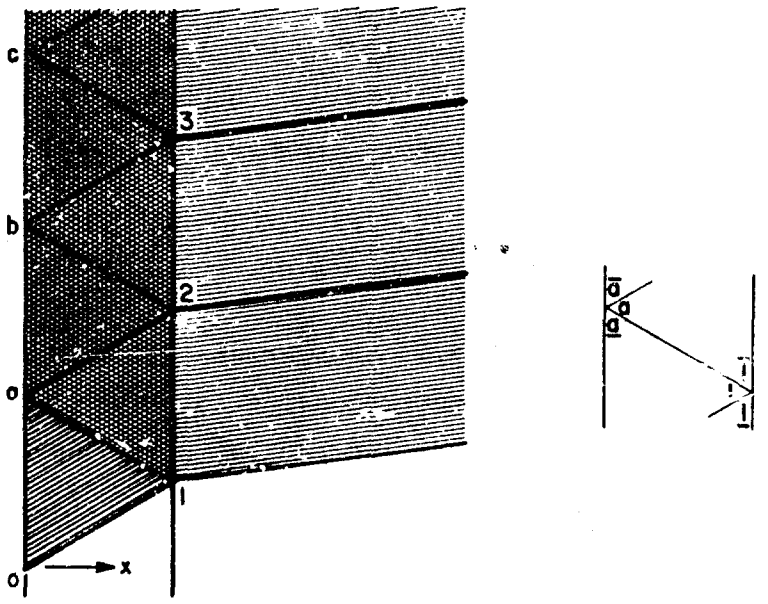

(b)

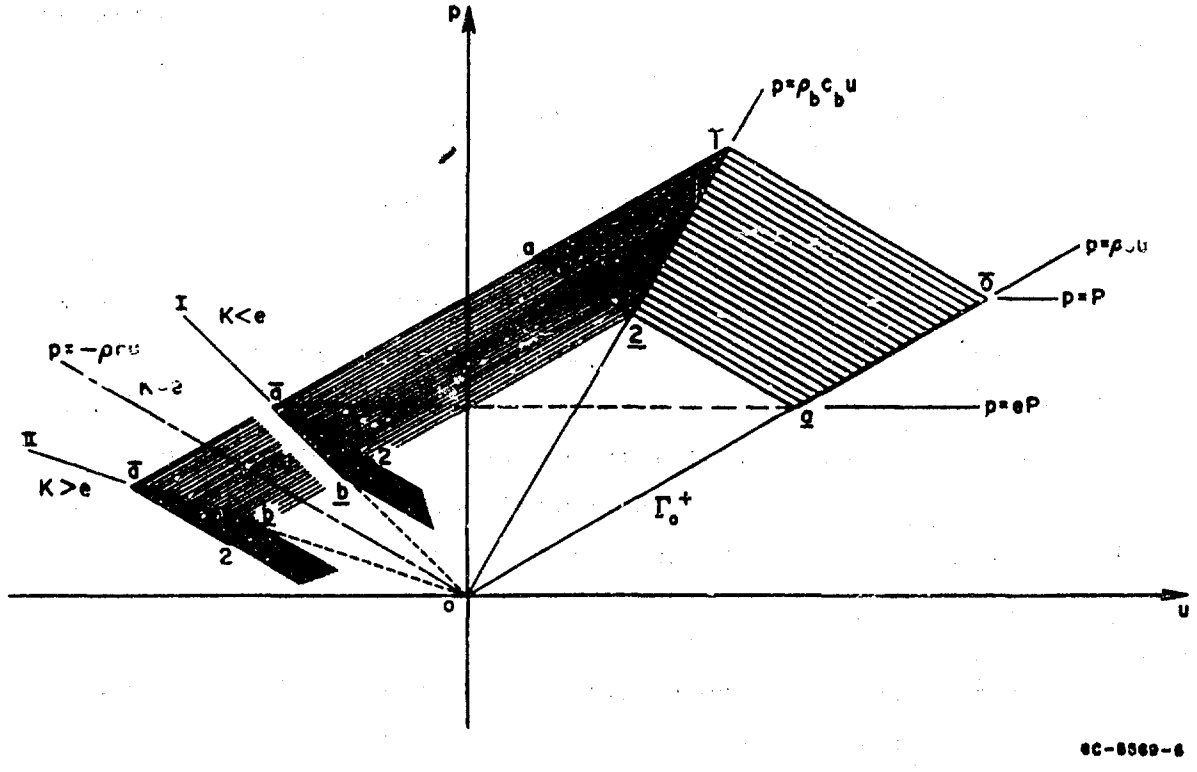

FIG. 4.2 x,t AND u,p DIAGRAMS FOR EXPONENTIAL PULSES

The loading surface states for $\tau \le t < 2\tau$ are found using (4.12) with $n = 1$ (since u_o, p_o lies on $p = \rho cu$). This gives

$$p = \rho cu \frac{e}{e - 2K} \tag{4.16}$$

Thus, these states lie on a straight line of slope $\rho c[e/(e - 2K)]$ passing through the origin.

The lines I and II of Fig. 4.2b show two possible locations of this line with respect to the line $p = -\rho cu$. To facilitate the discussion of these cases, we first obtain the equations for the loci of subsequent loading surface states.

To obtain the line of loading surface states for $2\tau \le t < 3\tau$, we put $n = e/(e - 2K) = x$ from (4.16) into (4.12) and obtain

$$p = \rho cu \frac{xe}{xe - (x + 1)K} \tag{4.17}$$

By continuing this process we obtain for the successive loading surface states

$$\begin{aligned}
&p = \rho cu && P \ge p > eP \\
&p = x\rho cu && eP \ge p > e^2P \\
&p = y_1\rho cu && e^2P \ge p > e^3P \\
&p = y_2\rho cu && e^3P \ge p > e^4P \\
&\text{etc.}
\end{aligned} \tag{4.18}$$

where

$$\begin{aligned}
x &= \frac{1}{1 - 2\xi} \\
y_1 &= \frac{x}{x - (1 + x)\xi} \\
y_2 &= \frac{y_1}{y_1 - (1 + y_1)\xi} \\
&\text{etc.}
\end{aligned} \tag{4.19}$$

and $\xi = K/e$.

As shown below, if separation occurs it takes place first at $t = 1.5\tau$. Then, using (4.13) instead of (4.12), we obtain for the sequence of loading surface states

$$\begin{aligned} p &= \rho c u && P \geq p > eP \\ p &= x\rho c u && eP \geq p > e^2P \\ p &= z_1\rho c u && e^2P \geq p > e^3P \\ p &= z_2\rho c u && e^3P \geq p > e^4P \\ &\text{etc.} \end{aligned} \tag{4.20}$$

where

$$\begin{aligned} x &= \frac{1}{1 - 2\xi} \\ z_1 &= \frac{xe}{xe + (1 + x)} \\ z_2 &= \frac{z_1 e}{z_1 e + (1 + z_1)} \\ &\text{etc.} \end{aligned} \tag{4.21}$$

4.4 Exponential Pulses with Slow Decay ($K \leq e$)

It is readily shown that for $K < e$ (corresponding to I in Fig. 4.2b) tensile stresses do not develop in the shield or base and hence cracking or spalling cannot occur. The u,p diagram for $K < e$, extending beyond that of Fig. 4.2b, is shown in Fig. 4.3; the x,t diagram is the same as that of Fig. 4.2a. Consecutive loci of u,p states at the loading surface are the line segments $\bar{oa}$, $\bar{ab}$, $\bar{bc}$, etc. These correspond to the states given by (4.18).

The sequence of lines $\bar{oa}$, $\bar{ob}$, $\bar{oc}$, etc. of Fig. 4.3 appears to approach a limit. The slope y_n of this line is easily found from

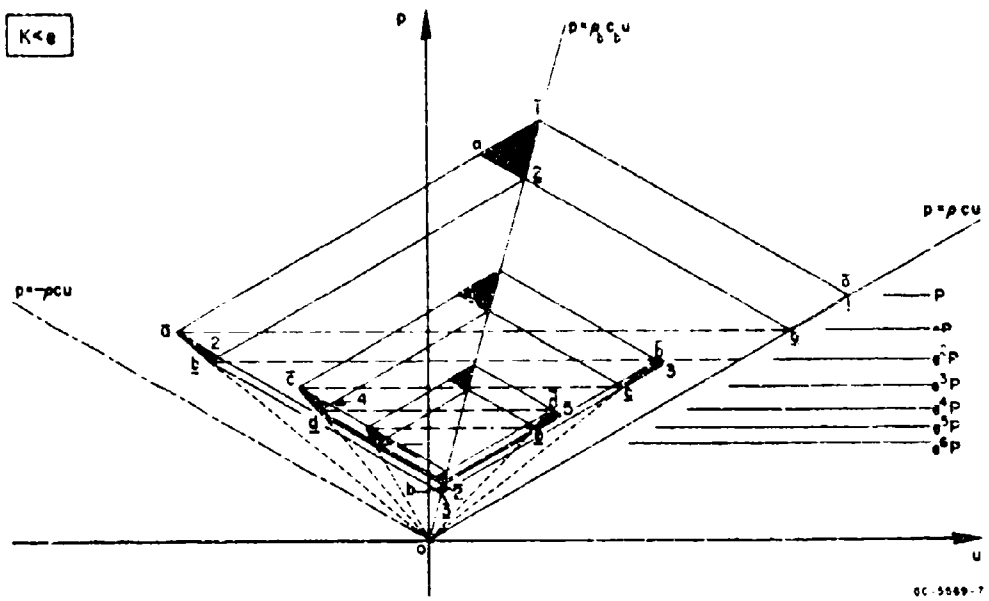

FIG. 4.3 u,p DIAGRAM FOR A PULSE WITH LOW RATE OF DECAY

(4.19) by putting $y_{n+1} = y_n$. This yields for the equation of the limiting line,

$$p = \frac{e + K}{e - K} \rho c u \qquad (4.22)$$

Hence, as can be seen from Fig. 4.3, for $K < e$ all the u,p states in the shield and the base lie within the region bounded by the lines $p = \rho c u$ and $p = -\rho c u$. Hence no tension develops in the shield or base.

4.5 Exponential Pulses with K = e

The x,t and u,p diagrams for the special case $K = e$ are given in Fig. 4.4. The triangles of state points $\bar{a}2\underline{b}$, $\bar{c}4\underline{d}$, etc., of Fig. 4.3 have all become segments of the line $p = -\rho c u$ and the triangles of state points $\bar{b}3\underline{c}$, $\bar{d}5\underline{e}$, etc., have become segments of the line $p = \rho c u$. All state points for the triangular areas $\bar{2}b\underline{3}$, ..., are represented by the origin $u = p = 0$. Since pressures are always positive, cracking or spalling does not occur. For $K = e$, the limiting line (4.22) approaches the p-axis.

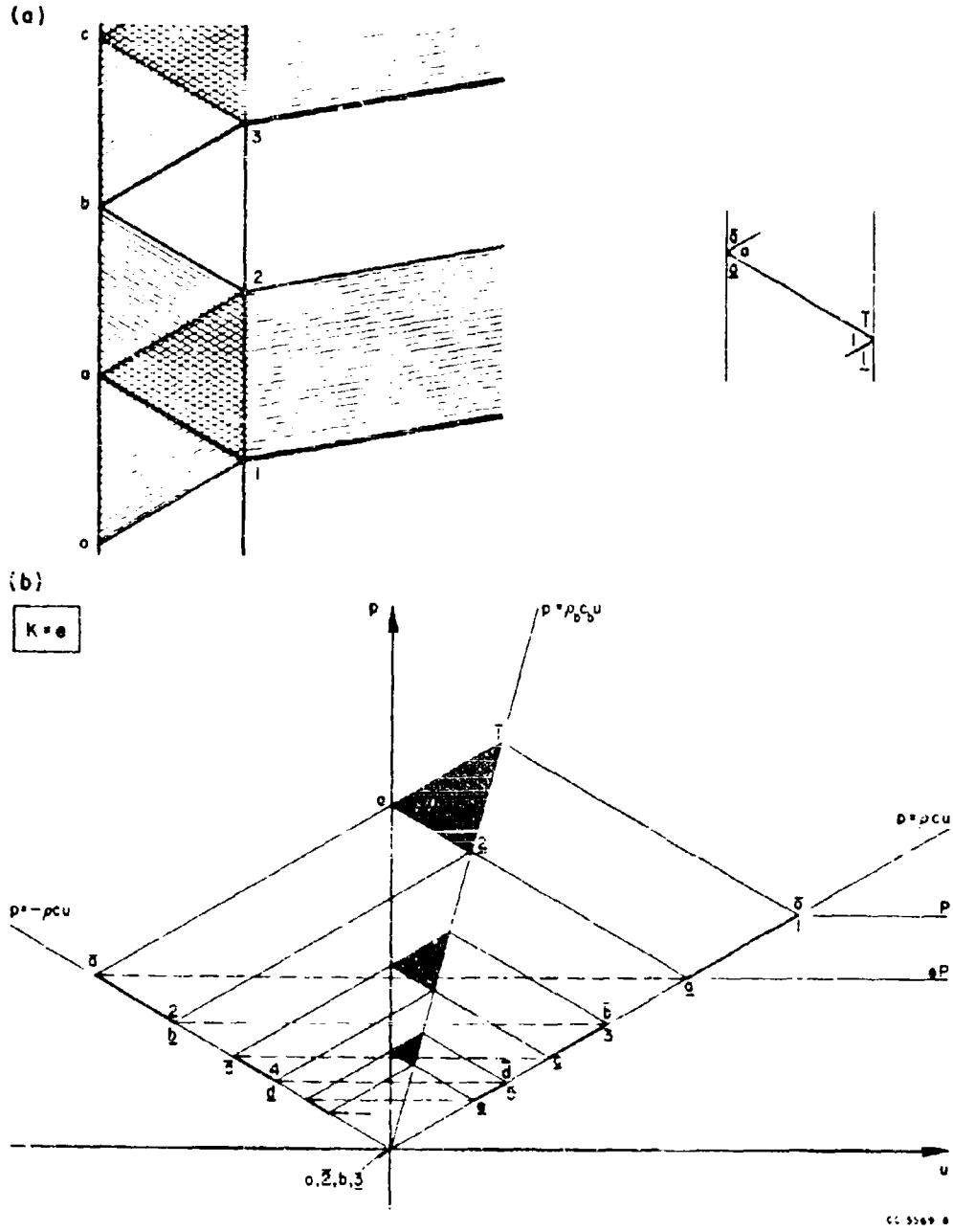

FIG. 4.4 x,t AND u,p DIAGRAMS FOR K = ∞

4.6 Exponential Pulses with $K > e$

As shown above, for $K < e$ no tensile stresses develop in the shield or base. For $K > e$, tensile stresses always occur, as can be readily shown from Fig. 4.2b.

In Fig. 4.2b, the locus of interface states for $1.5\tau \leq t < 2.5\tau$ in the segment of $p = \rho_b c_b u$ (line of interface states) which would be intersected by the extension of the lines emanating from II. Hence, the first possibility of tensile stress occurs at $t = 1.5\tau$. For a perfect bond, the magnitude of the tensile stress at $t = 1.5\tau$ is given by the intersection of the line through $\bar{a}2$ with the line of interface states. For the interval $1.5\tau \leq t < 2.5\tau$, the tensile stress with a perfect bond is a maximum for $t = 1.5\tau$.

For zero bond strength, tensile stresses at the interface cannot be sustained and separation occurs at $t = 1.5\tau$. Subsequent interface states lie on the segment of $p = 0$ intersected by the lines emanating from II.

For zero bond strength, the region $K > e$ divides into two parts for which the u,p diagrams are basically different. If point 2 of Fig. 4.2b lies above $p = 0$, as shown, one type of diagram results; if it lies below $p = 0$, a different type results. The division occurs for point 2 lying on $p = 0$. Pulses for which point 2 lies below $p = 0$ are pulses with fast decay; pulses for which point 2 lies above $p = 0$ are pulses with moderate decay.

The x,t and u,p diagrams for $p_2 = 0$ are shown in Fig. 4.5. As can be seen in the figure, state 2 is determined by the intersection of the lines

$$p_2 - p_{\underline{2}} = \rho c(u_2 - u_{\underline{2}})$$

$$p_2 - p_{\underline{a}} = -\rho c(u_2 - u_{\underline{a}})$$

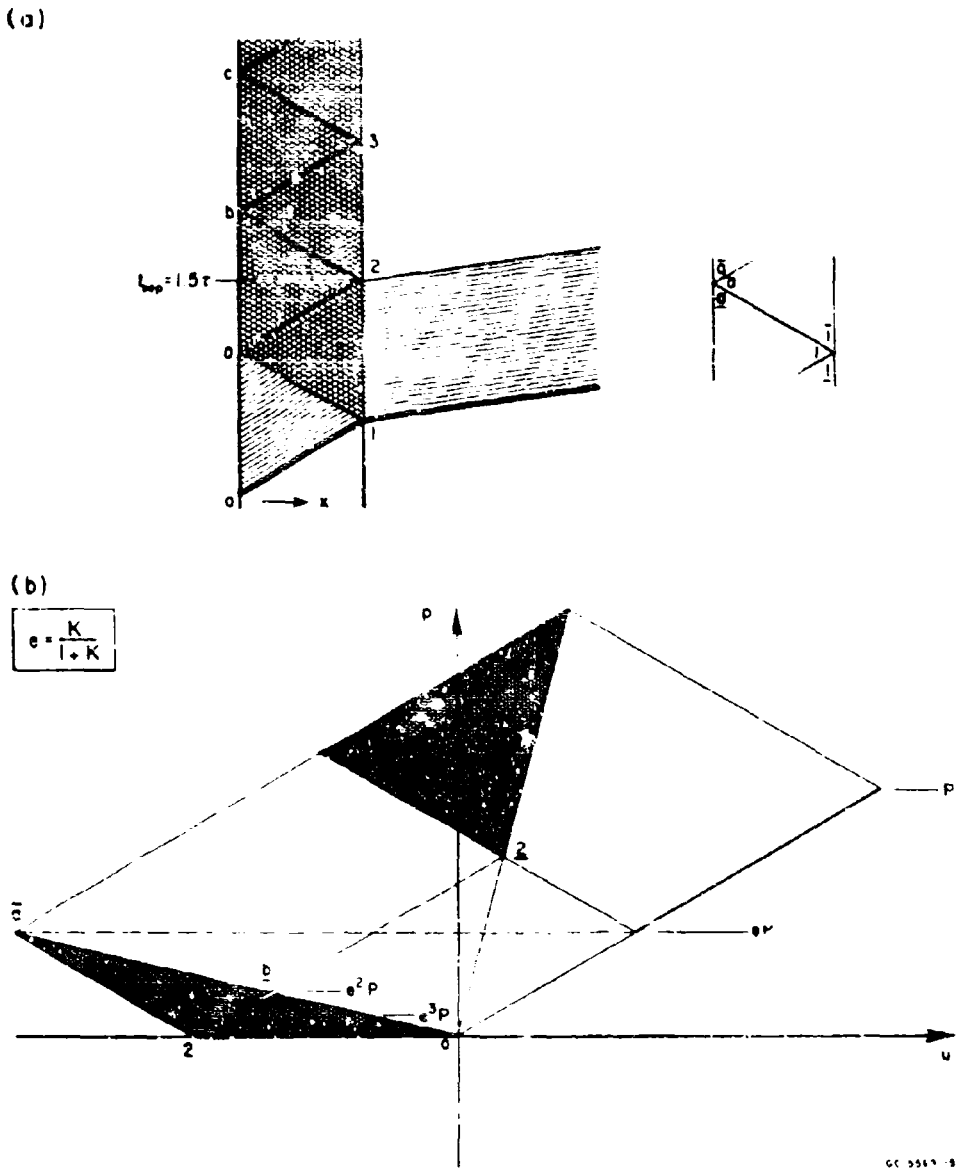

FIG. 4.5 x,t AND u,p DIAGRAMS FOR $p_2 = 0$ ($e = K/(K+1)$)

Using

$$p_{\underline{2}} = \rho_b c_b u_{\underline{2}} = (1 + K)eP$$

$$p_{\underline{a}} = x_{\underline{a}} c u_{\underline{a}} = eP$$

with x from (4.21), and $p_2 = 0$ we obtain the condition

$$e = \frac{K}{K + 1} \tag{4.23}$$

As indicated in Fig. 4.5b, the final loading surface state is $u = p = 0$. Hence the shield separates and is brought to rest by the pulse. As is shown below, for pulses with high decay rate the shield is left with a final velocity, and for pulses with moderate decay, the shield is driven back toward the base and recombination occurs. The regions in the K,e plane for slow, moderate, and fast decay are shown later in Fig. 4.15.

4.7 Exponential Pulses with Fast Decay ($0 < e < K/K + 1$)

Typical u,p diagrams for pulses with fast decay are shown in Fig. 4.6; the x,t diagram is the same as in Fig. 4.5a. Figure 4.6a gives the overall aspects of the diagram and Figs. 4.6b and c show details for relatively large and small values of e. It is readily seen from Figs. 4.6b and c that the sequence of triangular regions $\bar{a}2\underline{b}$, $\bar{b}3\underline{c}$, etc. reaches the limiting region $\bar{N}\underline{N}$, and the sequence $\bar{2}\underline{b}3$, $\bar{3}\underline{c}4$, etc. reaches $\bar{N}n\underline{N}$. These two limiting regions give the final state of motion and stress in the shield. As can be seen from the x,t diagram of Fig. 4.5a, after $t = 1.5\tau$ the motion is periodic with period τ. Since velocities are negative throughout, the shield remains separated.

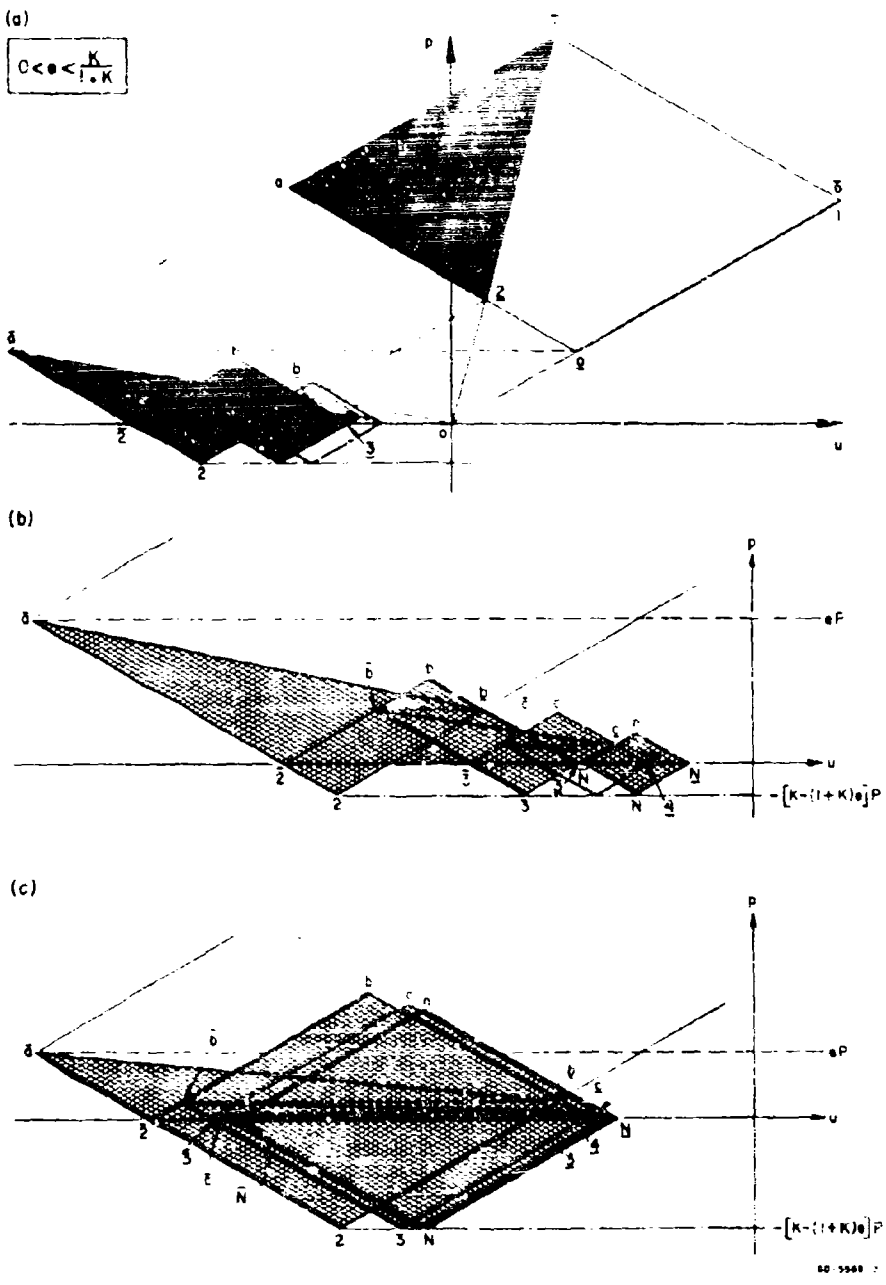

FIG. 4.6 u,p DIAGRAM FOR A PULSE WITH FAST DECAY
(a) complete diagram, (b) detail for large value of e, and (c) detail for small value of e

The maximum tensile stress ($\sigma_{max} = p_2$) indicated in Fig. 4.6 is found from the equations

$$
\begin{aligned}
p_2 - p_{\underline{2}} &= \rho c(u_2 - u_{\underline{2}}) \\
p_2 - p_{\underline{a}} &= \rho c(u_2 - u_{\underline{a}}) \\
p_{\underline{2}} &= \rho_b c_b u_{\underline{2}} = (1 + K)eP \\
p_{\underline{a}} &= \rho c u_{\underline{a}} = eP
\end{aligned}
\tag{4.24}
$$

and is given by

$$
- p_2 = \sigma_{max} = [K - (1 + K)e]P \tag{4.25}
$$

For the special case $(1 + K)e = K$ of Fig. 4.5, this reduces to $\sigma_{max} = 0$ as it should.

For the limiting case $e \to 0$ (very short pulse) we find $\sigma_{max} = KP$. The corresponding u,p diagram is shown in Fig. 4.7. The regions $\bar{a}2\underline{b}$, $\bar{b}3\underline{c}$, etc., all coincide with the region $\bar{N}N\underline{N}$, and $\bar{2}b\underline{3}$, $\bar{3}c\underline{4}$, etc. coincide with $\bar{N}n\underline{N}$. The diagram of Fig. 4.7 applies to short pulses of arbitrary shape, i.e. all pulses with step rise, a continuous decay, and a total duration T such that $T \leq \tau$.

4.8 Exponential Pulses with Moderate Decay $[K/(K + 1) < e < K]$

The analysis of pulses with moderate decay is more complicated than that for pulses with slow or fast decay because recombination occurs. Figure 4.8 shows the u,p diagram for a pulse with e slightly less than K. The x,t diagram (until recombination occurs) is the same as that of Fig. 4.5a.

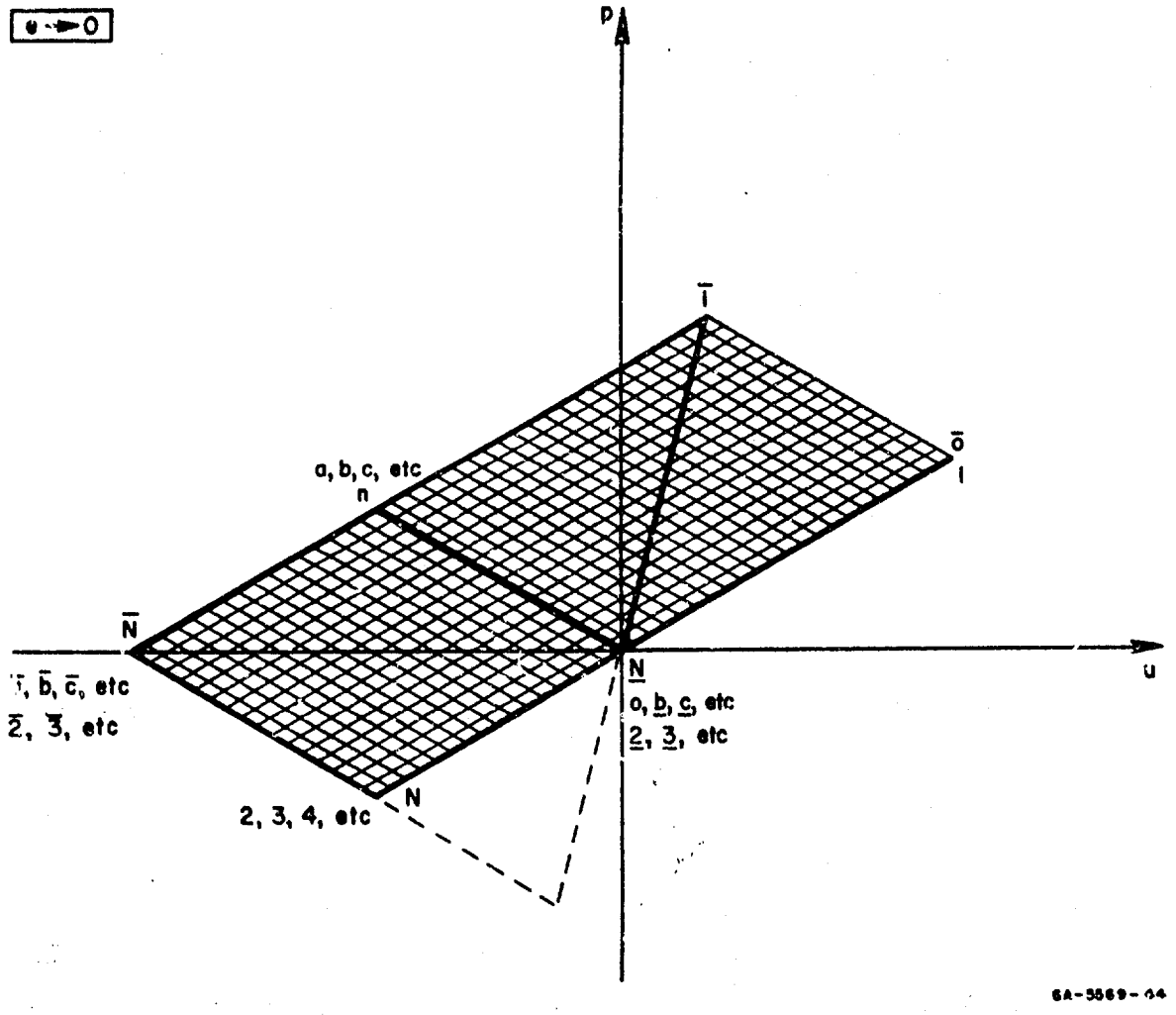

FIG. 4.7 u,p DIAGRAM FOR $e \to 0$

The regions of states $\bar{o}1\underline{a}$, $\bar{1}a\underline{2}$, and $\bar{a}2\underline{b}$ are found as before. Since $e < K$, separation of shield and base occurs at $t = 1.5\tau$. Hence, the region of states $\bar{2}b\underline{3}$ is determined by the condition $p = 0$ at the interface. The following two regions $\bar{b}3\underline{c}$ and $\bar{3}c\underline{4}$ are also easily determined.

From the x,t diagram of Fig. 4.5a it is seen that the segment of the u-axis $\bar{2}\underline{3}$ in Fig. 4.8 gives the interface velocity for $1.5\tau \le t < 2.5\tau$, and the segment $\bar{3}\underline{4}$ gives the interface velocity for $2.5\tau \le t < 3.5\tau$. Since the velocities corresponding to the segment $\bar{2}\underline{3}$ are smaller than those corresponding to the segment $\bar{3}\underline{4}$, the outward displacement of the shield during $1.5\tau \le t \le 2.5\tau$ is less than the possible inward displacement during $2.5\tau \le t \le 3.5\tau$. Hence recombination of the base occurs at an instant $t = \varphi\tau$, where $2.5 < \varphi < 3.5$.

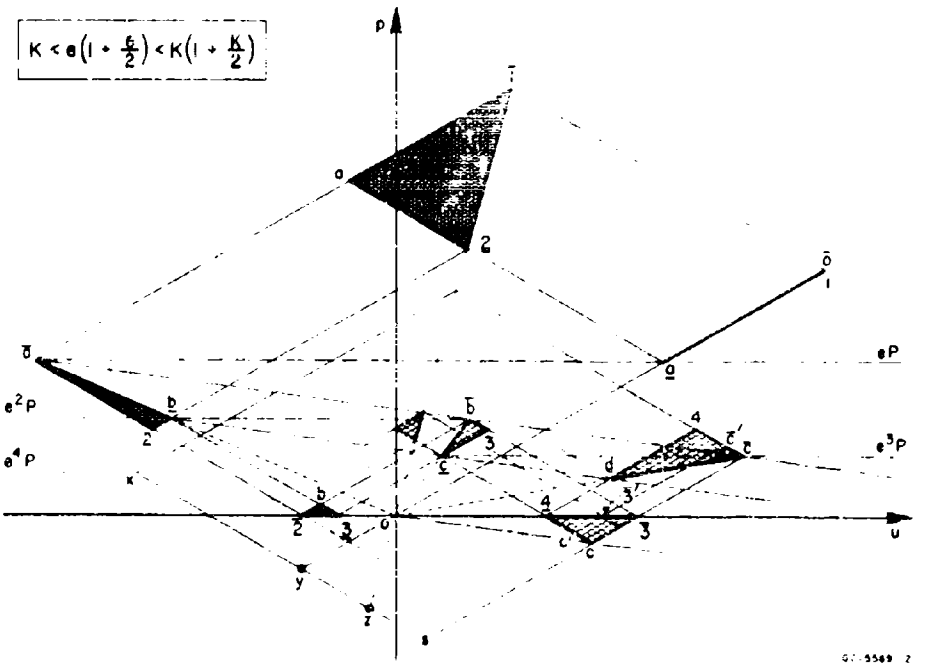

FIG. 4.8 u,p DIAGRAM FOR A PULSE WITH MODERATE DECAY K < e < ē, e(2 + e) < 2K. Recombination at t < 3.5τ

After the instant $t = \tau$, state points for elements of the shield at the interface are no longer determined by the condition $p = 0$: instead they must lie, as before separation, on the line $p = \rho_b c_b u$. Hence, the triangle of state points $\bar{3}c\underline{4}$ is not completely realized; only points within the region $\bar{3}\bar{3}'c'c$ actually occur. The remaining part $\bar{3}'\underline{c}'\underline{4}$ of the region $\bar{3}c\underline{4}$ is transferred to the interface line $p = \rho_b c_b u$ as indicated in Fig. 4.8.

A more detailed version of the diagram of Fig. 4.8 including later states is shown in Fig. 4.9. Inspection of the interface states indicates that separation and recombination occur repeatedly.

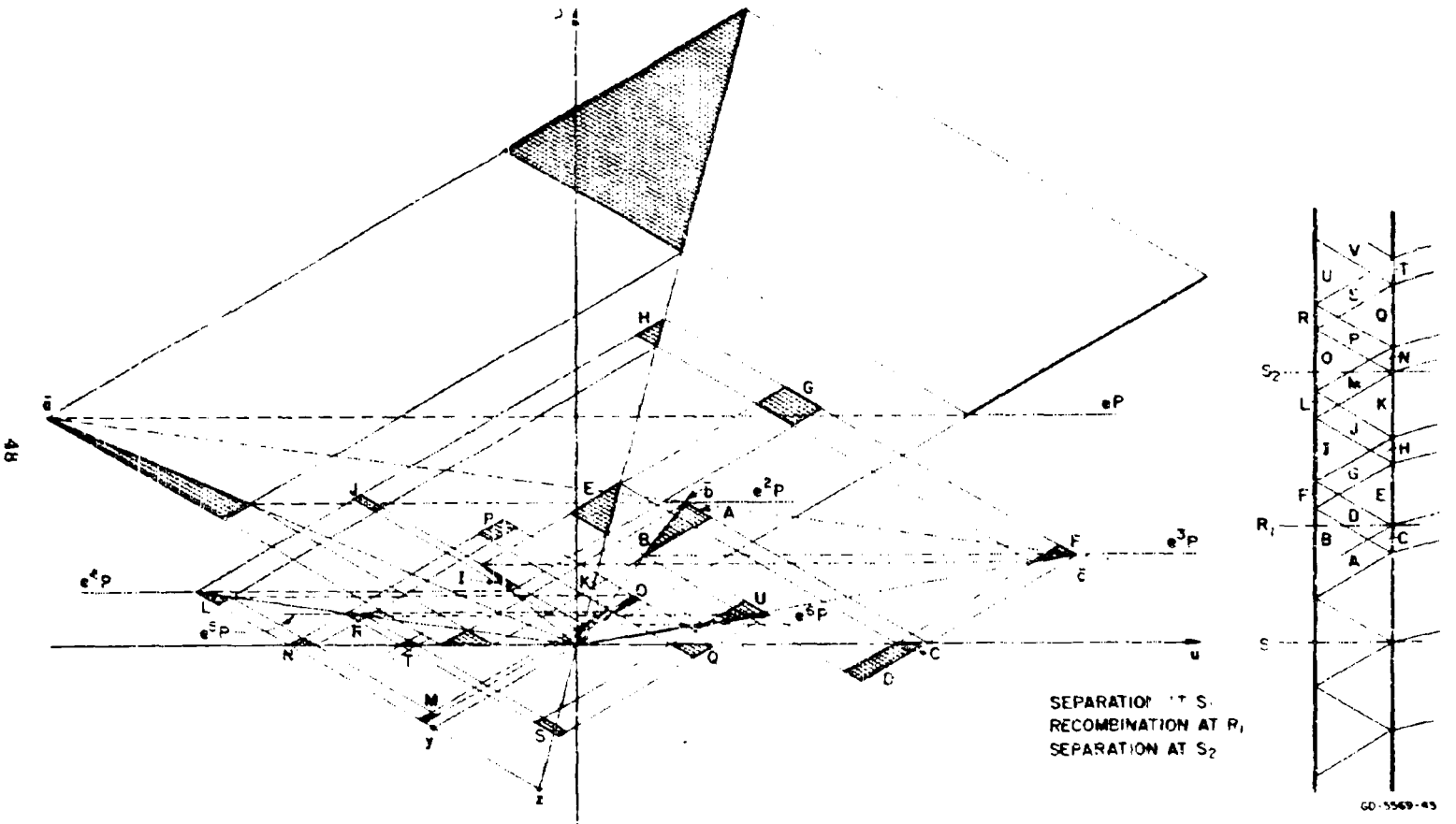

FIG. 4.9 u,p DIAGRAM FOR A PULSE WITH MODERATE DECAY K = e > $\bar{e}$, $\bar{e}(2-\bar{e})$ 2K.
Recombination at t = 3.5..

Figures 4.8 and 4.9 are valid for initial recombination during the interval $2.5\tau < t < 3.5\tau$. Figure 4.10 gives the u,p diagram for recombination at $t = 3.5\tau$. This occurs when the line of states $\bar{b}\underline{c}$ coincides with the p-axis, since then the velocities corresponding to the line segments $\bar{2}\underline{3}$ and $\bar{3}\underline{4}$ on the u-axis are equal and opposite. For the line of states $\bar{b}\underline{c}$ to coincide with the p-axis, the slope factor z_1 of (4.20) must be infinite. This gives

$$2K = e(e + 2) \tag{4.26}$$

The parameters K and e of Fig. 4.10, in addition to satisfying the condition $z_1 \to \infty$, were chosen so that after recombination, i.e., subsequent to the region $\bar{c}4\underline{d}$, the u,p diagram is identical to that of Fig. 4.5b. This occurs wnen state 5 (corresponding to state 2 of Fig. 4.5b) is on the u-axis. This results in the condition

$$e^3 + \frac{3}{2}e^2 + \frac{e}{2} = 1 \tag{4.27}$$

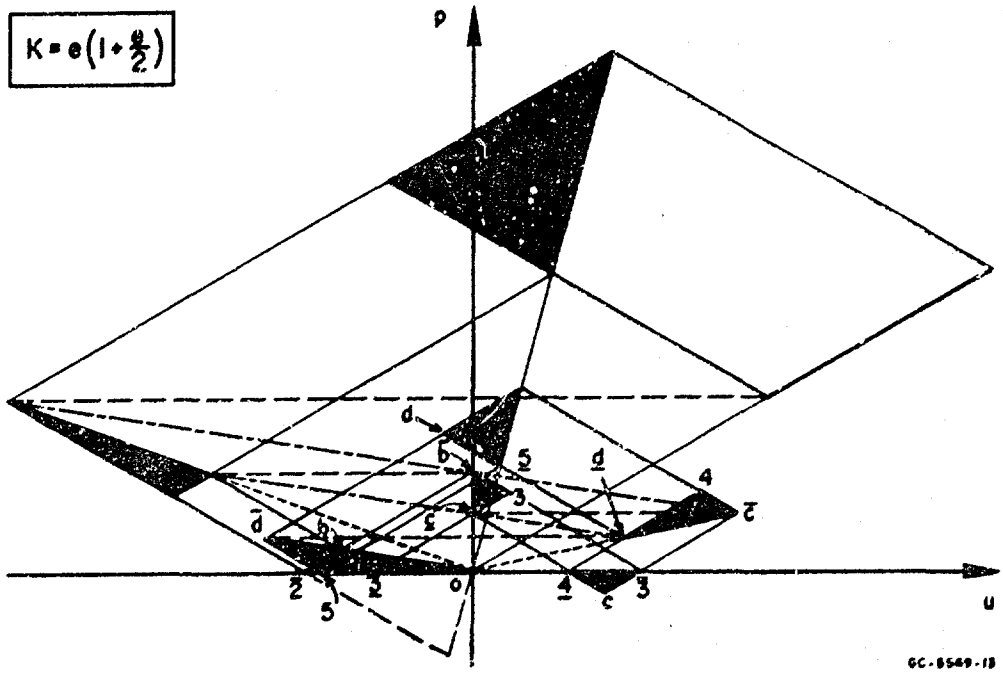

FIG. 4.10 u,p DIAGRAM FOR THE SPECIAL CASE $e[1 + (e/2)] = K$, $e^3 + (3/2)e^2 + e/2 = 1$ ($e = 0.6$, $K = 0.78$)

This equation has one real root in the interval $0 < e < 1$ which is approximately 0.6. The corresponding value of K from (4.26) is 0.78. Thus, for $e = 0.6$, $K = 0.78$, the diagrams of Fig. 4.5b and that of Fig. 4.10 become identical subsequent to region $\bar{c}4\underline{d}$. This means that the shield eventually comes to rest.

Figure 4.11 gives the u,p diagram for which initial recombination occurs during the interval $3.5\tau < t < 4.5\tau$. For this case recombination does not occur prior to $t = 3.5\tau$, because the average outward velocity corresponding to the segment $\bar{2}\underline{3}$ on the u-axis is greater than the average inward velocity corresponding to the segment $\bar{3}\underline{4}$. However, the average velocity of the two segments $\bar{3}\underline{4}$, $\bar{4}\underline{5}$ is greater than half the average velocity of $\bar{2}\underline{3}$, hence recombination occurs for $t < 4.5\tau$. The regions $\bar{4}\underline{d}5$ and $\bar{d}5\underline{e}$, respectively, in Fig. 4.11 correspond to the regions $\bar{3}c\underline{4}$ and $\bar{c}4\underline{d}$ of Fig. 4.8 and are not fully realized.

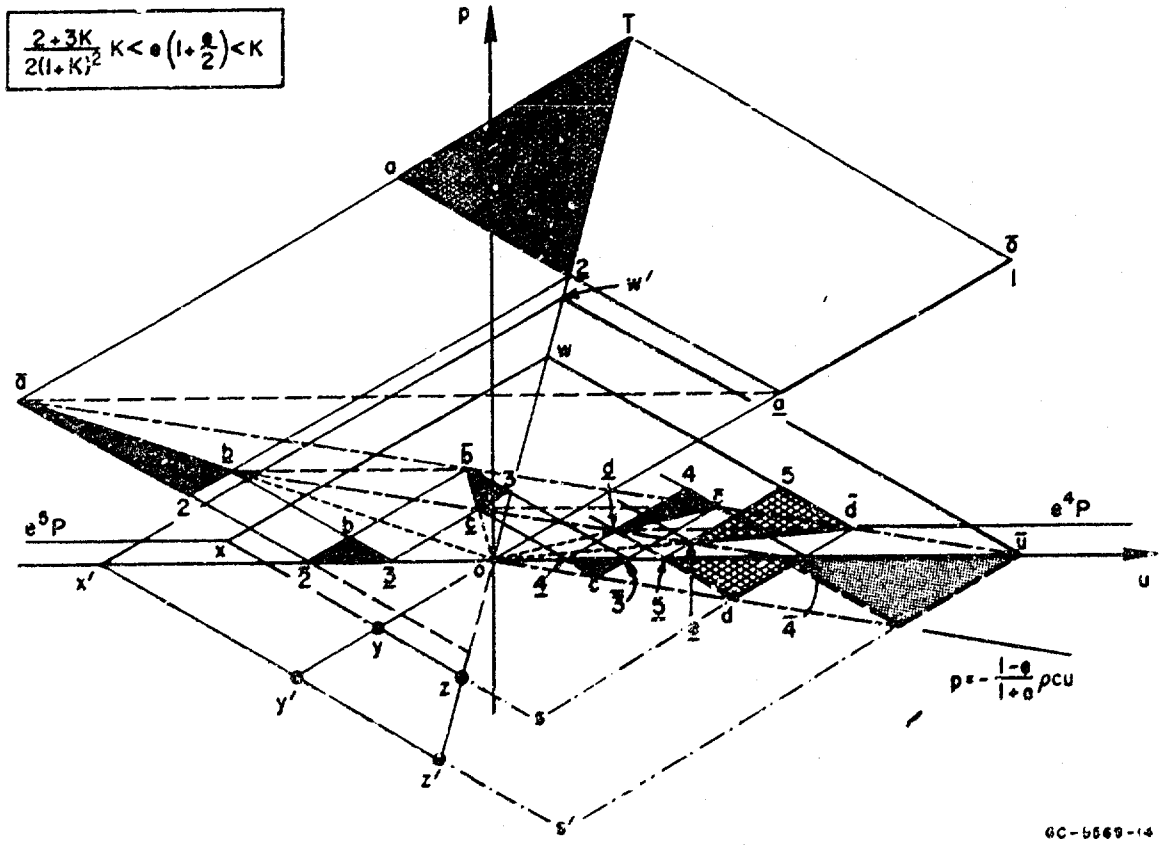

FIG. 4.11 u,p DIAGRAM FOR A PULSE WITH MODERATE DECAY.
Recombination at $t > 3.5\tau$.

In Fig. 4.9 the magnitude of the maximum tensile stress generated in the shield for the states shown lies between the stresses corresponding to the states y and z. Since the load decreases continually, subsequent tensile stresses should be less. Hence, the stresses at y and z are taken as bounds on the maximum tensile stress generated.

States y and z are determined by the intersection of the line xs in Fig. 4.8 with the lines $p = \rho c u$ and $p = \rho_b c_b u$. The equation of the line xs is

$$p - p_x = - \rho c (u - u_x)$$

with

$$p_x = e^4 p = m \rho c u_x$$

and m given by (4.12) for $n = z_2$ from (4.21). These equations yield

$$- p_y = \sigma_y = P[(e^3 + e^2 + e - K) K - e^4] \qquad (4.28)$$

and

$$- p_z = \sigma_z = (1 + K) \sigma_y \qquad (4.29)$$

The stresses given by (4.28) and (4.29) are valid for initial recombination occurring in the interval $2.5\tau \leq t < 3.5\tau$.

From Fig. 4.11, for initial recombination in the interval $3.5\tau \leq t < 4.5\tau$, the stresses at y and z are found from the equations

$$p - p_x = - \rho c (u - u_x)$$

with

$$p_x = e^5 P = m \rho c u_x$$

and m given by (4.12) for $n = z_3$ from (4.21). These yield

$$- p_y = \sigma_y = P[(e^4 + e^3 + e - K)K - e^5] \qquad (4.30)$$

and the expression of (4.29) for σ_z.

Equations (4.28) and (4.29) suggest the general form

$$\sigma_y = P[(e^n + e^{n-1} + e^{n-2} + \ldots + e^3 + e^2 + e - K)K - e^{n+1}] \qquad (4.31)$$

where

$$\tau = N + 1$$

for initial recombination occurring in the interval

$$(N + 0.5)\tau \leq t \leq (N + 1.5)\tau \qquad N = 2,3,4,\ldots$$

For large N, a simpler and more accurate estimate of the maximum tensile stress can be obtained as follows. The state points $\bar{a}$, $\bar{b}$, $\bar{c}$, etc. of Figs. 4.8 and 4.11 are connected by a straight line of slope $-(1 - e)/(1 + e)$, as are the points b, c, d, etc. For the first set of these points this can be readily verified by noting that they have the coordinates $(eP/x\rho c, eP)$, $(e^2P/z_1\rho c, e^2P)$, $(e^3P/z_2\rho c, e^3P)$, $(e^4P/z_3\rho c, e^4P)$, etc. in the u,p plane, with x, z_1, z_2, z_3, etc. as given by (4.21). Hence, the equation for the straight line $\bar{a}\bar{b}$ is

$$p = -\frac{1 - e}{1 + e}\rho cu + \frac{e - (1 - e)K}{1 + e}2P$$

and is satisfied by the coordinates of the points, $\bar{c}$, $\bar{d}$, etc. In Fig. 4.11, intersection of this line with the u-axis yields the point $(\bar{u},0)$, with

$$\rho c\bar{u} = \frac{e - (1 - e)K}{1 - e}2P = \frac{(1 + K)e - K}{1 - e}2P$$

For decreasing values of e the intersection point $(\bar{u},0)$ moves toward the origin, reaching the origin for $e = K/(1 + K)$. As $\bar{u}$ approaches the origin, more velocity increments represented by line segments of the set $\bar{34}$, $\bar{45}$, etc. are needed to nullify the outward velocity corresponding to the line segment $\bar{23}$, implying that recombination will be continuously delayed. Moreover, as $\bar{u}$ approaches the origin, the region $\bar{u}wxs$ (Fig.4.11) approaches the limiting region $\bar{u}w'x's'$. Hence, for $e \to K/(1 + K)$ the maximum stress generated in the shield is bracketed between the values $\sigma_{y'}$ and $\sigma_{z'}$.

For $\sigma_{z'}$ we have

$$\sigma_{z'} = (1 + K)\,\sigma_{y'}$$

The intersection of the line $x's'$ with $p = \rho c(u - \bar{u})$ through $\bar{u},0$ gives $p_{y'} = -\sigma_{y'}$. The line $x's'$ is found using

$$p = -\rho c(u - u_x)$$

$$p_{w'} = \rho c(u_{w'} - u_{x'}) = -\rho c(u_{w'} - \bar{u})$$

$$p_{w'} = \rho_b c_b u_{w'}$$

which yield

$$p = -\rho c u - \frac{(1 + K)e - K}{1 - e}\,2KP$$

The intersection of this line with $p = \rho c u$ gives

$$-p_{y'} = \sigma_{y'} = \frac{(1 + K)e - K}{1 - e}\,KP \qquad (4.32)$$

For $e = K/(K + 1)$, (4.33) gives $\sigma_{y'} = 0$. This is as expected from the u,p diagram for this case in Fig. 4.5.

Equations (4.31), (4.32), and (4.29) provide estimates of the maximum radial tensile stress for pulses of moderate decay. In Section 4.10 these equations are used to calculate the spall boundary.

4.9 Cracking Boundary for Exponential Pulses

To determine the cracking boundary, we regard the shield as a ring in uniform radial motion. Cracking occurs if the outward displacement is sufficient to develop tensile stresses exceeding the fracture stress of the shield. For pulses with slow decay ($K \leq e$), separation does not occur; hence, cracking is not possible. However, for pulses with moderate or fast decay ($K > e$), separation always occurs and cracking is possible if the load amplitude is sufficient.

To determine the maximum outward displacement, the average outward velocity of the shield at the separation preceding cracking is required. For pulses with fast decay, permanent separation occurs at $t = 1.5\tau$. For pulses with moderate decay, the average outward velocity of the shield is greatest at first separation, i.e., at $t = 1.5\tau$. This can be seen in the example of Fig. 4.9 by comparison of the average velocities at s_1 and s_2 (the velocities at s_1 fall within the leftmost triangle). Since separation velocity is proportional to the load amplitude, and the effective amplitude decreases for each successive separation, the average outward velocity will be greatest at first separation, i.e., at $t = 1.5\tau$. Therefore, the average velocity needed to determine the maximum outward displacement is that at $t = 1.5\tau$ for all pulses.

The average velocity at $t = 1.5\tau$ is readily found. The velocity of the shield at the interface at $t = 1.5\tau$ is that at state 2 in Fig. 4.8. The velocity at the loading surface at the same instant is on the line $\bar{ab}$ of Fig. 4.8 and is given by

$$p(1.5\tau) = Pe^{-1.5} = x\rho cu_2 \qquad (4.33)$$

with x from (4.19). Since for exponential pulses the transformation

$x,t \rightarrow u,p$ is linear, for points between the loading surface and the interface the velocity will lie on the straight line in the u,p plane connecting the loading surface state and the interface state. Thus, the average velocity of the shield is simply

$$v = \frac{1}{2}(u_2 + u_{2'}) \tag{4.34}$$

From Fig. 4.3 we have

$$\begin{aligned} p_{\underline{a}} - p_2 &= -\rho c(u_{\underline{a}} - u_2) \\ p_{\underline{2}} - p_2 &= \rho c(u_{\underline{2}} - u_2) \\ p_2 &= (1 + K)p_{\underline{2}} = \rho_b c_b u_{\underline{2}} \\ p_{\underline{a}} &= p_{\underline{a}} = eP \\ p_{\underline{a}} &= x\rho c u_{\underline{a}} \end{aligned} \tag{4.35}$$

Together with x from (4.19) these equations yield

$$\rho c u_2 = [(1 - K)e - K]P \tag{4.36}$$

Combining (4.36) with (4.33) gives

$$v = -\frac{1}{2}\frac{P}{\rho c}[K - (1 - K)e + (2K - e)e^{1/2}] \tag{4.37}$$

The outward displacement of the shield is determined by the average outward velocity at separation and the subsequent load. Here we neglect the subsequent load and thus obtain a lower bound on the load required for cracking.* The kinetic energy (per unit area) of the shield at

*To account for the subsequent load is not difficult, but it was not accomplished in time for inclusion in this report.

separation is

$$\text{Kinetic energy} = \frac{1}{2}\rho h v^2$$

where h is the shield thickness. For a ring in uniform radial motion, the strain energy is

$$\text{Strain energy} = \frac{1}{2}\frac{h}{E_\theta}\sigma_\theta^2$$

where σ_θ is the hoop stress and E_θ is the corresponding elastic modulus. Equating the kinetic energy to the strain energy gives

$$v^2 = \frac{\sigma_\theta^2}{\rho E_\theta} = \frac{\sigma_\theta^2}{\rho^2 c_\theta^2} \tag{4.38}$$

where c_θ is sound speed. For a homogeneous isotropic material the ratio of the radial (dilatational) sound speed c to the circumferential (plate) sound speed c_θ is

$$\beta = \frac{c}{c_\theta} = \frac{1 - \nu}{\sqrt{1 - 2\nu}} \tag{4.39}$$

Introducing (4.39) into (4.38) yields

$$v = \frac{\beta}{\rho c}\sigma_\theta \tag{4.40}$$

Using (4.40) in (4.37), and putting $\sigma_\theta = \sigma_{cr}$, gives*

$$\frac{p_{cr}}{\sigma_{cr}} = 2\beta[K - (1 - K)e + (2K - e)e^{1/2}]^{-1} \tag{4.41}$$

Comparing (4.41) with (3.1a), we have

$$C = \frac{1}{2\beta}[K - (1 - K)e + (2K - e)e^{1/2}] \tag{4.42}$$

*v of (4.40) is equal to $-v$ of (4.37).

The cracking boundary (4.41) is shown in Fig. 4.12 for $K = 0.7$ and $\beta = 1.3(\nu = 0.4)$.

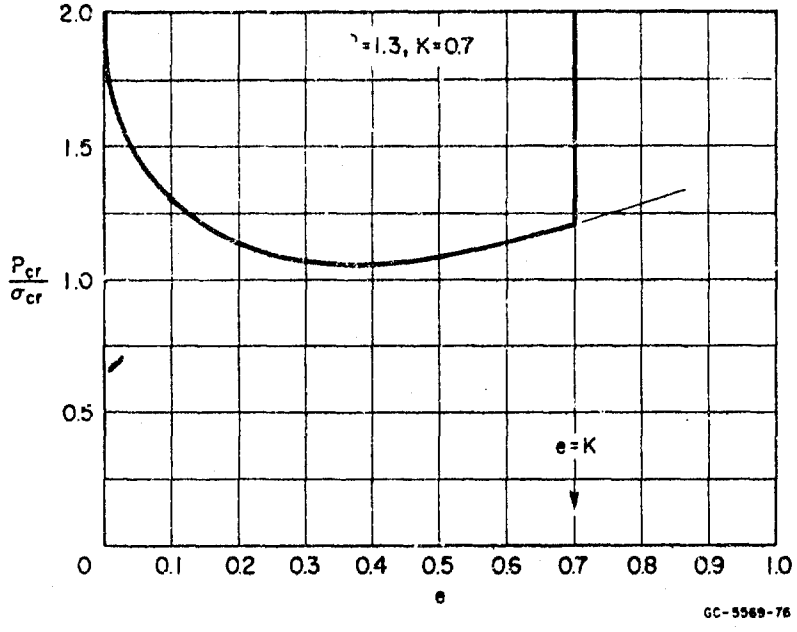

FIG. 4.12 CRACKING BOUNDARY FOR EXPONENTIAL PULSES IN TERMS OF e

For an exponential pulse the impulse I is given by

$$I = \frac{P}{\lambda} = PT \tag{4.43}$$

where T is the characteristic time duration (see Fig. 2.3). Using $\ell n\ e = -\lambda\tau$, we have

$$\frac{T}{\tau/2} = \frac{2}{\ell n(1/e)} \tag{4.44}$$

The cracking boundary in terms of $T/(\tau/2)$ is given in Fig. 4.13.

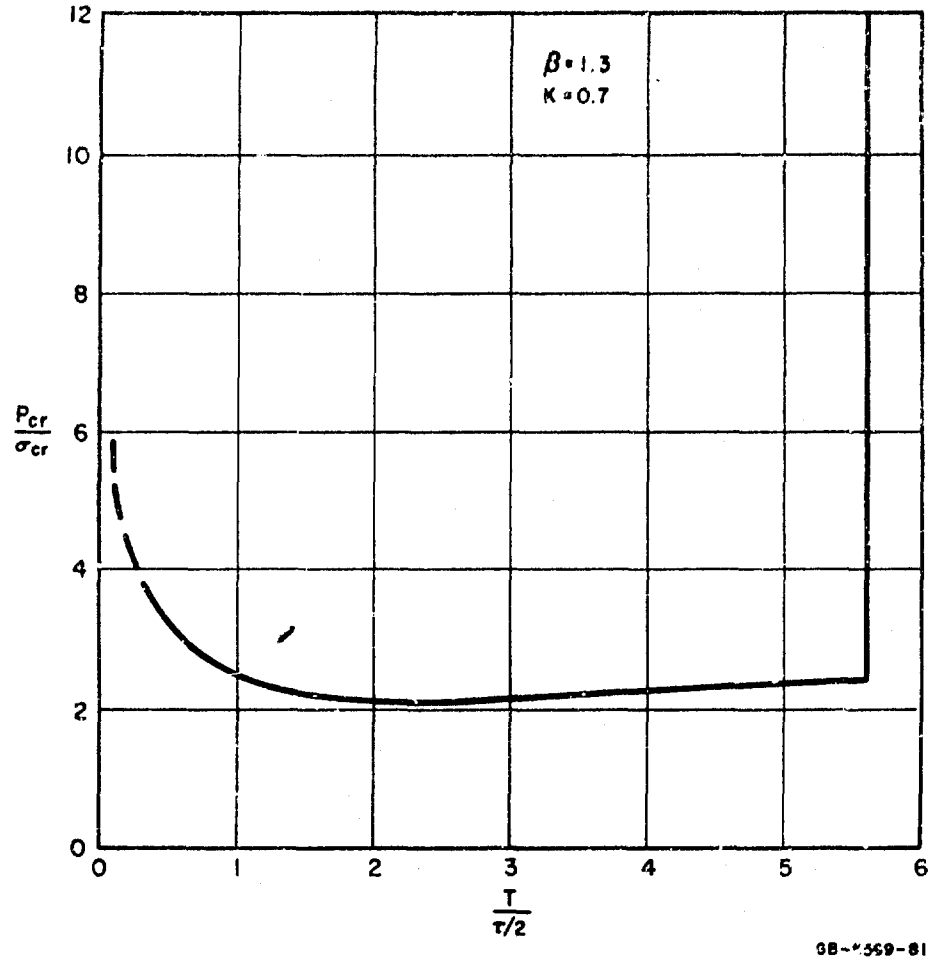

FIG. 4.13 CRACKING BOUNDARY FOR EXPONENTIAL PULSES IN TERMS OF T

To obtain the cracking boundary in the P,I plane we use the transformation

$$I_{cr} = P_{cr}T = \frac{P_{cr}\tau}{\ell n(1/e)} \qquad (4.45)$$

obtained from (4.43) and (4.44). The limiting value of I_{cr} for $e \to 0$ (very short pulses) is readily found. For pulses of arbitrary shape with durations less than τ, the momentum at separation is the reflected impulse I_r given by

$$I_r = -KI_{cr} = \rho hv$$

Dropping the minus sign and putting $h = c\,\frac{\tau}{2}$ gives

$$I_{cr} = \frac{1}{K}\,\rho c v\,\frac{\tau}{2}$$

Substituting v from (4.38) yields

$$I_{cr} = \frac{1}{K}\,\frac{c}{c_\theta}\,\sigma_{cr}\,\frac{\tau}{2}$$

With $\beta = c/c_\theta$ and $I^* = \beta/K$ we obtain

$$I_{cr} = \frac{\beta}{K}\,\sigma_{cr}\,\frac{\tau}{2} = I_{cr}^*\,\sigma_{cr}\,\frac{\tau}{2} \tag{4.46}$$

for the limiting impulse of the cracking boundary as $e \to 0$.

Using (4.45) and (4.46) yields the cracking boundary in the P,I plane shown in Fig. 4.14, where

$$I^* = \frac{I}{\sigma_{cr}\,\frac{\tau}{2}} \tag{4.47}$$

The boundary has the expected shape. In Fig. 3.1, the cracking boundary of Fig. 4.14 is compared to the cracking boundary obtained numerically.

4.10 Spall Boundary for Exponential Pulses

Figure 4.15 shows the regions of the K,e plane for exponential pulses with slow, moderate, and fast decay. For pulses with slow decay ($K \le e$) radial tensile stresses do not occur; hence spall is not possible. For pulses with moderate or fast decay ($K > e$) radial tensile stresses always occur and spall is possible if the load amplitude is sufficient. To facilitate the discussion, we regard K as fixed, say $K = 0.7$. Then, to establish the spall boundary, P_{sp}/σ_{sp} must be determined along the line $K = 0.7$ in Fig. 4.15.

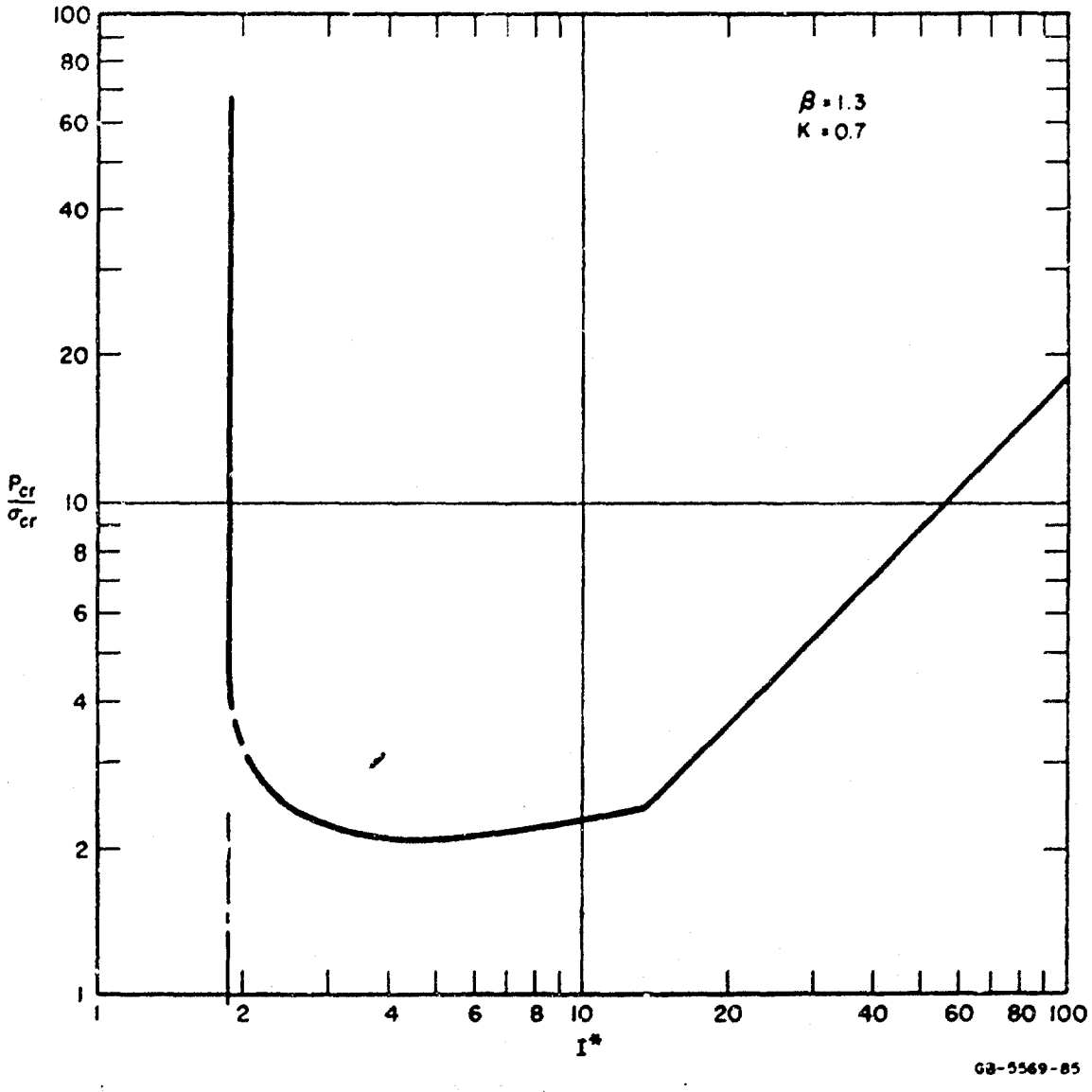

FIG. 4.14 CRACKING BOUNDARY FOR EXPONENTIAL PULSES IN PRESSURE-IMPULSE PLANE

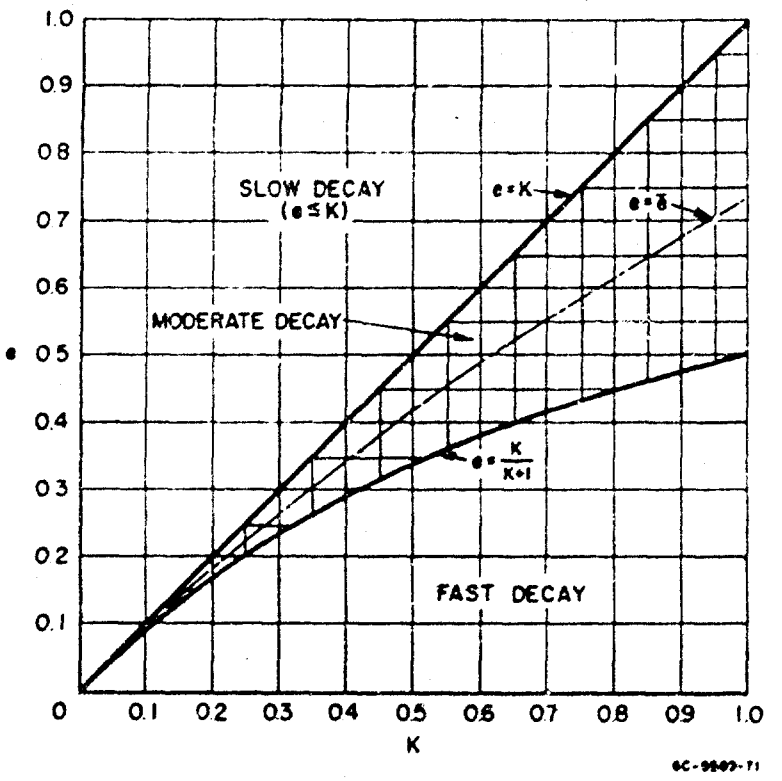

FIG. 4.15 SLOW, MODERATE, AND FAST DECAY REGIONS IN K,e PLANE

The segment of the line $K = 0.7$ extending upward from $e = K$ corresponds to pulses of slow decay, for which spall does not occur. Using the transformation of (4.44) with $e = K$ gives the vertical boundary of Fig. 4.16. Since larger values of e correspond to larger values of T, spall cannot occur in the region to the right of the vertical boundary.

The segment of the line $K = 0.7$ extending downward from $e = K(K + 1)$ in Fig. 4.15 corresponds to pulses with fast decay. For this segment we have from (4.25), with $\sigma_{max} = \sigma_{sp}$, $P = P_{sp}$,

$$\frac{P_{sp}}{\sigma_{sp}} = [K - (K + 1)e]^{-1} \tag{4.48}$$

Hence, from (3.1b),

$$S = K - (K + 1)e \tag{4.49}$$

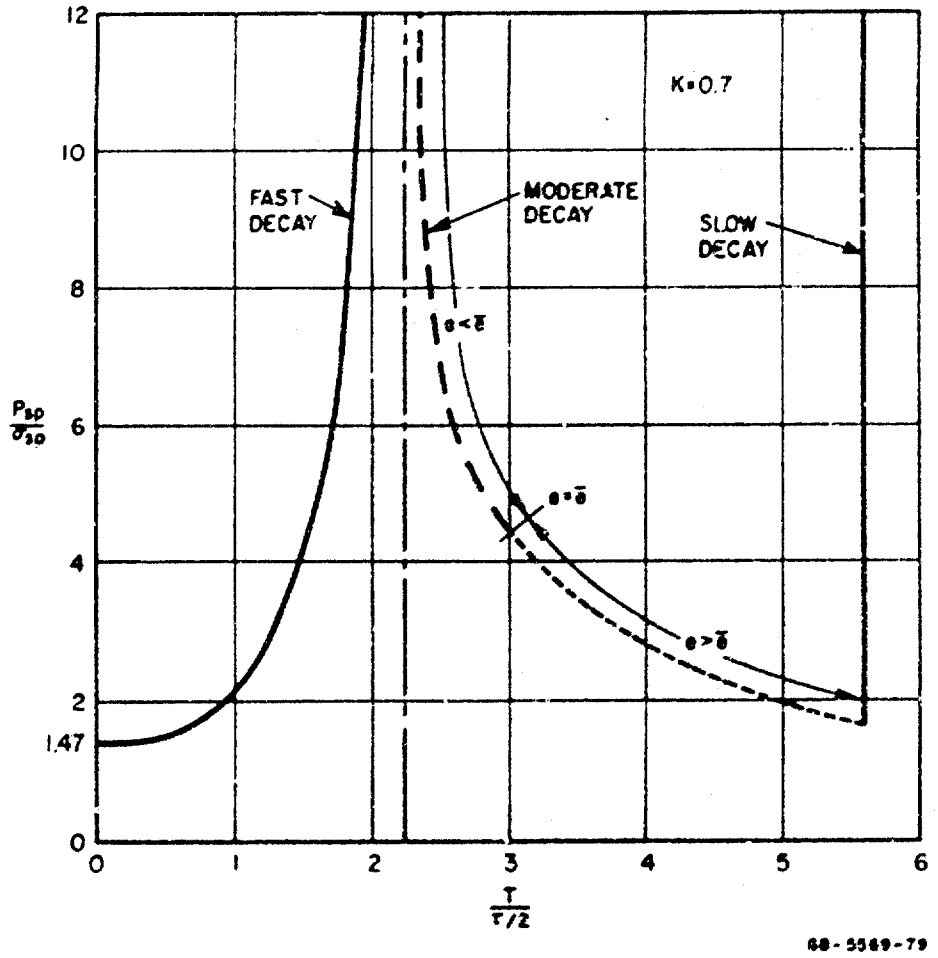

FIG. 4.16 SPALLING BOUNDARY FOR EXPONENTIAL PULSES IN TERMS OF T

Equation (4.49) together with the transformation of (4.44) yields the fast-decay boundary of Fig. 4.16. For the limiting value $e \to K/(K+1)$, (4.49) yields $P_{sp} \to \infty$, corresponding to the vertical asymptote in Fig. 4.16. For $e \to 0$, (4.49) gives $P_{sp}/\sigma_{sp} = 1/K = 1.47$, corresponding to the intersection of the spall boundary with the vertical axis in Fig. 4.16.

The segment of the line $K = 0.7$ between $e = K$ and $e = K/(K+1)$ corresponds to pulses of moderate decay. For the part of this segment $K > e > \bar{e}$, with $\bar{e}(\bar{e}+2) = 2K$ from (4.26), the spall boundary is

found using (4.29) and (4.31) with $\sigma_z = \sigma_{sp}$, $P = P_{sp}$, and $N = 2$, corresponding to recombination in the interval $1.5\tau \leq t < 2.5\tau$. Making these substitutions, we have

$$\frac{P_{sp}}{\sigma_{sp}} = \frac{1}{K+1}\left[(e^3 + e^2 + e - K)K - e^4\right]^{-1} \qquad (4.50)$$

Together with the transformation (4.44), (4.50) gives the spall boundary for $K > e > \bar{e}$.

To determine the intersection of the moderate-decay boundary with the slow-decay boundary in Fig. 4.16, we put $e = K(1 - \delta)$, $\delta << 1$, into (4.50) and obtain

$$\lim_{\delta \to 0} \frac{P_{sp}}{\sigma_{sp}} = \frac{1}{(K+1)K^3} \qquad (4.51)$$

For $K = 0.7$ this gives $P_{sp}/\sigma_{sp} = 1.71$ at the intersection of the moderate-decay and slow-decay boundaries.

To determine P_{sp}/σ_{sp} from (4.50) at $e = \bar{e}$, we put $e = \bar{e}(1 + \epsilon)$, $\epsilon << 1$, and obtain

$$\lim_{\epsilon \to 0} \frac{P_{sp}}{\sigma_{sp}} = \frac{1}{K+1}\left[\frac{\bar{e}^3}{2}\left(1 + \frac{\bar{e}}{2} + \bar{e}^2\right)\right]^{-1} \qquad (4.52)$$

For $K = 0.7$, $\bar{e} = 0.55$, and (4.52) yields $P_{sp}/\sigma_{sp} = 4.5$. Thus, as can be seen from Fig. 4.16 the spall boundary for $K > e > \bar{e}$, i.e., $N = 1$, extends from the slow-decay boundary to $T/(\tau/2) = 3$.

For the next interval, $N = 3$, (4.29) and (4.31) yield, with $\sigma_z = \sigma_{sp}$ and $P = P_{sp}$,

$$\frac{P_{sp}}{\sigma_{sp}} = \frac{1}{K+1}\left[(e^4 + e^3 + e^2 + e - K)K - e^5\right]^{-1} \qquad (4.53)$$

For $e \to \bar{e}$, (4.53) gives

$$\lim_{e \to \bar{e}} \frac{P_{sp}}{\sigma_{sp}} = \frac{1}{K+1}\left[\frac{\bar{e}^{-3}}{2}\left(1 + \frac{5}{2}\bar{e} + \bar{e}^{-2} + \bar{e}^{-3}\right]^{-1}\right. \tag{4.54}$$

For subsequent intervals, we use (4.29) and (4.32), with $\sigma_z = \sigma_{sp}$ and $P = P_{sp}$, to determine the spall boundary. This gives

$$\frac{P_{sp}}{\sigma_{sp}} = \frac{1}{K+1}\,\frac{(K+1)e - K}{1 - e}\,KP \tag{4.55}$$

The spall boundary in the P,I plane is obtained from Fig. 4.16 using the transformation (4.45) written as

$$I_{sp} = P_{sp}\,\frac{\tau}{2} = \frac{P_{sp}\tau}{\ell n(1/e)} \tag{4.56}$$

together with the definition

$$I^* = \frac{I}{\sigma_{cr}\,\frac{\tau}{2}} \tag{4.57}$$

The spall boundary in the P,I plane is shown in Fig. 4.17. The spall boundary of Fig. 4.17 is compared with numerical calculations in Fig. 3.2.

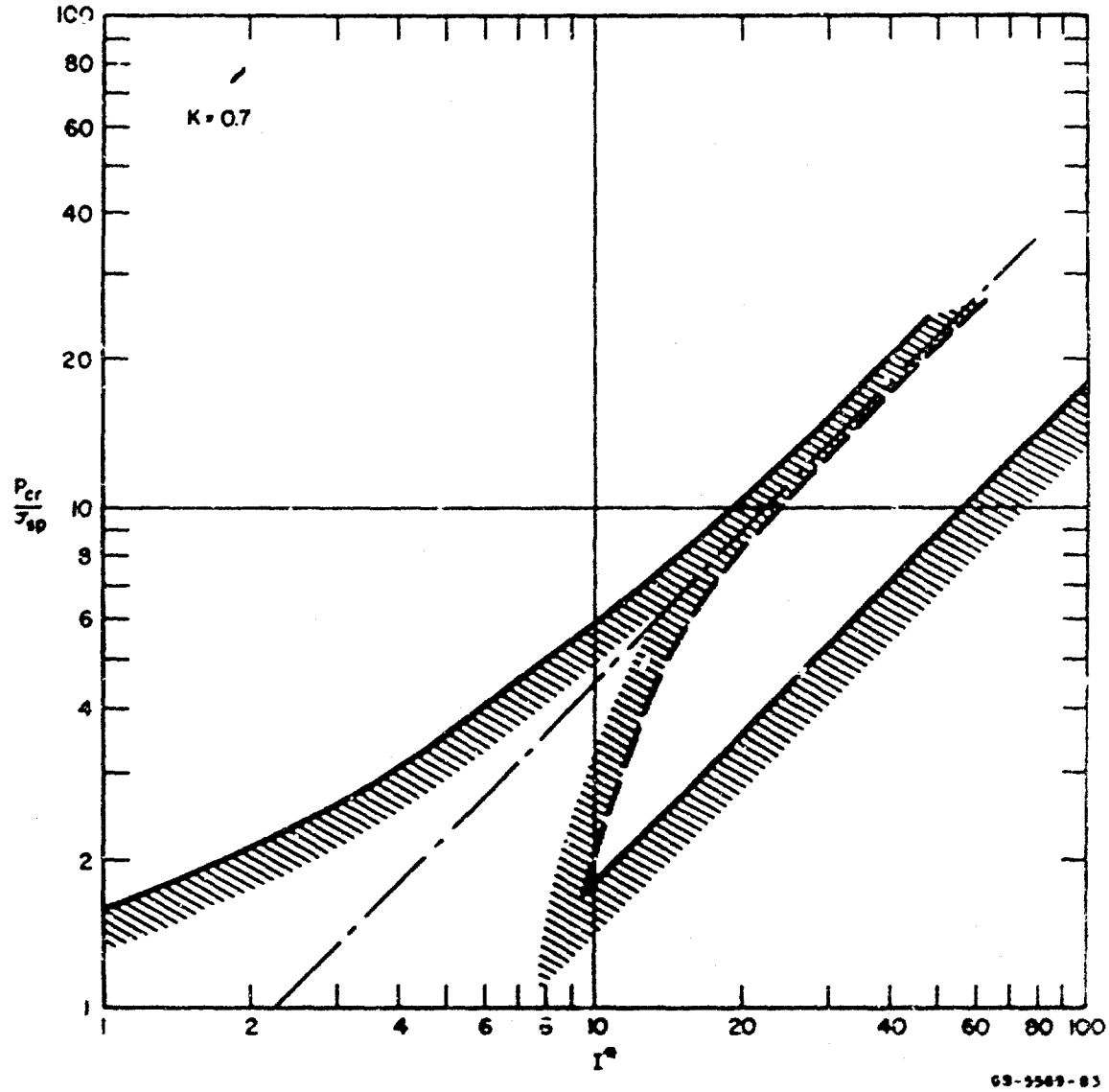

FIG. 4.17 SPALL BOUNDARY FOR EXPONENTIAL PULSES IN PRESSURE-IMPULSE PLANE

This page intentionally left blank.

SECTION 5

EXPERIMENTAL VERIFICATION OF REBOUND CRACKING THEORY

5.1 Introduction

To attempt to verify the theory of rebound cracking, an experimental program was undertaken using a shield of phenolic setting resin* and a thick base of steel. The main element of the experiment is shown in Fig. 5.1. On the central steel mandrel are mounted a phenolic test section, two segmented aluminum rings, a segmented phenolic ring, and two end spacers. The segments are shown more clearly in Fig. 5.2.

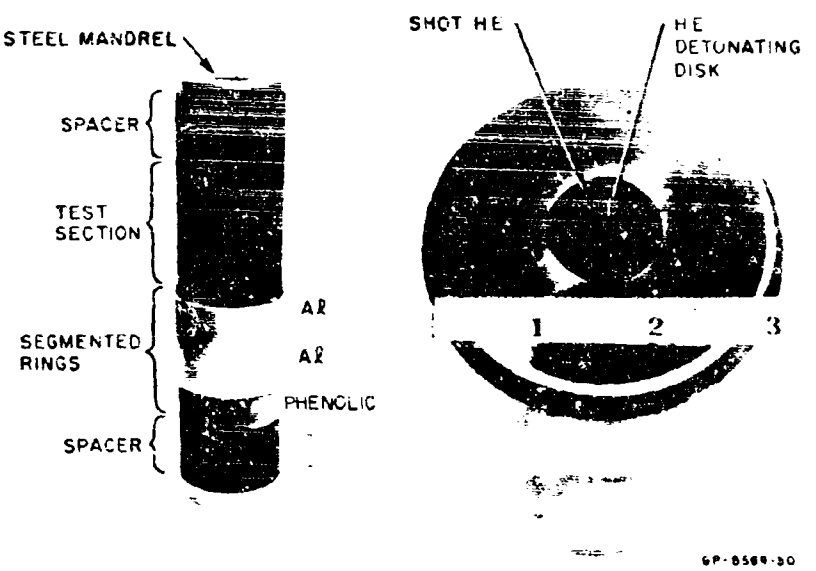

(a) OUTFITTED MANDREL (b) HE PLACEMENT

FIG. 5.1 MAIN ELEMENT OF EXPERIMENT TO VERIFY REBOUND CRACKING THEORY

*Micarta, Westinghouse.

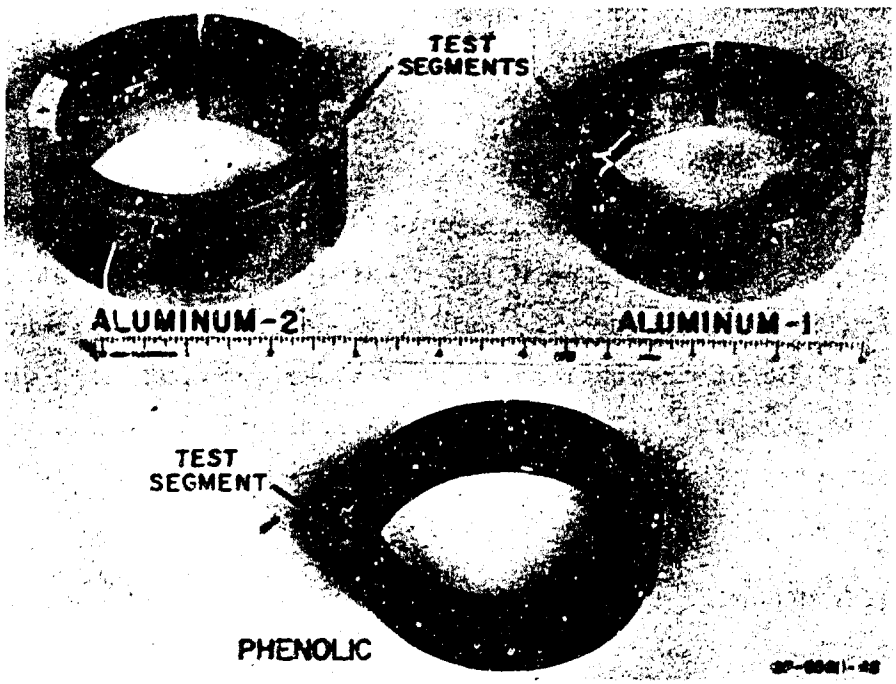

FIG. 5.2 SEGMENTED RINGS

To keep the outer surface unobstructed for photographic observations, the explosive load was applied to the inner surface of the hollow steel mandrel. The main purpose of the experiment was to determine (1) the ability of the theory to predict the velocity of the phenolic segments and (2) the conditions under which the test section would crack.

Selected frames from a framing camera sequence of a typical shot are shown in Fig. 5.3. The segment velocities from such photographs were used to check the predictability of the velocity of the phenolic segments and to determine the input pulse to the test section. To check the predictability of the velocity of the phenolic segments, the wave transit time of the thinner aluminum ring was made equal to that of the phenolic ring; as shown below, this results in the same input pulse to both rings. Using one-dimensional linear wave theory, the phenolic velocity predicted from the velocity of the aluminum segment is found to agree with the observed segment velocity to within 5 percent.

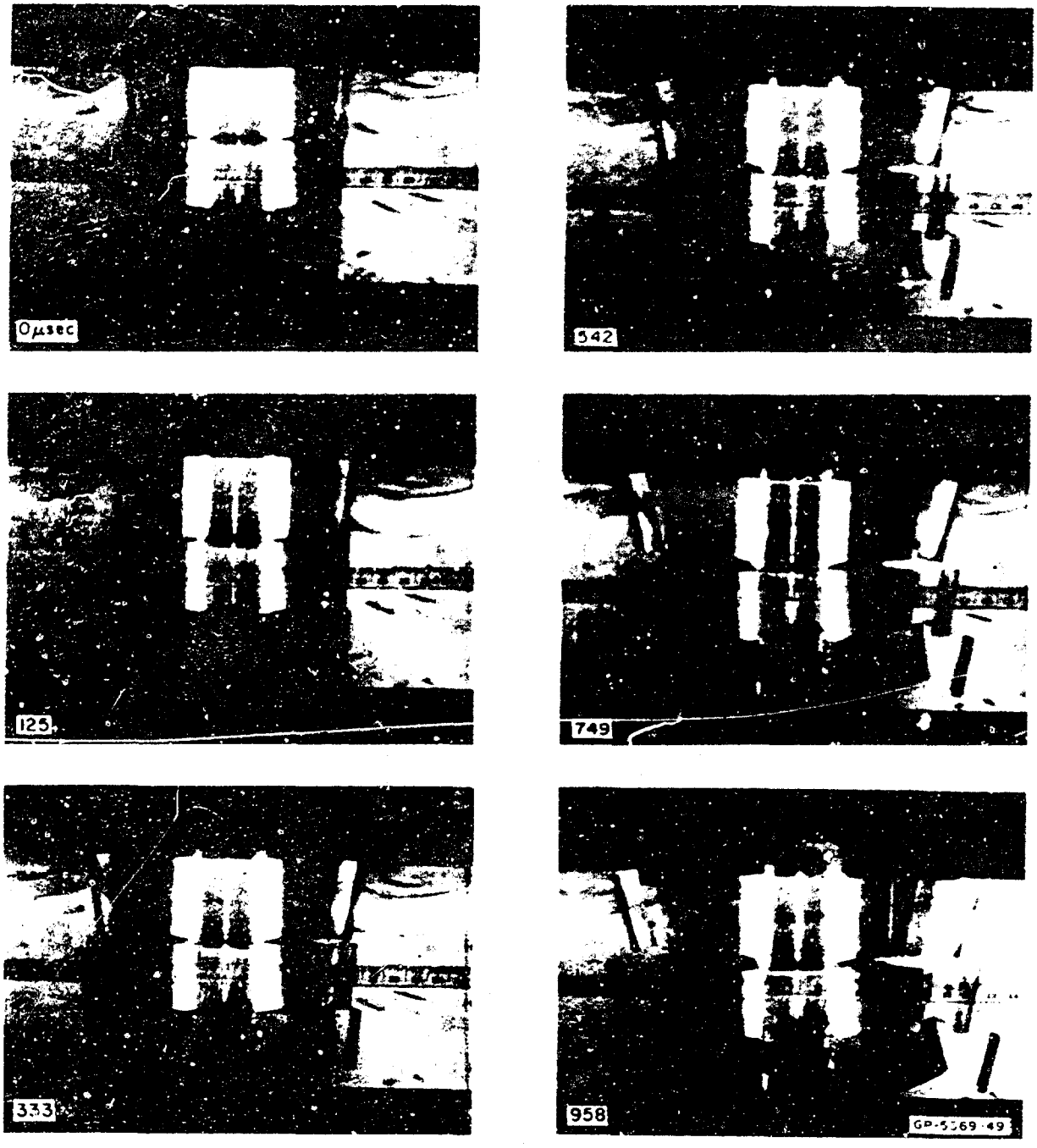

FIG. 5.3 FRAMING PHOTOGRAPHS OF SEGMENTED RINGS. The velocity is determined from the motion of the center of mass.

The initial velocity of the test section is taken to be the same as the velocity of the phenolic segment, which is of equal thickness. It is found that the predicted cracking velocity, based on the static stress-strain curve for the phenolic, and observed cracking velocity agree to within 10 percent. A cracked test section is shown in Fig.5.4.

The velocity of the thicker aluminum ring, together with that of the thinner ring, is used to obtain information of the shape of the input pulse at the segment-mandrel interface. It is found that, of the triangular and exponential shapes, the pulse is matched best by a triangular shape.

Additional information on the experimental setup and the experimental results are given in Section 5.3. In Section 5.2, immediately following, the theoretical basis for the experiments is given.

FIG. 5.4 CRACKED TEST SECTION

5.2 Theory

5.2.1 Shield Velocity for Internal Loading

For comparison with the experiments we calculate the shield velocity for internal loading using one-dimensional linear analysis. Figure 5.5 shows the analysis for a uniform load, taken so for simplicity. Upon arrival at the interface, the incident pulse in the mandrel (state 1) results in a transmitted shock in the shield and a reflected rarefaction in the mandrel, corresponding to state 2. The shock in the shield reflects from the free surface as a rarefaction producing state 02. The arrival of the rarefaction at the interface results in separation. Thus, for internal loading, the maximum duration of the pulse acting on shield is twice the transit time through the shield.

After separation, the pulse continues to accelerate the mandrel. As indicated in Fig. 5.5, if the acceleration continues long enough, the mandrel velocity (e.g., u_{10}) eventually exceeds the separation velocity u_{02} of the shield. To determine the probability of postseparation impact, the motion of the mandrel and shield are analyzed in Appendix A. The results show that, for the thick-walled mandrel used, postseparation impact does not occur.

Since separation occurs when the rarefaction from the free surface arrives at the interface, the momentum I_t transmitted to the shield prior to separation is related to the interface impulse I_i, for a pulse of arbitrary shape, by

$$I_t = K_t I_i \tag{5.1}$$

where

$$K_t = \frac{2z}{1 + z}$$

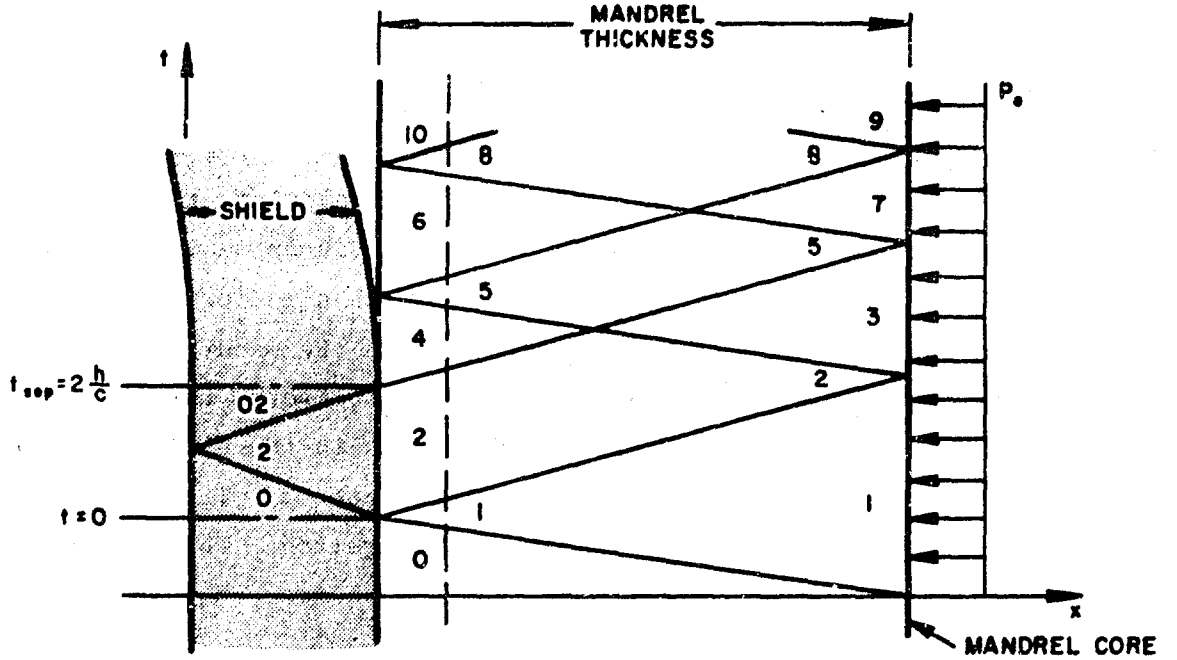

(a) x, t WAVEFRONT DIAGRAM

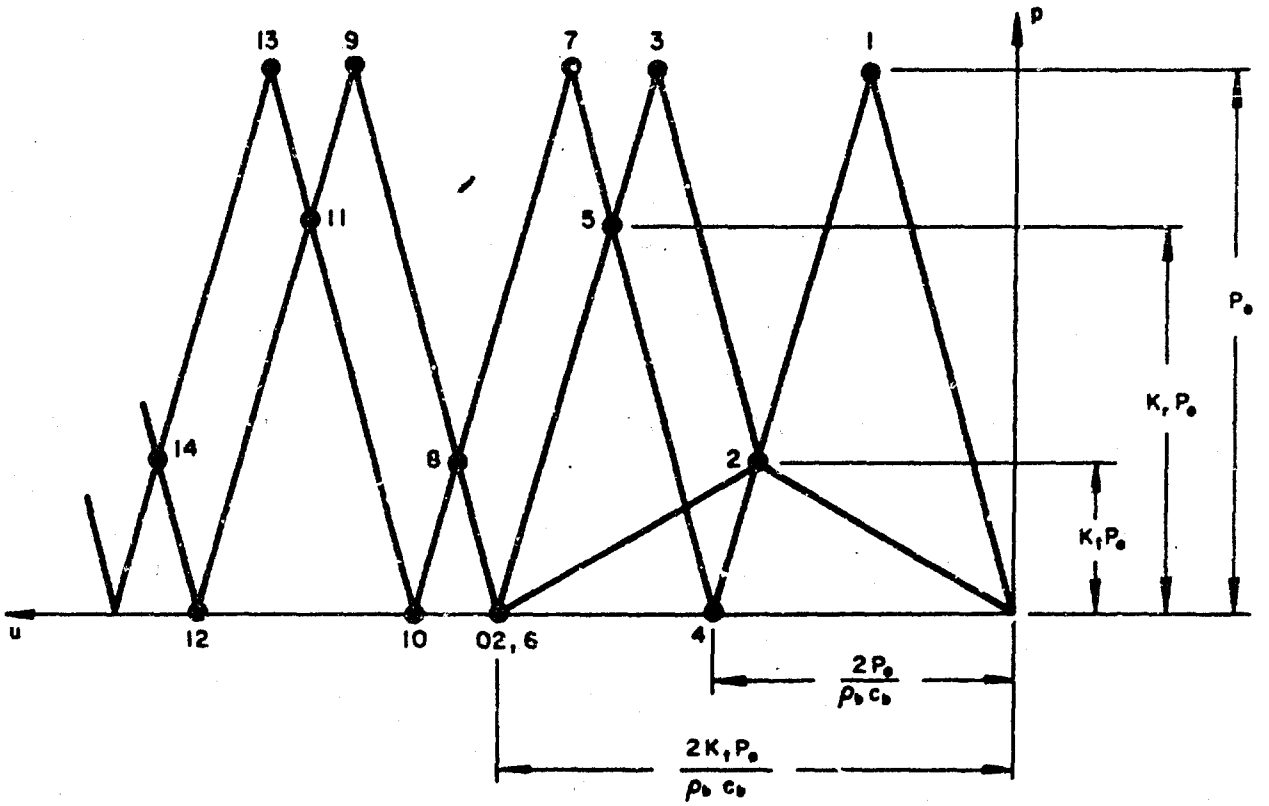

(b) p, u STATE DIAGRAM

FIG. 5.5 x, t AND p, u DIAGRAMS FOR A UNIFORM INTERNAL PULSE

and z is the ratio of the acoustic impedance* of the shield to that of the mandrel.†

For an incident pulse of arbitrary shape, the momentum is given by

$$I_i = PT\gamma \tag{5.2}$$

where P and T are a characteristic pressure and time depending on the pulse shape, and γ is a number depending on the separation time. The momentum of the shield is

$$I_t = \rho h v \tag{5.3}$$

where ρ and h are the density and thickness of the shield and v is

---

*Product of density and sound speed (ρc).

†For an external load to develop an interface pulse of duration comparable to that of the internal load (i.e., not exceeding twice the transit time through the shield), the external load must not exceed a duration of twice the transit time through the shield. For an external pulse of arbitrary shape satisfying this condition, the rebound momentum I' is related to the incident external impulse I_e by

$$I' = K_r' I_e$$

where

$$K_r' = \frac{1 - z^{-1}}{1 + z^{-1}}$$

Equating I' to I_t from (5.1) yields for the equivalent external pulse

$$I_e = \frac{2z}{z - 1} I_i$$

This equation places no restrictions on pulse shape, only on impulse.

the velocity. Putting (5.3) and (5.2) into (5.1) gives

$$v = K_t \frac{P}{\rho c} \frac{T}{h/c} \gamma \tag{5.4}$$

c being sound speed and h/c the transit time through the shield. Furthermore, for equal shield transit times h/c, the separation times and hence the values of γ are equal. In the experiments described below, the transit time of one of the aluminum rings was equal to that of the phenolic ring. For this condition (5.4) yields

$$v_M = \frac{(K_t)_M}{(K_t)_{Al}} \frac{(\rho c)_{Al}}{(\rho c)_M} v_{Al} \tag{5.5}$$

where v_{Al} is the observed velocity of the 1/4-inch aluminum segment and v_M is the predicted velocity of the phenolic segment. Values of v_M from (5.5) are compared with observed phenolic segment velocities in the next section.

5.3 Experiments

5.3.1 Experimental Setup

Figure 5.6 shows the steel mandrel and the external parts. A new setup was used for each shot. The top and bottom 1/8-inch-thick solid phenolic sections served as spacers to reduce end effects. Cracking of the 4-inch phenolic test section was determined by posttest examination. The material properties of the phenolic and aluminum and of the steel mandrel are given in Table 5.1.

The contact surfaces of the mandrel were ground to insure positive contact. The three phenolic rings were installed using oil between the surfaces. The segmented rings were attached with a thin layer of adhesive.* The small test segments (Fig. 5.2), used to determine the rebound velocities of the phenolic and aluminum, were positioned at right angles to the focal plane of the camera.

*Eastman 910.

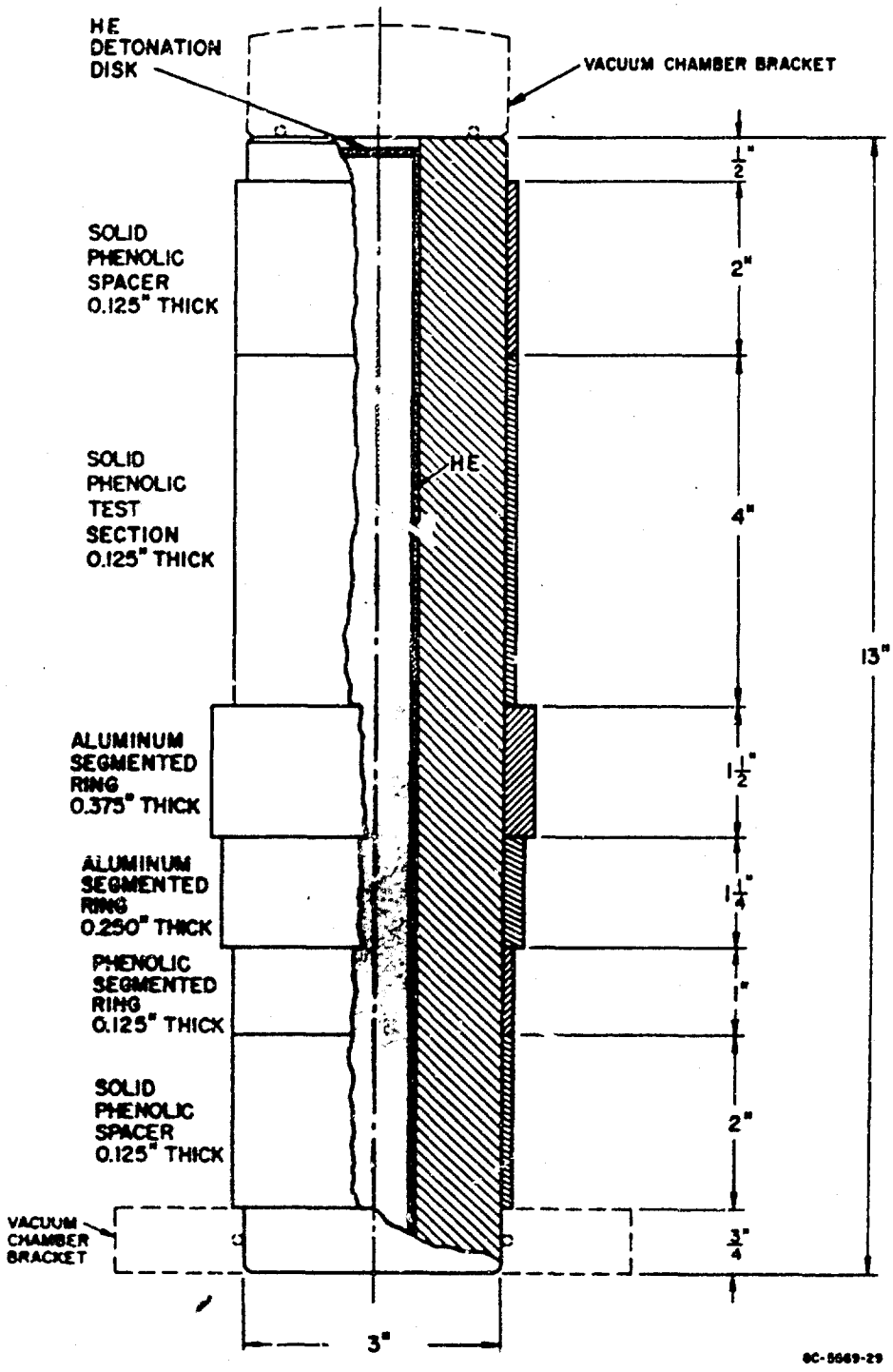

FIG. 5.6 TEST MANDREL

Table 5.1

MATERIAL PROPERTIES

Material	Density (g/cm^3)	Sound Speed (cm/μsec)	Thickness (inch)	Transit Time (μsec)
Phenolic	1.39	0.26	0.125	1.23
Aluminum-1 (6061-T6)	2.77	0.51	0.250	1.24
Aluminum-2 (6061-T6)	2.77	0.51	0.375	1.86
Steel	7.87	0.50	1.0	5.08

A 12-inch length of plastic explosive* was placed in contact with the mandrel core (Fig. 5.6) and a thin explosive detonating disk inserted at the top. The disk, detonated at the center as shown in Fig. 5.7, produced a radial detonation front which simultaneously initiated the main charge around the circumference.

*EL-506D, DuPont.

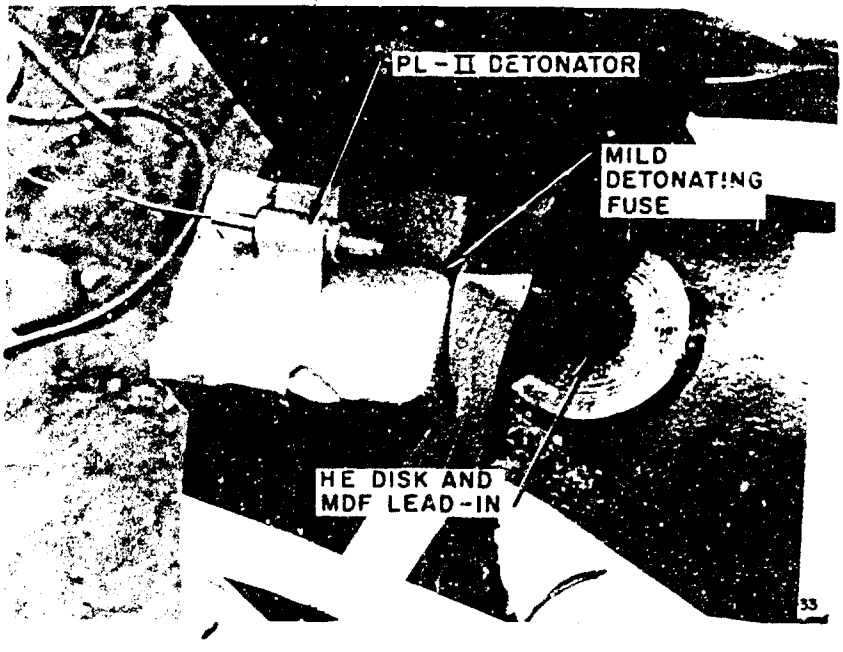

FIG. 5.7 DETONATOR ARRANGEMENT

Preliminary calculations indicated that the aerodynamic pressure acting on the test segments after separation would decelerate the sections by 15 percent during the 1-millisecond coverage of the framing camera. Consequently, a vacuum chamber was designed to produce a 50-micron environment (Fig. 5.8). Figure 5.9 is a view of the experimental setup with three light boxes installed on the front of the chamber.

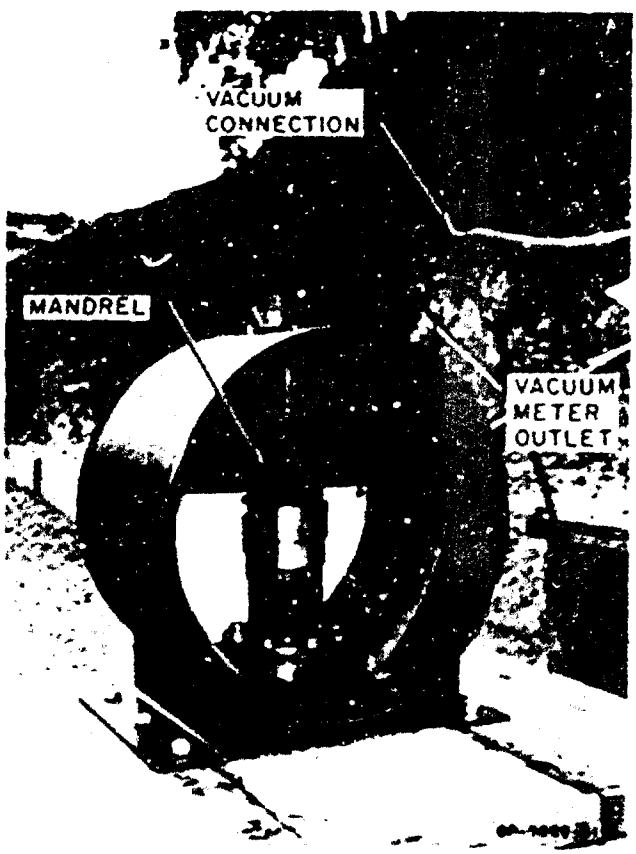

FIG. 5.8 VACUUM CHAMBER

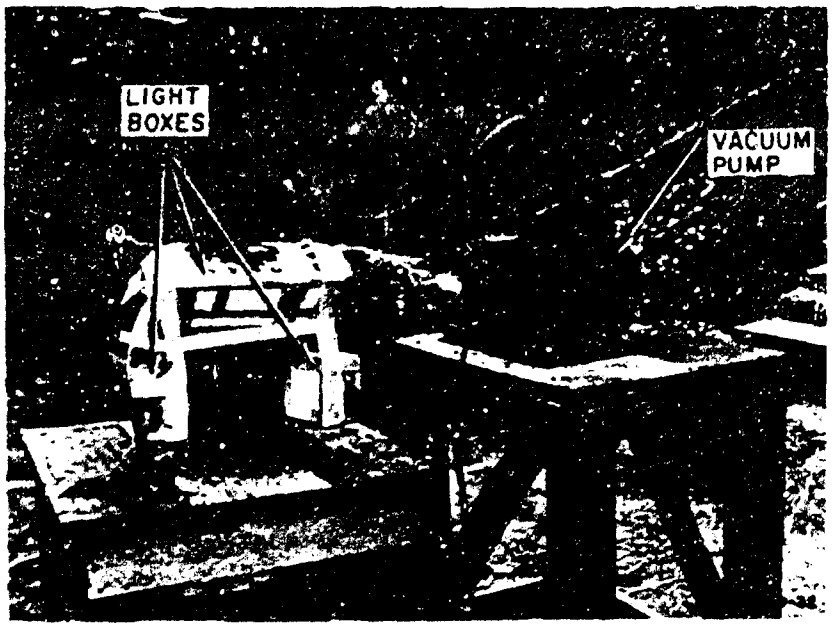

FIG. 5.9 EXPERIMENTAL SETUP

5.3.2 Shield Velocities

The segment velocities are given in Table 5.2. The observed values are those obtained from photographic records. The calculated phenolic velocities were obtained using the velocity of the 1/4-inch aluminum segments and the properties of Table 5.1 in (5.5). The last column gives the ratio of the observed and calculated Micarta velocities. The agreement is within experimental error and is better than expected. The ratio is plotted in Fig. 5.10.

5.3.3 Cracking Velocity of the Phenolic

Of the shots listed in Table 5.2, only the last resulted in cracking of the phenolic test section (see Fig. 5.4). Thus, the cracking velocity of the test section was between 4.44 and 4.57 cm/msec.

Table 5.2

SHIELD VELOCITIES

Shot No.*	Velocities (cm/msec)				$\frac{V_{obs}}{V_{calc}}$ †
	Observed			Calculated	
	3/8" Al.	1/4" Al.	Phenolic	Phenolic	
1 (12276)	1.40	1.76	2.30	2.18	1.05
2 (12226)	1.86	2.27	2.72	2.82	0.97
3 (11970)	2.37	2.81	3.54	3.48	1.02
4 (12227)	3.02	3.26	3.93	4.04	0.97
5 (12277)	3.17	3.46	4.44	4.29	1.03
6 (12278)	3.48	3.71	4.57	4.60	0.99

*SRI shot number noted in parentheses.

†Ratio of observed and calculated phenolic velocities.

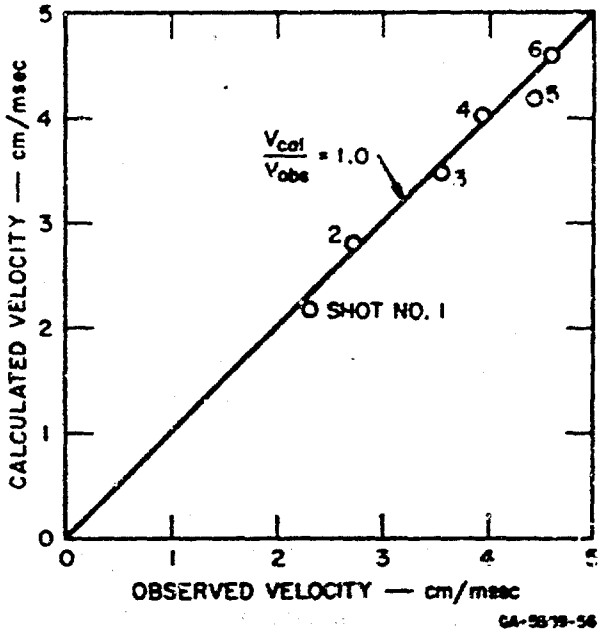

FIG. 5.10 PHENOLIC VELOCITY
(calculated vs. observed)

From (2.29), the relationship between the cracking velocity v_{cr} and circumferential cracking stress $\sigma_{\theta cr}$ for a ring of a linear material in uniform radial motion is given by

$$v_{cr} = \frac{\sigma_{\theta cr}}{\rho c}\sqrt{1-\nu^2} \tag{5.6}$$

where we have substituted $c_\theta/c = \sqrt{1-\nu^2}$ and ν is Poisson's ratio. Using the properties of Table 5.1 for phenolic in (5.6) yields

$$v_{cr} = 4.29 \text{ cm/msec}$$

This is less than 10 percent below the velocity of 4.57 cm/msec which produced cracking. The difference is well within uncertainties in material properties and experimental error.

5.3.4 Pulse Shape

To investigate the pulse shape at the interface, the momentum of the two aluminum segments was equated to the impulse developed at the interface to obtain

$$\text{mom} = \rho h v = \int_0^{t_s} p(t)dt \tag{5.7}$$

where $p(t)$ is the interface pressure time profile being investigated and t_s is the separation time.

For a uniform pulse, (5.7) yields

$$\rho h v = P_o t_s \tag{5.8}$$

where P_o is peak pressure. For a pulse with a linear decay, (5.7) gives

$$\rho h v = P_o t_s \left[1 - \frac{t_s}{2T}\right] \text{ (triangular)} \tag{5.9}$$

where P_o is peak pressure and T is the pulse duration. For a pulse with an exponential decay

$$p(t) = P_o e^{-\lambda t} \tag{5.10}$$

where λ is the decay constant, (5.7) yields

$$\rho hv = \frac{P_o}{\lambda}\left[1 - e^{-\lambda t_s}\right] \text{ (exponential)} \tag{5.11}$$

The two aluminum segments of different thicknesses, aluminum-1 and aluminum-2, provide two sets of momentum and t_s values. For the rectangular pulse (5.8) each set of values defines a peak pressure, P_{o1} and P_{o2}. The pressures obtained using the velocities from Table 5.2 are listed in Table 5.3 and are shown in Fig. 5.11 for Shot 3. The ratio of the values range from 0.80 to 0.94 indicating that the pulse decays roughly 10 to 20 percent in 1.24 μsec.* This time is half the separation time for the phenolic and thin aluminum segments; hence the pulse probably decays roughly 20 to 40 percent from 0 to 2.5 μsec. This indicates that a decaying pulse is a better representation of the pulse actually realized at the interface.

As indicated in (5.9) and (5.11), two parameters, peak pressure and decay time, are required to specify a decaying pulse. Using the two sets of values of momentum and separation time from the aluminum-1 and aluminum-2 segments, the peak pressure and decay time may be found. For the triangular pulse

$$T = \frac{1}{2}\,\frac{\dfrac{h_1}{h_2}\dfrac{v_1}{v_2}\dfrac{t_2^2}{t_1} - t_1}{\dfrac{h_1}{h_2}\dfrac{v_1}{v_2}\dfrac{t_2}{t_1} - 1} = f\left(\frac{v_1}{v_2}\right) \tag{5.12}$$

*Difference in transit times of the aluminum segments (see Table 5.1).

Table 5.3

PULSE SHAPE RESULTS

Shot	HE Thickness (mils)	Incident Impulse* (taps)	Calculated Interface Conditions								
			Rectangular			Exponential			Triangular		
			P_{o1} (kbar)	P_{o2} (kbar)	$\frac{P_{o2}}{P_{o1}}$	P_o (kbar)	τ (μsec)	I (taps)	P_o (kbar)	T (μsec)	I (taps)
1	31	20,600	2.38	1.89	0.80	3.23	3.89	12,560	3.01	6.02	9,050
2	42	28,000	3.07	2.52	0.82	4.16	3.89	16,200	3.88	6.02	11,670
3	52	34,700	3.80	3.21	0.84	5.15	3.89	20,050	4.80	6.02	14,440
4	61	40,700	4.41	4.09	0.93	5.98	3.89	23,260	5.57	6.02	16,750
5	67	44,600	4.68	4.29	0.92	6.35	3.89	24,600	5.90	6.02	17,800
6	72	48,000	5.02	4.71	0.94	6.80	3.89	26,470	6.34	6.02	19,070

*10,000 taps/15 mils.

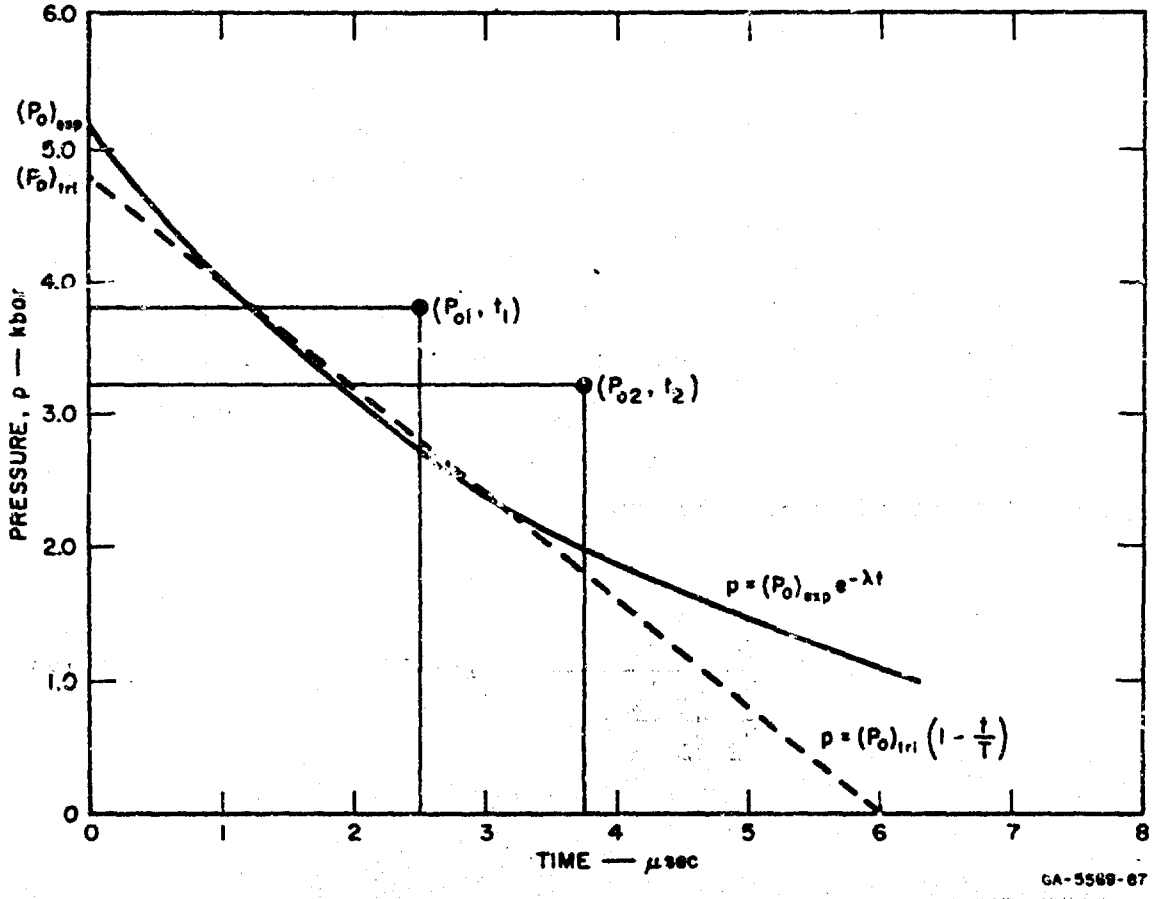

FIG. 5.11 PULSE SHAPE DIAGRAM FOR SHOT 3

and, using T in (5.9), the peak pressure may be determined. For the exponential pulse

$$\frac{v_1}{v_2} = \frac{h_2(1 - e^{-\lambda t_1})}{h_1(1 - e^{-\lambda t_2})} \tag{5.13}$$

where λ also becomes a function of v_1/v_2 and must be determined by trial and error. The peak pressure is found from (5.11).

The velocities of Table 5.2 are plotted in Fig. 5.12 as a function of incident impulse. The pair of lines indicate a constant velocity ratio, v_2/v_1, of 0.87 which is the rms value of the experimental values. The variation of the experimentally determined values from the mean ratio is attributed to experimental error. Since, for the chosen pulse shapes, the decay constants depend only on the velocity ratio, which is approximately constant, the pulse duration at the segment-mandrel interface must be independent of the incident impulse.

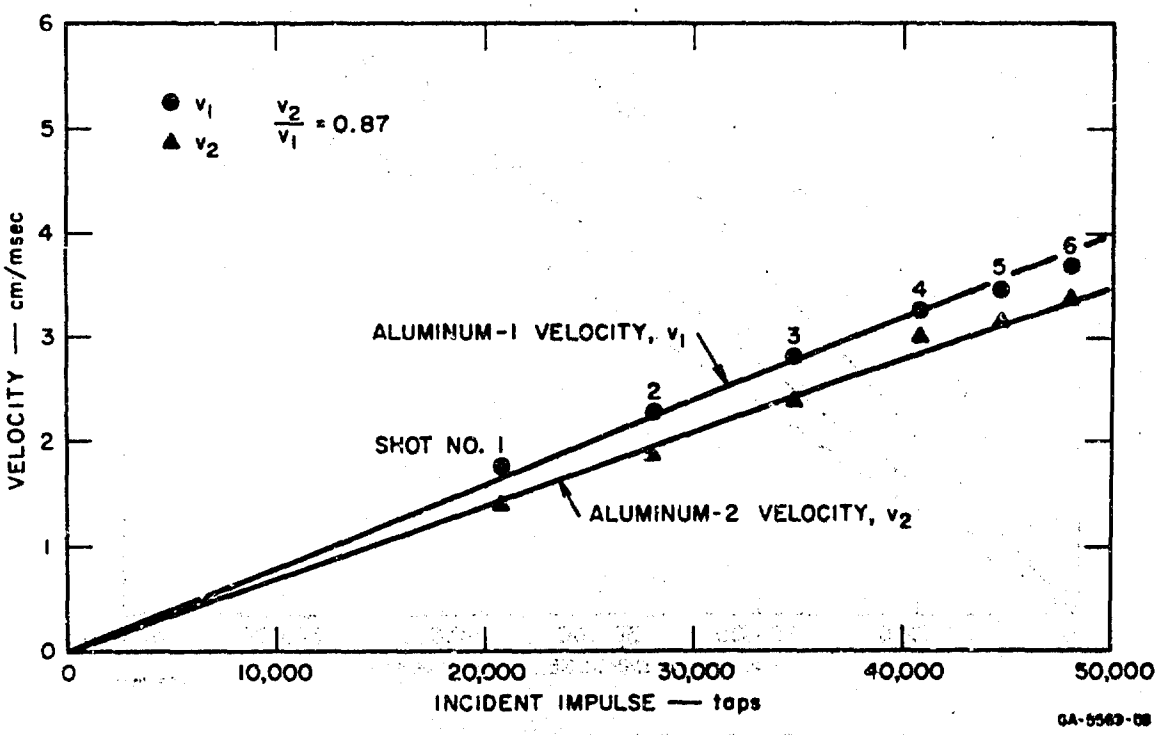

FIG. 5.12 ALUMINUM SEGMENT VELOCITIES

Hence, only peak pressure varies with the explosive thickness. The values obtained for these conditions are given in Table 5.3. The corresponding pulses for Shot 3 are plotted in Fig. 5.11.

Figure 5.13 gives the calculated total impulse for the exponential and linear decay curves based upon the decay times and peak pressures of Table 5.3. The values increase with incident impulse as shown. Although the impulse realized at the interface should be at least a factor of 1/R lower than the incident impulse due to geometric divergence, the impulse levels for both the pulse profiles analyzed are

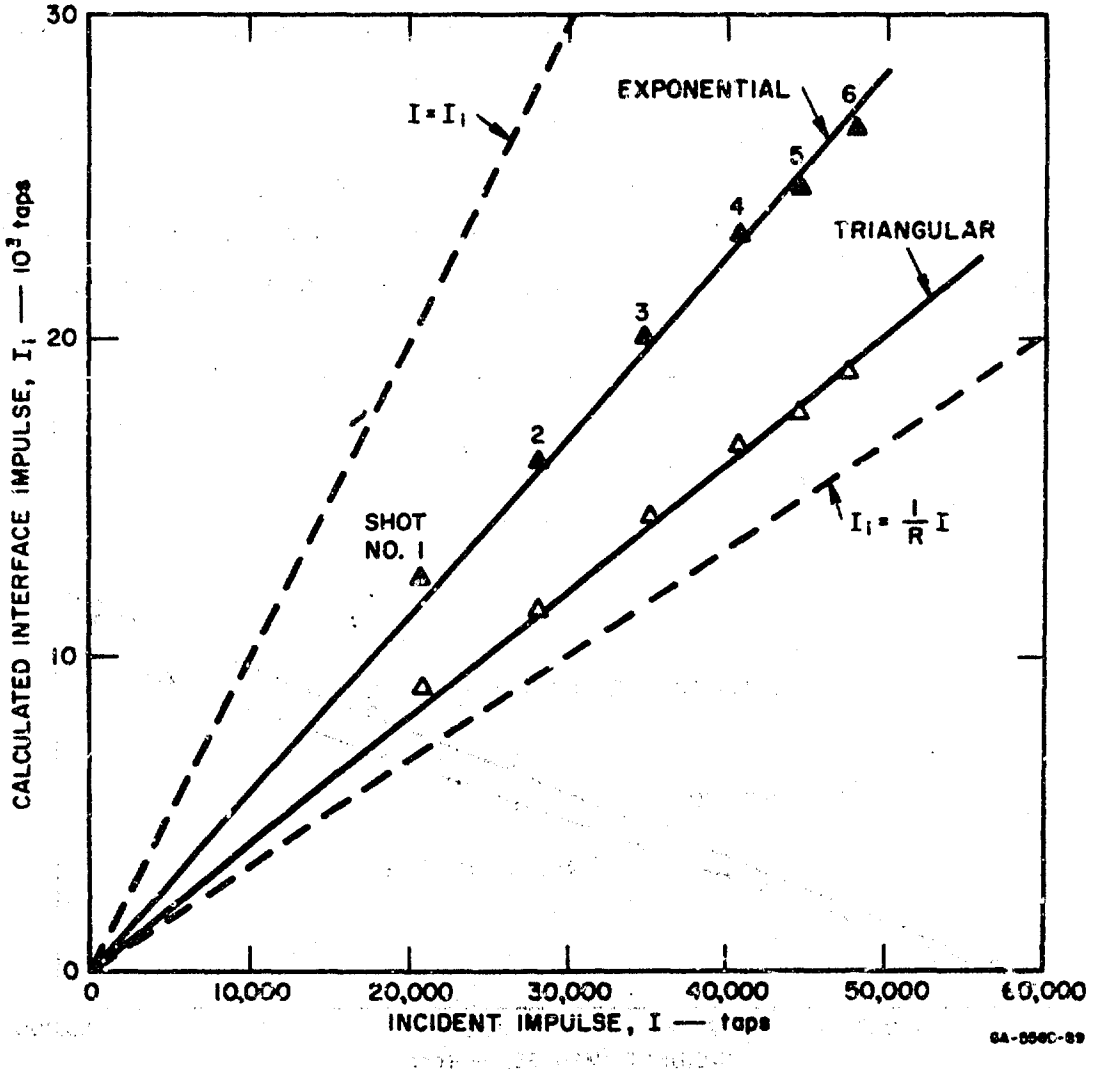

FIG. 5.13 CALCULATED INTERFACE IMPULSE

greater. The triangular representation lies 16 percent above whereas the exponential representation lies 40 percent above. This suggests that

(1) of the two pulse profiles considered, the linear decay best represents the actual pulse, and

(2) the actual pulse probably decays more rapidly than the linear decay model.

This page intentionally left blank.

APPENDIX A

ANALYSIS OF POSTSEPARATION MOTION OF MANDREL AND SHIELD

A.1 Introduction

The calculated velocities of the phenolic segments given in Section 5 are valid only if there is no postseparation impact during the initial outward motion. The analysis given here shows that, for the chosen conditions of the experiments, postseparation impact does not occur during the initial outward motion.

In the analysis, the phenolic ring is treated as a linear oscillator, taking the velocity at separation as the initial velocity. The motion of the outer surface of the mandrel is calculated by regarding a thin outer layer of the mandrel as a linear oscillator being loaded by pulses determined by the stress wave pattern.

A.2 Stress Wave Calculations

Figure A.1 shows the x,t and u,p diagrams for a one-dimensional laminate corresponding to the mandrel and the shield. Since wave velocities are not very sensitive to pressure, the wave pattern in cylindrical geometry would be essentially the same. We regard the load for the one-dimensional calculation as an equivalent load which produces the same pulse at the interface as would occur in cylindrical geometry. The motion of the shield and the outer surface of the mandrel are both taken to be proportional to the load amplitude at the interface. Thus, in calculating the motion of the mandrel, we depend on the stress wave calculation only for the frequency at which the pulses arrive at the interface.

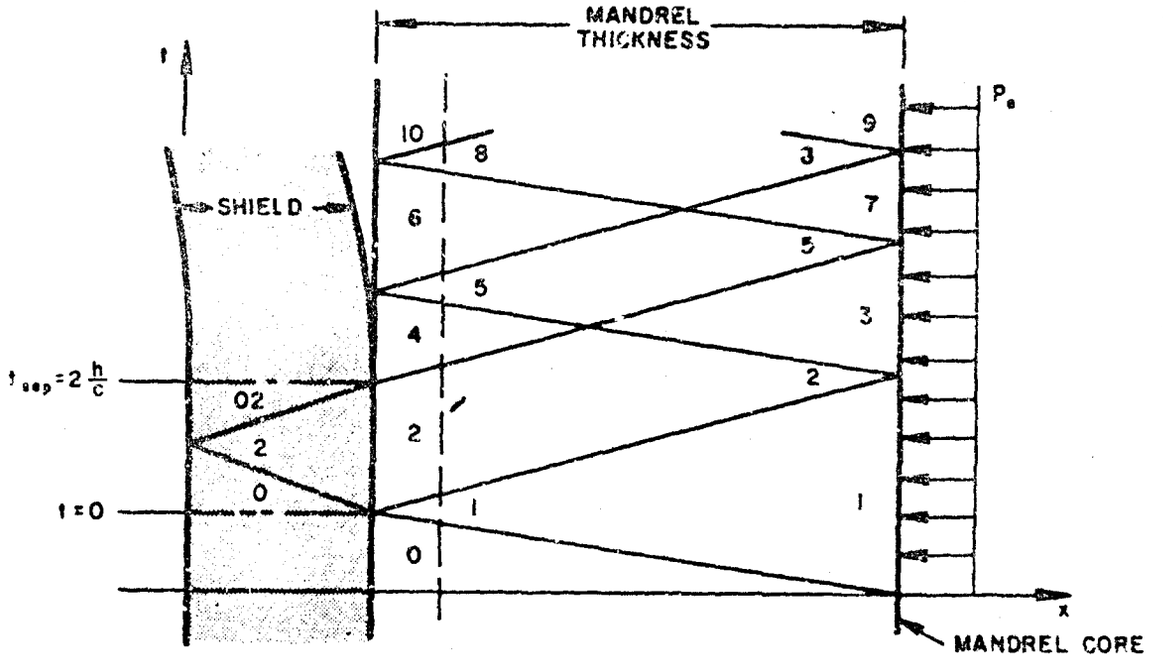

(a) x, t WAVEFRONT DIAGRAM

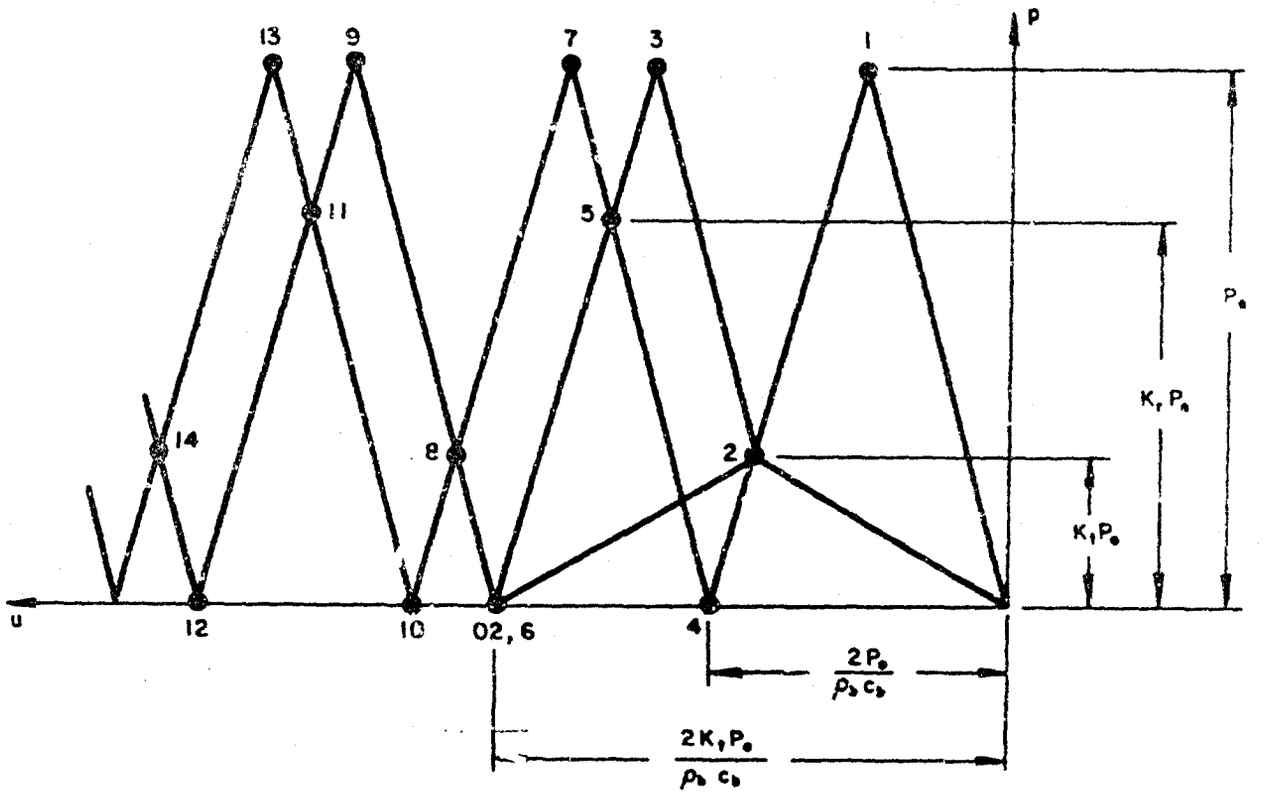

(b) p, u STATE DIAGRAM

GA-8868-28

FIG. A.1 x,t AND p,u DIAGRAMS FOR A UNIFORM INTERNAL PULSE

In Fig. A.1 the shield separates from the mandrel at the velocity u_{02}. This is taken as the initial velocity of the phenolic ring. The initial velocity of the outer surface of the mandrel is u_4. The outer layer of the mandrel, indicated by the dashed line in Fig. A.1a, will be accelerated further by pulses of amplitude p_5, p_8, etc. Moreover, the duration of the pulse is proportional to the thickness of the outer layer, hence the acceleration is independent of the thickness chosen. In the calculations below, an outer layer of convenient thickness is used to calculate the motion of the outer surface of the mandrel under the action of the successive pulses and the restraining hoop stresses.

A.3 Motion of Phenolic Ring and Mandrel Surface

The motion of the phenolic ring is simply

$$x = \frac{u_{02}}{q} \sin qt \qquad (A.1)$$

where u_{02} is the velocity of the phenolic at separation and q is given by

$$q = \frac{E}{\rho r^2} \qquad (A.2)$$

E and ρ being Young's modulus and density for the phenolic shield and r the mean radius of the shield.

The motion of the outer surface of the mandrel is given by

$$x = \frac{u_4}{q_b} \sin q_b t + \frac{F(t)}{q_b^2} (1 - \cos q_b t) \qquad (A.3)$$

where u_4 is the velocity of the mandrel surface at separation, $F(t)$ is the forcing function, and

$$q_b = \frac{E_b}{\rho_b r_b} \qquad (A.4)$$

E_b and ρ_b being Young's modulus and density for the steel mandrel and r_b the mean radius of the outer layer.

From Fig. A.1

$$u_{02} = \frac{2P_o K_t}{\rho_b c_b} \tag{A.5}$$

where

$$K_t = \frac{2}{1 + \frac{\rho c}{\rho_b c_b}} \tag{A.6}$$

ρc and $\rho_b c_b$ being the acoustic impedances of the phenolic shield and steel mandrel, here taken as $\rho c = 0.358$, $\rho_b c_b = 4.00$ barsec/cm. The velocity of the mandrel surface at separation is

$$u_4 = \frac{2P_o}{\rho_b c_b} \tag{A.7}$$

The amplitudes of the pulses p_5, p_8, etc. are indicated in Fig. A.1. For p_5 we have

$$p_5 = K_r P_o \tag{A.8}$$

where

$$K_r = \frac{1 - \frac{\rho c}{\rho_b c_b}}{1 + \frac{\rho c}{\rho_b c_b}} \tag{A.9}$$

For p_8

$$p_8 = K_t P_o \tag{A.10}$$

The duration of the pulses at the outer layer is twice the transit time through the layer.

A.4 Results

The motion of the phenolic ring and the outer surface of the mandrel are shown in Fig. A.2 for a mandrel 25.4 mm thick. The paths indicate that impact does not occur during the initial outward motion.

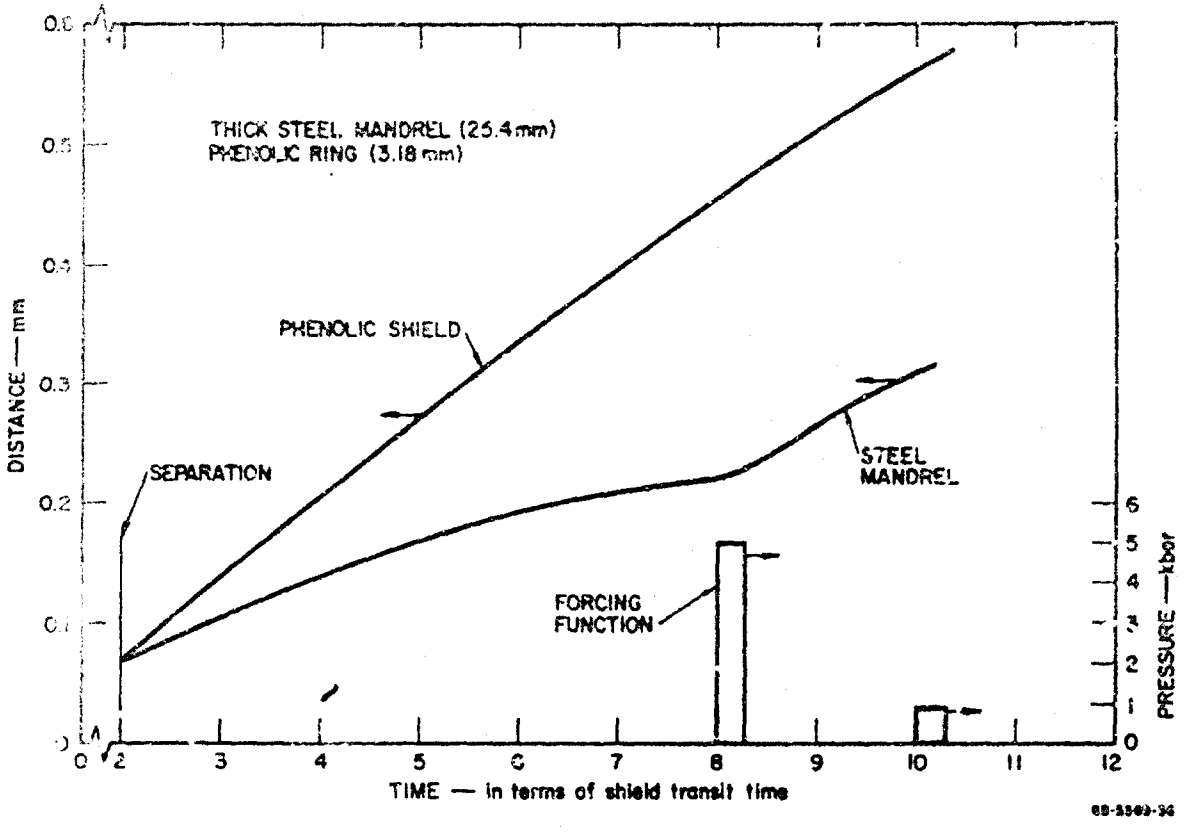

FIG. A.2 DISPLACEMENT-TIME DIAGRAM OF PHENOLIC SHIELD AND THICK STEEL MANDREL

Figure A.3 shows the same phenolic motion and that of a mandrel 8 mm thick. In this case the mandrel overtakes the shield.

In the experiments a mandrel thickness of 25.4 mm was used. Hence, postseparation impact during the initial outward motion was avoided.

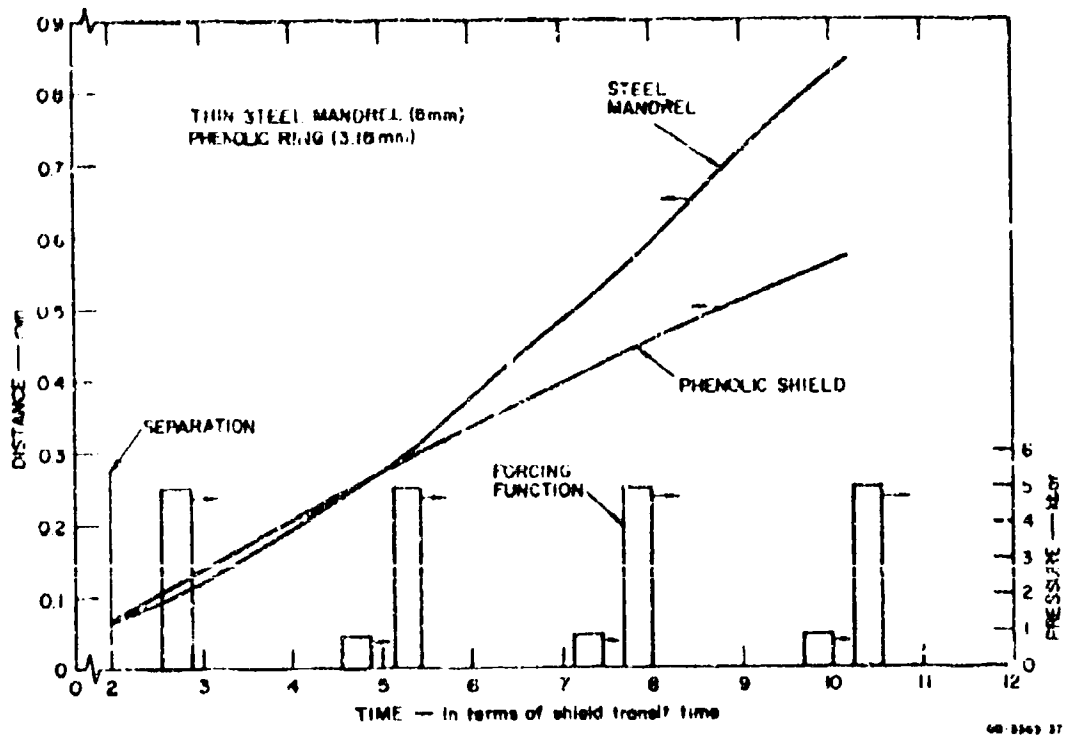

FIG. A.3 DISPLACEMENT-TIME DIAGRAM OF PHENOLIC SHIELD AND THIN STEEL MANDREL

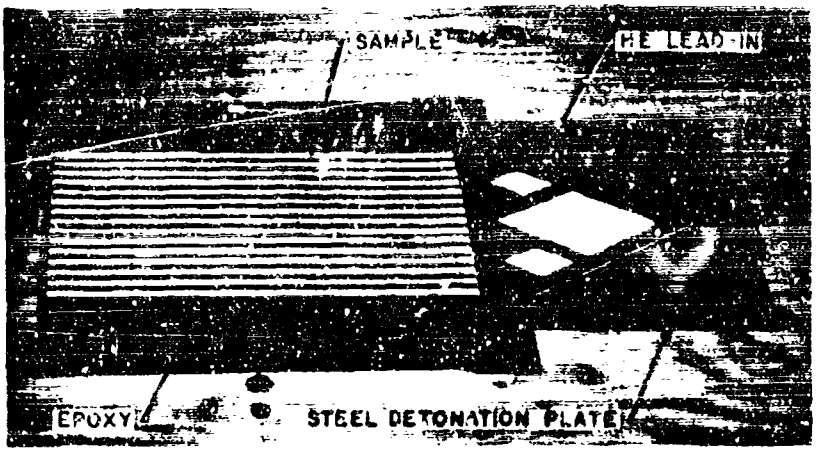

FIG. B.3 EXPERIMENTAL SETUP

Table B.1

SLAB EXPERIMENT RESULTS

Shot	Impulse (taps)	Loading	Damage
1	10,000	15 mil solid HE sheet	Severe spall
2	5,000	15 mil 1/8-inch strips spaced 1/8 inch	Moderate spall
3	3,400	15 mil 1/8-inch strips spaced 1/4 inch	Marginal end crack

In the final test, a 3400-tap load produced a minor crack at the opposite end from that at which the explosive was initiated (Fig. B.6). This damage is attributed to edge effects. The 3400-tap loading is considered a lower bound on the impulse to cause separation.

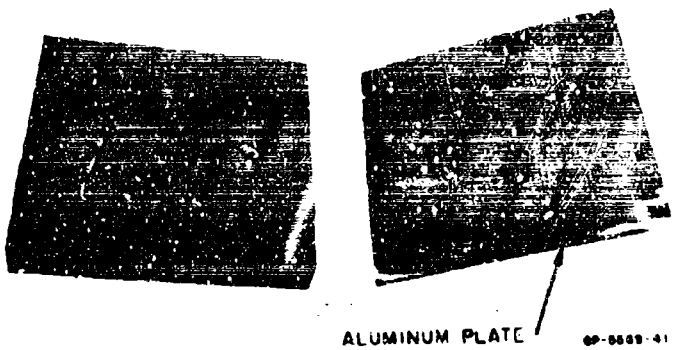

FIG. B.4 COMPOSITE (10,000 Tops)

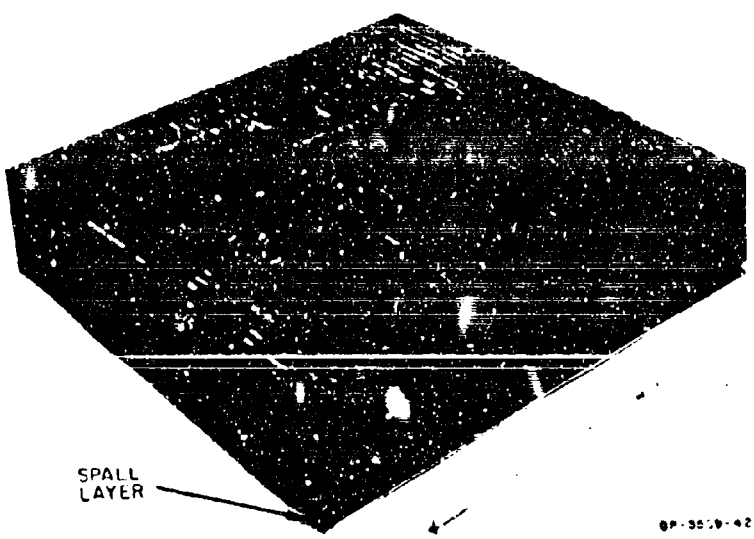

FIC. B.5 COMPOSITE (5000 Tops)

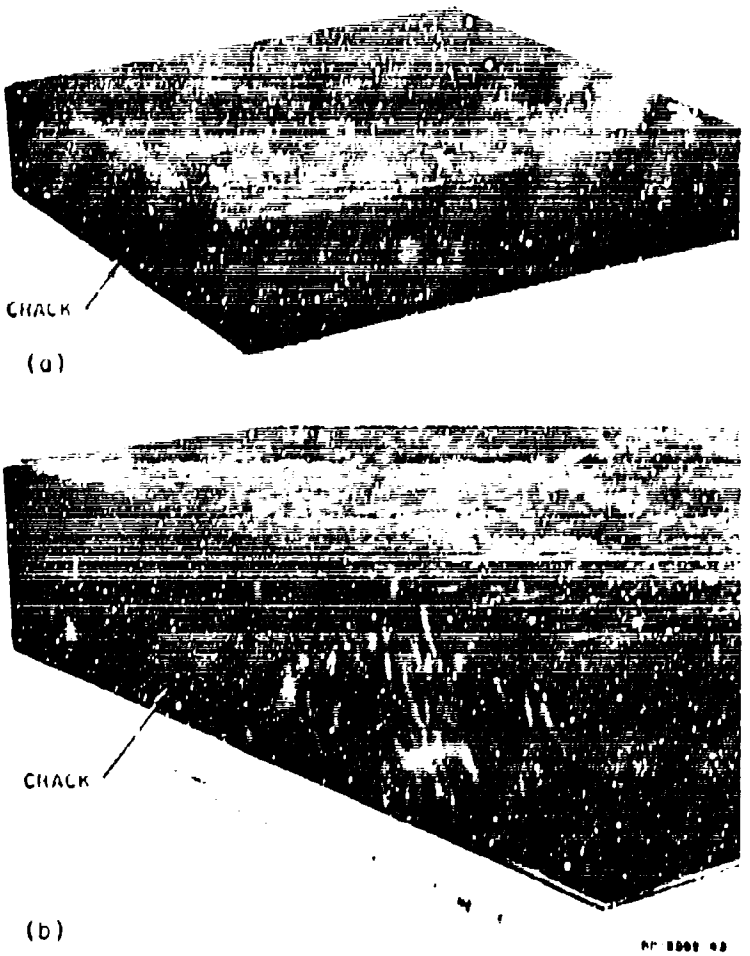

FIG. B.6 COMPOSITE (3400 Tape

This page intentionally left blank.

Unclassified

Security Classification

DOCUMENT CONTROL DATA - R&D

(Security classification of title, body of abstract and indexing annotation must be entered when the overall report is classified)

1. ORIGINATING ACTIVITY (Corporate author)
Stanford Research Institute
Menlo Park, California

2a. REPORT SECURITY CLASSIFICATION
Unclassified

2b. GROUP

3. REPORT TITLE
CRITICAL LOAD CURVES FOR REBOUND CRACKING

4. DESCRIPTIVE NOTES (Type of report and inclusive dates)
Final Report June 1965 through September 1966

5. AUTHOR(S) (Last name, first name, initial)
Samuelsen, G. S.; Stuiver, W.; Abrahamson, G. R.

6. REPORT DATE	7a. TOTAL NO. OF PAGES	7b. NO. OF REFS
March 1967	112	6

8a. CONTRACT OR GRANT NO.	9a. ORIGINATOR'S REPORT NUMBER(S)
AF29(601)-6828 b. PROJECT NO. 5710 c. Subtask No. 15.014 d.	AFWL-TR-66-130 9b. OTHER REPORT NO(S) (Any other numbers that may be assigned this report) SRI Project FGU-5569

10. AVAILABILITY/LIMITATION NOTICES This document is subject to special export controls and each transmittal to foreign governments or foreign nationals may be made only with prior approval of AFWL (WLRP), Kirtland AFB, N.M. 87117. Distribution of this document is limited because of the technology discussed.

11. SUPPLEMENTARY NOTES	12. SPONSORING MILITARY ACTIVITY
	Air Force Weapons Laboratory (WLRP) Kirtland Air Force Base, New Mexico 87117

13. ABSTRACT

It is shown that, under an external load, a cylindrical plastic shell mounted on a steel mandrel can rebound at a velocity sufficient to cause cracking of the shield due to hoop tension. Using numerical calculations, critical load curves are found for the combinations of peak pressure and impulse which divide the loads that produce cracking from those that do not. These curves are found to be consistent with semigraphical solutions based on the method of characteristics. The latter method is also used to obtain critical load curves for spall.

Experiments that verify the theory of rebound cracking are reported.

DD FORM 1 JAN 64 1473

Unclassified

Security Classification

Unclassified
Security Classification

14. KEY WORDS	LINK A		LINK B		LINK C	
	ROLE	WT	ROLE	WT	ROLE	WT
Pressure Impulse Cracking Spall						

INSTRUCTIONS

1. ORIGINATING ACTIVITY: Enter the name and address of the contractor, subcontractor, grantee, Department of Defense activity or other organization *(corporate author)* issuing the report.

2a. REPORT SECURITY CLASSIFICATION: Enter the overall security classification of the report. Indicate whether "Restricted Data" is included. Marking is to be in accordance with appropriate security regulations.

2b. GROUP: Automatic downgrading is specified in DoD Directive 5200.10 and Armed Forces Industrial Manual. Enter the group number. Also, when applicable, show that optional markings have been used for Group 3 and Group 4 as authorized.

3. REPORT TITLE: Enter the complete report title in all capital letters. Titles in all cases should be unclassified. If a meaningful title cannot be selected without classification, show title classification in all capitals in parenthesis immediately following the title.

4. DESCRIPTIVE NOTES: If appropriate, enter the type of report, e.g., interim, progress, summary, annual, or final. Give the inclusive dates when a specific reporting period is covered.

5. AUTHOR(S): Enter the name(s) of author(s) as shown on or in the report. Enter last name, first name, middle initial. If military, show rank and branch of service. The name of the principal author is an absolute minimum requirement.

6. REPORT DATE: Enter the date of the report as day, month, year, or month, year. If more than one date appears on the report, use date of publication.

7a. TOTAL NUMBER OF PAGES: The total page count should follow normal pagination procedures, i.e., enter the number of pages containing information.

7b. NUMBER OF REFERENCES: Enter the total number of references cited in the report.

8a. CONTRACT OR GRANT NUMBER: If appropriate, enter the applicable number of the contract or grant under which the report was written.

8b, 8c, & 8d. PROJECT NUMBER: Enter the appropriate military department identification, such as project number, subproject number, system numbers, task number, etc.

9a. ORIGINATOR'S REPORT NUMBER(S): Enter the official report number by which the document will be identified and controlled by the originating activity. This number must be unique to this report.

9b. OTHER REPORT NUMBER(S): If the report has been assigned any other report numbers *(either by the originator or by the sponsor)*, also enter this number(s).

10. AVAILABILITY/LIMITATION NOTICES: Enter any limitations on further dissemination of the report, other than those imposed by security classification, using standard statements such as:

(1) "Qualified requesters may obtain copies of this report from DDC."

(2) "Foreign announcement and dissemination of this report by DDC is not authorized."

(3) "U. S. Government agencies may obtain copies of this report directly from DDC. Other qualified DDC users shall request through

_____."

(4) "U. S. military agencies may obtain copies of this report directly from DDC. Other qualified users shall request through

_____."

(5) "All distribution of this report is controlled. Qualified DDC users shall request through

_____."

If the report has been furnished to the Office of Technical Services, Department of Commerce, for sale to the public, indicate this fact and enter the price, if known.

11. SUPPLEMENTARY NOTES: Use for additional explanatory notes.

12. SPONSORING MILITARY ACTIVITY: Enter the name of the departmental project office or laboratory sponsoring *(paying for)* the research and development. Include address.

13. ABSTRACT: Enter an abstract giving a brief and factual summary of the document indicative of the report, even though it may also appear elsewhere in the body of the technical report. If additional space is required, a continuation sheet shall be attached.

It is highly desirable that the abstract of classified reports be unclassified. Each paragraph of the abstract shall end with an indication of the military security classification of the information in the paragraph, represented as *(TS), (S), (C), or (U)*.

There is no limitation on the length of the abstract. However the suggested length is from 150 to 225 words.

14. KEY WORDS: Key words are technically meaningful terms or short phrases that characterize a report and may be used as index entries for cataloging the report. Key words must be selected so that no security classification is required. Identifiers, such as equipment model designation, trade name, military project code name, geographic location, may be used as key words but will be followed by an indication of technical context. The assignment of links, rules, and weights is optional.

AFSC (KAFB NM)

Unclassified
Security Classification

REFERENCES

1. Bungay, R. W., "Estimated Bounds on Suddenly Applied Loads Required to Damage the Heat Shield on a Hardened Reentry Vehicle (U)," Stanford Research Institute Semiannual Tech. Summary Report No. 1, Contract No. AF 29(601)-6251, July 30, 1964 (SRD).

2. von Neumann, J. and R. D. Richtmyer, "A Method for the Numerical Calculation of Hydrodynamic Shocks," J. Appl. Phys. 21, 232-237 (1950).

3. White, M. P. and L. Griffis, "The Propagation of Plasticity in Uniaxial Compression," J. Appl. Mech. Paper No. 48, APM-17.

4. Wood, D. S., "On Longitudinal Plane Waves of Elastic-Plastic Strain in Solids," J. Appl. Mech. 19, 521 (1952).

5. Morland, L. W., "The Propagation of Plane Irrotational Waves through an Elastoplastic Medium," Phil. Trans. Roy. Soc. London, 251, 341-383 (1959).

6. Erkman, J. O., "Artificial Viscosity Code for One-Dimensional Shock Waves," in G. E. Duvall and R. C. Alverson, "Fundamental Research in Support of Vela-Uniform," Stanford Research Institute Report STSR 4, July 15, 1963.